

Czech Technical University in Prague

Faculty of Electrical Engineering  
Department of Electromagnetic Field

***NEW METHODOLOGIES OF REMOTE  
SENSING BASED ON MICROWAVE  
RADIOMETER***

Doctoral Thesis

***Petr Dvořák***

Prague, February 2014

Ph.D. Programme: Electrical Engineering and Information Technology  
Branch of study: Radioelectronics

Supervisor: ***Prof. Ing. Miloš Mazánek, CSc.***  
Supervisor-Specialist: ***Doc. Ing. Stanislav Zvánovec, Ph.D.***

## **Abstract**

In this thesis new methodologies of remote sensing will be described. The thesis consists of two main parts, the first part deals with the new methodology of atmosphere dynamic effects (rain, clouds) sensing by a microwave radiometer. The methodology is based especially on evaluation of brightness temperature variance. Next, methodology of fire remote detection and its properties from the microwave point of view are proposed. Fire emissivity, other fire properties and environmental parameters are examined and described.

**Keywords:** radiometry, atmosphere sensing, rain prediction, fire sensing.

## **Acknowledgements**

I would like to thank everyone who has helped and contributed no matter how indirectly. Nevertheless, a special mention deserves Doc. Ing. Stanislav Zvánovec Ph.D. without whose support and endless patience I would not be able to finish the thesis. Equally, I would like to express my thankfulness to Prof. Ing. Miloš Mazánek CSc. for all the support despite his incredible workload of leadership of our Department of Electromagnetic Field. Unfortunately, I cannot list all the other people who deserve my gratitude for helping me any way but they either were or will be advised by me personally.

# Contents

<b>1</b>	<b>Introduction</b>	<b>1</b>
<b>2</b>	<b>Theoretical Background of Radiometry</b>	<b>2</b>
2.1	General Principles of Radiometry . . . . .	2
2.1.1	Fundamental Laws . . . . .	2
2.1.2	The Planck Law . . . . .	4
2.1.3	The Wien radiation law . . . . .	6
2.1.4	The Rayleigh-Jeans Radiation Law . . . . .	6
2.1.5	The Wien Displacement Law . . . . .	6
2.1.6	The Stefan-Boltzmann Law . . . . .	7
2.2	Radiometer Systems and Principles . . . . .	7
2.2.1	Radiometer Receiver . . . . .	10
2.2.2	The Total Power Radiometer . . . . .	11
2.2.3	The Dicke Radiometer . . . . .	12
2.2.4	The Noise-Injection Radiometer . . . . .	13
2.2.5	Correlation Radiometer . . . . .	13
2.2.6	Other Radiometer Types . . . . .	13
<b>3</b>	<b>State of the Art in Radiometric Sensing</b>	<b>14</b>
3.1	Ground Based Sensing of Atmosphere . . . . .	15
3.1.1	Atmospheric Models . . . . .	15
3.1.2	Atmosphere Profiles . . . . .	16
3.1.3	Precipitation Sensing . . . . .	18
3.1.4	Conclusion . . . . .	21
3.2	Methods of Remote Sensing in Case of Fires . . . . .	22
3.2.1	Fires Detection . . . . .	23
3.2.2	Localization of Fires . . . . .	25
3.2.3	Conclusion . . . . .	29
<b>4</b>	<b>Thesis objectives</b>	<b>30</b>
<b>5</b>	<b>Atmosphere Sensing Methodology</b>	<b>31</b>
5.1	Introduction and Analysis of Atmosphere Sensing . . . . .	31
5.2	Measurement Site . . . . .	32
5.3	Atmospheric Models . . . . .	38
5.4	Atmospheric Events . . . . .	42
5.5	Method for Precipitation Prediction . . . . .	45
5.6	Method for Cloud Detection . . . . .	49
5.7	Conclusion . . . . .	53

<b>6</b>	<b>Fire Sensing Methodology</b>	<b>55</b>
6.1	Theoretical Introduction and Analysis of Fire Sensing . . . . .	55
6.1.1	Soil Emissivity . . . . .	56
6.1.2	Filling Factor . . . . .	57
6.1.3	Fire Emissivity . . . . .	58
6.2	Fire Detectability . . . . .	58
6.2.1	Airborne Sensing . . . . .	59
6.2.2	Human Figure Sensing . . . . .	62
6.2.3	Gasoline Fire . . . . .	64
6.2.4	Flood Trash Fire . . . . .	66
6.2.5	Wood Fire . . . . .	68
6.2.6	Straw Fire . . . . .	69
6.2.7	Fire Size and Temperature Influence . . . . .	76
6.3	Methodology of Fire Sensing . . . . .	80
6.4	Conclusion . . . . .	82
<b>7</b>	<b>Conclusion</b>	<b>84</b>

## Used symbols

Symbol	Quantity	Units
$A, A_F$	Area, fire spot area	$\text{m}^2$
$A_{ant}$	Antenna footprint area	$\text{m}^2$
$a, b$	Antenna footprint parameters	m
$CLW$	Cloud liquid water	$\text{g} \cdot \text{m}^{-3}$
$E_f$	Energy of radiation	$\text{kg} \cdot \text{m}^2 \cdot \text{s}^{-2}$
$F$	Antenna radiation pattern	-
$F_N$	Normalized antenna radiation pattern	-
$f$	Frequency	Hz
$G, G_0$	Gain, antenna gain	-, dB
$S$	Power Spectral Density	$\text{W} \cdot \text{Hz}^{-1}$
$H$	Height of the lower atmosphere	m
$B_d$	Directional spectral brightness	$\text{W} \cdot \text{m}^{-2} \cdot \text{Hz}^{-1} \cdot \text{sr}^{-1}$
$B_{di}$	Directional spectral brightness of incident radiation,	$\text{W} \cdot \text{m}^{-2} \cdot \text{Hz}^{-1} \cdot \text{sr}^{-1}$
$B_{da}$	directional spectral brightness of absorbed radiation,	$\text{W} \cdot \text{m}^{-2} \cdot \text{Hz}^{-1} \cdot \text{sr}^{-1}$
$B_{bb}$	spectral brightness of black body)	$\text{W} \cdot \text{m}^{-2} \cdot \text{Hz}^{-1} \cdot \text{sr}^{-1}$
$B_f, B_\lambda$	Spectral brightness	$\text{W} \cdot \text{sr}^{-1} \cdot \text{m}^{-2} \cdot \text{Hz}^{-1}$ , $\text{W} \cdot \text{sr}^{-1} \cdot \text{m}^{-3}$
$J_\lambda$	Source function	$\text{W} \cdot \text{sr}^{-1}$
$k_\lambda$	Mass extinction crosssection	$\text{cm}^2 \cdot \text{g}^{-1}$
$n$	Refractive index	-
$P$	Power	W
$p$	Atmospheric pressure	Pa
$PWV$	Precipitable water vapor height	cm
$q$	Filling factor	-
$R$	Resistance	$\Omega$
$\mathbf{r}$	Displacement vector	m
$s$	Layer thickness	m
$T$	Temperature	K
$T_X$	Temperature of an object $X$ : 0... atmosphere at the ground level $F$ ... fire $M$ ... mirror $S$ ... soil $V$ ... vegetation	K
$T_A$	Antenna noise temperature	K
$T_B$	Brightness temperature	K

Symbol	Quantity	Units
$T_{BX}$	Brightness temperature of an object $X$ : $A$ ... atmosphere $AR$ ... atmosphere reflected by vegetation $C$ ... cosmic background $F$ ... fire $SF$ ... soil with fire $SL$ ... sidelobes brightness temperature contribution $SV$ ... soil covered by vegetation $SFV$ ... soil with fire covered by a vegetation $V$ ... vegetation layer $VrS$ ... vegetation reflected by the soil and attenuated by a vegetation layer $VrF$ ... vegetation reflected by the fire and attenuated by a vegetation layer	K
$T_N$	Receiver-added noise temperature	K
$t$	Time	s
$t_A$	Atmosphere transmissivity	-
$t_V$	Vegetation transmissivity	-
$V$	Water vapor content	$\text{g} \cdot \text{m}^{-3}$
$\dot{Z}$	Impedance	$\Omega$
$z$	Height of an atmospheric variable	m
$\alpha, \alpha_d, \alpha_g$	Absorptivity, directional absorptivity, absorptivity of gaseous components	-
$\beta$	Antenna half-power beam width	deg
$\gamma$	Temperature lapse rate	$\text{K} \cdot \text{m}^{-1}$
$\delta$	Pressure lapse rate	$\text{Pa} \cdot \text{km}^{-1}$
$\epsilon, \epsilon_d$	Emissivity, directional emissivity	-
$\epsilon_X$	Emissivity of an object $X$ : $F$ ... fire $S$ ... soil $V$ ... vegetation	- - -
$\Theta$	Polar coordinate	rad
$\lambda$	Wavelength	m
$\lambda_m$	Maximum radiation wavelength	m
$\lambda_{m,n}$	Maximum radiation wavelength in transparent medium	m
$\rho$	Reflectivity	-
$\rho_0, \rho_W$	Absolute humidity at the sea level, water vapor density	$\text{g} \cdot \text{m}^{-3}$

Symbol	Quantity	Units
$\rho_d$	Material density	$\text{kg} \cdot \text{m}^{-3}$
$\rho_T$	Brightness temperature contrast	K
$\rho_V$	Vegetation reflectivity	-
$\sigma^2$	Noise signal variance	$\text{V}^2$
$\tau$	Integration time	s
$\tau_v$	Atmospheric optical depth	-
$\tau_f$	Frequency-dependent atmospheric optical depth	-
$\varphi$	Polar coordinate	rad
$\psi$	Incident radiation angle	rad
$\Phi$	Radiation flux	$\text{W} \cdot \text{m}^{-2}$
$\Phi_\lambda, \Phi_f$	Spectral radiation flux	$\text{W} \cdot \text{m}^{-2} \cdot \mu\text{m},$ $\text{W} \cdot \text{m}^{-2} \cdot \text{Hz}^{-1}$
$\Phi_{\lambda b}$	Spectral radiation flux of a black body	$\text{W} \cdot \text{m}^{-2} \cdot \mu\text{m}$
$\Omega, \mathbf{\Omega}, \Omega_F$	Solid angle, vector, solid angle of a fire spot	sr

## Used constants

Symbol Name	Value	Units	
$c$	Speed of light in vacuum	$2.99792458 \times 10^8$	$\text{m} \cdot \text{s}^{-1}$
$C_1$	First radiation constant	$3.747749 \times 10^{-16}$	$\text{W} \cdot \text{m}^2$
$C_2$	Second radiation constant	0.01438769	$\text{m} \cdot \text{K}$
$C_3$	Third radiation constant	$2.89776 \times 10^{-3}$	$\text{m} \cdot \text{K}$
$h$	Planck's constant	$6.6260755 \times 10^{-34}$	$\text{J} \cdot \text{s}$
$k$	Boltzmann's constant	$1.380658 \times 10^{-23}$	$\text{J} \cdot \text{K}^{-1}$
$M$	Molecular weight of atmosphere	28.97	
$M_0$	Atomic mass unit	$1.66 \times 10^{-27}$	kg
$\sigma$	Stefan-Boltzmann constant	$5.670373 \times 10^{-8}$	$\text{W} \cdot \text{m}^{-2} \cdot \text{K}^{-4}$

# 1 Introduction

Remote sensing methods have been and continue to be developed over the last few decades with rapidly increasing technical maturity. Throughout history, the surrounding world was perceived using simple methods whereby humans interacted directly with nature. Short-range fields (temperature, acoustic) were observed and investigated, and subsequent attempts to make sense of the observations focused on objects more and more remote from the Earth's atmosphere such as planets and stars rather than the closest space object, the Moon. Since direct sensing of these objects is either extremely difficult or impossible, it is only by measuring long-range fields that these remote objects can be effectively examined.

One of the first remote sensing attempts was done by Gaspard-Félix Tournachon. Tournachon first made pictures of Earth, essentially Paris, from a balloon. Since that time, 1858, when the images of Paris were distributed, mankind has gone on to such bold and daunting projects such as the launching of the Planck probe, in 2009, by the European Space Agency [1]. The probe is equipped with state-of-the-art radiometers which scan the temperature of the universe in three frequency bands from 30 GHz to 70 GHz [2].

The electromagnetic field is the most convenient means of conducting remote sensing and most widely used for sensing a wide-frequency spectrum allows scientists to observe the object from various points of view – in terms of sensing various states and process by one quantity.

Currently, new types of radiometers have been developed allowing us to integrate them with more complex measurement systems. Together, with the miniaturization of radiometric systems thanks to MEMS devices and system-on-chip technologies, radiometry boasts a new perspective for remote sensing from satellite, airborne or ground-based scanning.

New methodologies of remote sensing will be described in this thesis. Since the instrumentation for remote sensing is accessible and well developed, opportunities to propose new methodologies of measuring and datamining that are crucial in current research abound.

The main aim of this doctoral thesis is to propose new methodologies of remote sensing. The thesis is focused on currently used radiometric methodologies in remote sensing of the terrestrial atmosphere, and, fire detection and localization. The thesis is organized as follows. Following the introduction a theoretical background of remote sensing is introduced in the second chapter; Principles and fundamental laws are explained first with currently used radiometric concepts also being presented. In the third chapter, state-of-the-art remote sensing is discussed with general methodologies of ground-based atmosphere sensing highlighted, followed by a discussion of measuring atmospheric profiles. In relation to atmospheric profiles, precipitation detection and prediction is discussed. The second part of the third chapter is focused on methods of fire detection. In the fourth chapter the thesis objectives are proposed and defined. The main thesis focus consists of two parts: the first part deals with the new methodology of atmosphere dynamic effects (rain, clouds) sensing and is described in chapter 5. Next, the chapter 6 describes the methodology of remote fire detection and its properties from a microwave point of view.

## 2 Theoretical Background of Radiometry

### 2.1 General Principles of Radiometry

In this chapter, fundamental laws describing emissive properties of an object of any physical nature will be investigated. Only macroscopic scales and points of view will be considered. All physical objects that have a physical temperature higher than absolute zero emit a fluctuating electromagnetic field. Since there is non-zero internal energy, transitions between vibration-rotation levels of gas molecules, oscillations of molecules in liquids and in lattice of solid bodies can occur. This radiation has quantum characteristics and cannot be satisfactorily explained by classical Maxwell equations but by quantum theory as the radiation is emitted over a wide-frequency spectrum – mainly in radio and optic bands.

A strong relationship between radiation can then be recorded and the internal thermal structure of a body allows us to express the fundamental theorem: The fluctuation-dissipation theorem (FDT). Two approaches important for remote sensing are mentioned [3–6].

#### 2.1.1 Fundamental Laws

The first approach is the quasi-stationary FDT approximation called the Nyquist formula. H. Nyquist used an existing physical concept of a random electromotive force localized in an active circuit. He showed that the power spectral intensity (Wiener's spectrum)  $S(f)$  of the fluctuating electromotive force localized in a passive circuit is

$$S(f) = 4kT \operatorname{Re} \dot{Z}(j2\pi f), \quad (2.1.1)$$

where  $k$  is the Boltzmann's constant,  $T$  and  $\dot{Z}(j2\pi f)$  are temperature and impedance of the passive two-port circuit and  $f$  stands for frequency [3, p. 130]. The (2.1.1) gives the spectral power density in the unit intervals at positive frequencies. It is valid in the non-quantum band of frequencies and temperature ranges, assuming  $hf \ll kT$  where  $h$  is the Planck's constant. The final equation, the quantum-mechanical generalized formula which is valid for low temperatures and high frequencies,  $hf > kT$  is shown as follows [3, p. 130]:

$$S(f) = 2hf \coth \left( \frac{hf}{2kT} \right) \operatorname{Re} \dot{Z}(j2\pi f). \quad (2.1.2)$$

The theory of thermal fluctuations in electrodynamics arguably represents one of the most important applications of general theory of thermal radiation for macroscopic objects.

The second approach is geometric and optical based approximation: the Kirchhoff law, which considers states as thermodynamic equilibrium and detailed balance. The main idea of the Kirchhoff law posits that an object at thermal equilibrium has equal emissivity and absorptivity. The most simple expression of the Kirchhoff law is in the relation

$$1 - \epsilon = \rho, \quad (2.1.3)$$

where the parameter  $\epsilon$  stands for emissivity and  $\rho$  for reflectivity.

At first, emissive ability is investigated as the characteristic, emissive ability of a real physical object depends on many factors such as its temperature, physical and chemical composition, geometrical structure, surface roughness etc. The wavelength that corresponds to emitted radiation and the angle at which the radiation is emitted are the most interesting factors to note. For remote sensing the last two factors are crucial – to know the emissive ability in a required direction and the emissive ability at various wavelengths. These characteristics are called angular characteristics and directional characteristics. The directional emissivity is defined as follows [3, p. 218]:

$$\epsilon_d(\mathbf{r}, T, f, \mathbf{\Omega}, \dots) = \frac{B_d(\mathbf{r}, T, f, \mathbf{\Omega}, \dots)}{B_{bb}(T, f)}. \quad (2.1.4)$$

The directional emissivity is defined as the ratio of the directional spectral brightness of a real surface  $B_d(\mathbf{r}, T, f, \mathbf{\Omega}, \dots)$  to the black-body brightness  $B_{bb}(T, f)$  where  $\mathbf{r}$  is the coordinate of a point of space,  $\mathbf{\Omega}$  is radiation propagation direction. The spectral emissivity depends on the body's temperature, physical and chemical composition, intrinsic geometrical structure, roughness etc. The (2.1.4) is the most general expression because it includes wavelength, temperature and direction dependencies.

The absorbing ability of a body is the ratio of radiation flux absorbed by a body and radiation flux incident on the body. The spectral distribution of the incident energy is independent of temperature, physical properties of the body, or surface properties.

The general equation defining spectral radiation intensity  $B_d(\mathbf{r}, \mathbf{\Omega}, t)$  is defined by the following limit [3, p. 144]:

$$B_d(\mathbf{r}, \mathbf{\Omega}, t) = \lim_{dA, d\Omega, df, dt \rightarrow 0} \left[ \frac{dE_f}{dA \cos \Theta d\Omega df dt} \right], \quad (2.1.5)$$

where  $t$  is time,  $\Theta$  stands for the polar angle in which the radiation is considered,  $E_f$  is the energy of radiation in a specific frequency band and  $A$  is the projection surface to which radiation impacts. The directional absorptivity  $\alpha_d(\mathbf{r}, T, \mathbf{\Omega}, \dots)$  is the ratio of the spectral intensity of absorbed radiation  $B_{da}(\mathbf{r}, T, f, \mathbf{\Omega}, \dots)$  to the spectral intensity of incident radiation at specified wavelength and direction  $B_{di}(\mathbf{r}, T, f, \mathbf{\Omega}, \dots)$  expressed by [3, p. 219]

$$\alpha_d(\mathbf{r}, T, f, \mathbf{\Omega}, \dots) = \frac{B_{da}(\mathbf{r}, T, f, \mathbf{\Omega}, \dots)}{B_{di}(\mathbf{r}, T, f, \mathbf{\Omega}, \dots)}. \quad (2.1.6)$$

The complex Kirchhoff law relates the abilities of emitting and absorbing of energy by a physical body [7]. In the case of microwave sensing, the directional properties of the Kirchhoff law are necessary. From the equations (2.1.4) and (2.1.5) the energy radiated by a surface element from  $dA$  in the frequency band  $df$  within the angle  $d\Omega$  and over the time period  $dt$  can be calculated by relation [3, p. 219]:

$$dE_f = \epsilon_d(\mathbf{r}, T, f, \mathbf{\Omega}, \dots) B_{bb}(T, f) dA \cos \Theta d\Omega df dt. \quad (2.1.7)$$

It should be mentioned that the temperature  $T$  is considered as constant and isothermal at the element  $dA$ . When the ideal object is a black, closed cavity at temperature  $T$  the incident radiation intensity on the element  $dA$  in direction  $\mathbf{\Omega}$  is equal to  $B_{bb}(T, f)$ . Considering isotropical radiation in an ideal cavity, fluxes of absorbed and emitted radiation (2.1.6) (2.1.7) are equal and

$$\epsilon_d(\mathbf{r}, T, f, \mathbf{\Omega}, \dots) = \alpha_d(\mathbf{r}, T, f, \mathbf{\Omega}, \dots) \quad (2.1.8)$$

is valid [3, p. 219].

This posits relationship between the fundamental properties of physical substances and 2.1.8 is valid without limitations for all media in a state of thermodynamic equilibrium. To complete the contemplation, the Kirchhoff law can be applied even in situation when the thermal radiation is not in ideal equilibrium but cannot be applied in cases when the thermodynamic equilibrium conditions are strongly disturbed.

### 2.1.2 The Planck Law

In accordance with quantum statistic principles, a spectral volume density of radiated energy can be expressed by calculating the equilibrium distribution of photons, considering radiation where the field entropy is at maximum. For a gaseous medium, we can employ the Planck formula [8, p. 192]:

$$B_f(T, f) = \frac{2hf^3}{c^2} \frac{1}{[\exp(hf/kT) - 1]}, \quad (2.1.9)$$

where  $B_f$  is the frequency dependent spectral brightness. The spectral intensity of a black-body radiated into transparent medium can be expressed by formula

$$B_f(T, f) = \frac{2hf^3n^2}{c^2} \frac{1}{[\exp(hf/kT) - 1]}, \quad (2.1.10)$$

where  $n$  means refractive index and  $c$  stands for speed of light in vacuum. The black-body radiation is  $n^2$  times higher than when emitting into vacuum. By using wavelength  $\lambda$  instead of frequency, and considering refractive index independent on the frequency, the formula (2.1.10) turns into:

$$B_\lambda(T, \lambda) = \frac{2hc^2}{n^2\lambda^5} \frac{1}{[\exp(hc/n\lambda kT) - 1]}. \quad (2.1.11)$$

For remote sensing applications (radiometry, radioastronomy) an expression representing the amount of radiation energy emitted by the unit area of the black-body surface, at temperature  $T$  per unit time, in all directions, would be more appropriate. This relation, according to [3, p. 211] is expressed by

$$\Phi_\lambda(T) = \frac{C_1}{n^2\lambda^5} \frac{1}{[\exp(C_2/n\lambda T) - 1]}, \quad (2.1.12)$$

where  $\Phi_\lambda(T)$  is spectral radiation flux of a black body. Quantities

$$C_1 = 2\pi hc^2; C_2 = \frac{hc}{k} \quad (2.1.13)$$

are called the first and the second radiation constants, respectively. In Fig. 2.1 the spectral distribution of the surface density of a monochromatic black-body radiation flux  $\Phi_\lambda(T)$  is depicted. Wavelength dependencies of radiation flux for several values of absolute temperature are depicted.

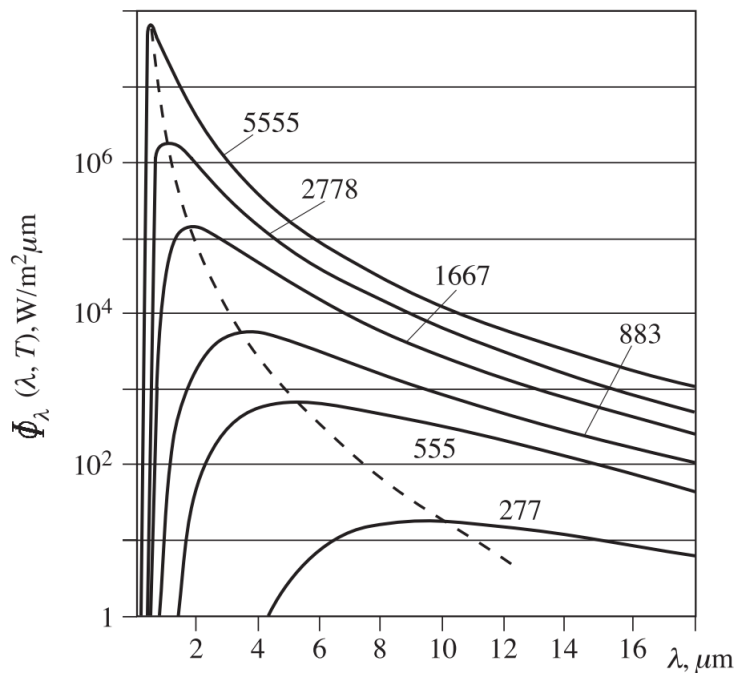


Figure 2.1: Hemispherical spectral radiation flux of black bodies for some values of temperature at specific wavelengths. Values of radiation flux maxima are marked by a dashed line [3].

Increase of the radiation energy with increasing temperature at all wavelengths is obvious. The next particularity is when the maximum of the spectral surface density of radiation flux approaches to shorter wavelengths with increasing temperatures. A conclusion can be derived: energy of radiation emitted at the short-wave extremity of the frequency spectrum increases in temperature faster than the energy of radiation corresponding to longer wavelengths. The result of the Planck law for energy distribution in the black body spectrum is the maximum value of the intensity of radiation which is emitted by a physical body at specified temperature and wavelength [2].

### 2.1.3 The Wien radiation law

The Planck law can be divided by a fifth power of temperature – the result is a more suitable form of equation (2.1.14) to avoid constructing curves for each temperature [3, p. 213]:

$$\frac{\Phi_\lambda(T, \lambda)}{T^5} = \frac{\pi B_\lambda(T, \lambda)}{T^5} = \frac{C_1}{(\lambda T)^5} \frac{1}{[\exp(C_2/\lambda T) - 1]}, \quad (2.1.14)$$

where  $B_\lambda$  is the spectral brightness. When  $\exp(C_2/\lambda T) > 1$  in the equation (2.1.14) can be reduced to the simple expression

$$\frac{B_\lambda(T, \lambda)}{T^5} = \frac{C_1}{\pi(\lambda T)^5} \frac{1}{\exp(C_2/\lambda T)}. \quad (2.1.15)$$

This equation is the Wien radiation law. In the range of  $\lambda T < 3000 \mu\text{m K}$  the expression determines maximal error in the limit of 1 %.

### 2.1.4 The Rayleigh-Jeans Radiation Law

The next approximation of the Planck's law can be obtained by developing the denominator in (2.1.14) into the Taylor series [3, p. 213]. When  $\lambda T > C_2$ , the series can be simplified by the second term of expansion and the equation (2.1.14) turns into form

$$\frac{B_\lambda(T, \lambda)}{T^5} = \frac{C_1}{\pi C_2} \frac{1}{(\lambda T)^4}. \quad (2.1.16)$$

This form of Planck's law is known as the Reyleigh-Jeans radiation law and the maximum error of this formula is up to 1 % for the values of  $\lambda T$  exceeding than  $7.8 \times 10^5 \mu\text{m} \cdot \text{K}$ . This range is out of the range usually considered in IR thermal radiation but can be successfully applied within the radio-frequency band. The frequency expression of spectral brightness  $B_\lambda$  of equation (2.1.17) is more convenient and widely used:

$$B_f(T, f) = \frac{2f^2}{c^2} nkT = \frac{2f^2}{c^2} nkT. \quad (2.1.17)$$

### 2.1.5 The Wien Displacement Law

The next quantity that should be mentioned is the wavelength  $\lambda_m$  to which the maximum surface density of radiated energy flux correspond. This limit is marked by the dashed line in Fig. 2.1. A maximum of emitted energy flux is moved to shorter wavelengths with the increasing temperature. The transcendental (2.1.18) equation is obtained by differentiating the Planck function and by equating to zero [3, p. 214]:

$$\lambda_m T = \frac{C_2}{5} \frac{1}{(1 - \exp(-C_2/\lambda_m T))}, \quad (2.1.18)$$

where  $\lambda_m$  is the wavelength of maximum radiation. The 2.1.18 has a solution:

$$\lambda_m T = C_3, \quad (2.1.19)$$

which is known as the Wien displacement law. The constant  $C_3 = 2.89776 \times 10^{-3} \text{m}\cdot\text{K}$ . When considering the black-body radiation into a transparent medium with refractive index  $n$  the Wien law turns into this equation

$$n\lambda_{m,n}T = C_3, \quad (2.1.20)$$

where  $\lambda_{m,n}$  means wavelength at which the radiation is in transparent medium maximal. By substitution of the wavelength from the Wien law (2.1.19) into Planck's equation (2.1.14), the following expression is obtained.

$$B_\lambda(T, \lambda_m) = T^5 \frac{C_1}{\pi C_3^5 [\exp(C_2/C_3) - 1]} \quad (2.1.21)$$

Stemming from this relation comes the fact that the maximum value of radiation intensity increases with the fifth power of temperature [3, p. 214].

### 2.1.6 The Stefan-Boltzmann Law

The last approximation of Planck's law is the Stefan-Boltzmann law. By integrating an amount of radiated energy  $\Phi_\lambda$  over all wavelengths, we obtain the total black-body radiation flux  $\Phi(T)$ , the equation

$$\Phi(T) = \int_0^\infty \Phi_\lambda(T, \lambda) d\lambda = \int_0^\infty \Phi_f(T, f) df = \pi \int_0^\infty B_f(T, f) df = n^2 \sigma T^4. \quad (2.1.22)$$

In (2.1.22) the Stefan-Boltzmann constant  $\sigma$  is equal to the expression

$$\sigma = \frac{2\pi^5 k^4}{15c^2 h^3}. \quad (2.1.23)$$

Using equation (2.1.22) the total power emitted by a body from 1 square meter at room temperature can be calculated. With the (2.1.17) (Reyleigh-Jeans law) the total power emitted by a body from 1 square meter at  $T = 300 \text{ K}$  within the radio-frequency up to  $10^{11} \text{ Hz}$  can be calculated [3, p. 215].

## 2.2 Radiometer Systems and Principles

Basic techniques and concepts of measuring thermal electromagnetic fluctuation radiation are described in this chapter. Theoretical fundamentals were explained in the previous chapter. Notions from practical remote sensing field are explained, as well as a description of systems determined for passive remote sensing. The concept and methodology of measuring by radiometers will be stated.

The procedure of remote sensing of spectral density consists of three basic components:

- Linear frequency filtering, parameters depends on physical features.
- Nonlinear quadratic signal transformation.
- Temporal accumulation of the measured signal determined for separating the constant component of the transformed signal.

At first, a short overview of spectrum characteristics should be mentioned. Signals coming from space have various forms of thermal radiation spectra. Signal can be white noise and may have a complicated spectrum of gas media radiation. In Fig. 2.2 the qualitative spectrum of electromagnetic emissions is depicted. It is shown in brightness temperature scale over a wide wavelength range. A basic characteristic of various radiating objects can be seen on optical band wavelengths up to the kilometer band: The approximate brightness temperature. The shortest wavelength has radiation from the Sun and Earth. This is followed by thermal radiation of gases. The gas absorption spectrum consists of a high number of narrow and sharp spectral lines. This is determined by the quantum character of the gas radiation intensity.

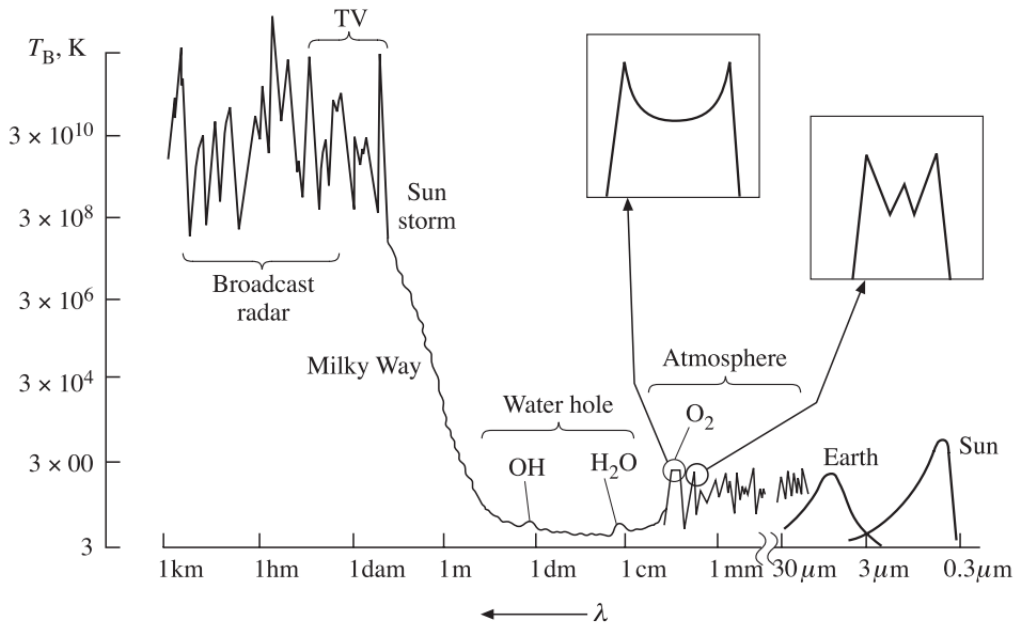


Figure 2.2: The qualitative picture of the spectrum of electromagnetic emissions and artificial radiations [3].

From the qualitative overview of the spectrum (Fig. 2.2) of electromagnetic emissions and artificial radiation, the importance of primary signal filtering is apparent. The whole spectrum can be divided in two parts: i) the broadened continuum part of the continuous spectrum; and ii) the multi-line absorption spectrum. Radiometers are working in both modes, the continuous spectrum radiometers and multichannel radiometer-spectrometers.

In accordance with the spectrum character, the concept of radiometric measuring systems can be implemented in two forms. The first form is an analogue, multichannel, filter system as seen in Fig. 2.3. Every frequency channel is filtered, amplified and recorded separately.

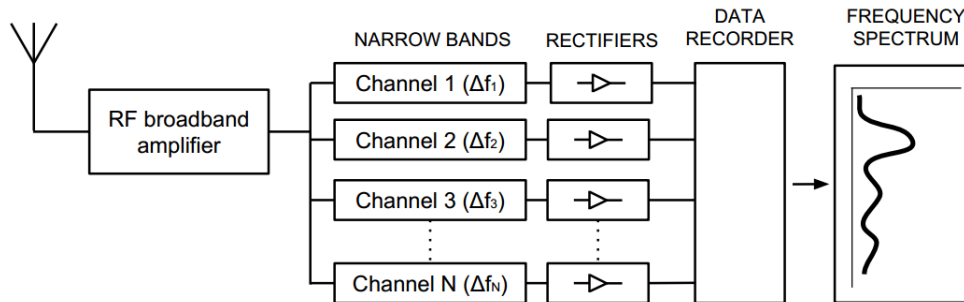


Figure 2.3: Analogue multichannel filter system receiver.

The second radiometer concept is the auto-correlation receiver. This type of radiometer produces an auto-correlation function transformed by Fourier transformation to a frequency spectrum. It is based on the decomposition of the time sequence of a basic signal in accordance with the multichannel scheme. The principal diagram is shown in Fig. 2.4.

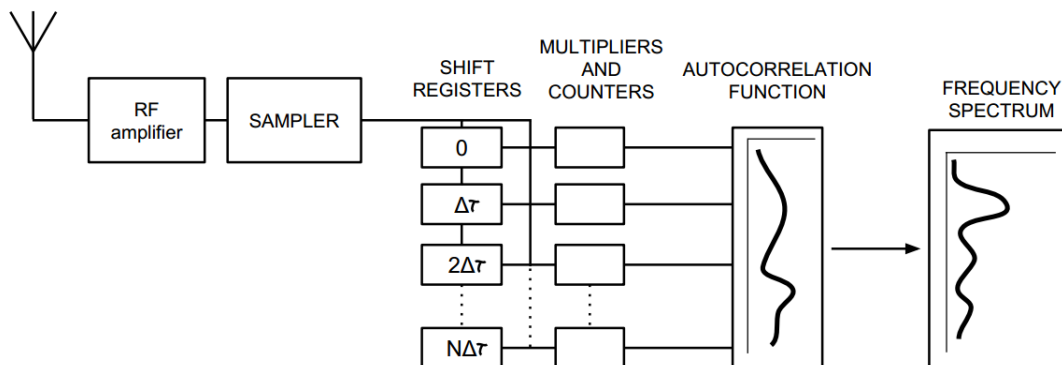


Figure 2.4: Autocorrelation receiver.

The increasing time delay is applied to each channel with a subsequent multiplication of the basic and delayed signals which are time-averaged. The instrument forms discrete values of the auto-correlation function and transforms it to spectral density by Fourier transformation to the original signal.

Both approaches are equally useful, but it depends the concrete application determines which is preferable.

### 2.2.1 Radiometer Receiver

The thermal radiation system should fulfill following criteria:

- Receive thermal electromagnetic radiation at specified frequency band from specified direction.
- Measure the signal with high sensitivity to record the thermal variation of physical objects.
- The possibility to assign measured radiation to the spatial coordinates of corresponding emitting objects.

With regard to the aforementioned criteria, the system should include the following components:

- An antenna system converting electromagnetic waves from free space to a measurable signal to ensure the observation of an object or surface.
- Radio-thermal receiver allowing measuring of the signal with good sensitivity and required accuracy.
- A preprocessing device that controls the antenna system, data acquisition, calibration and recording of the data.
- A system processing measured data that allows required post-processing.

The simple principal diagram of the receiver is depicted in Fig. 2.5.

The antenna system transforms electromagnetic waves from free space into modes and oscillations of electromagnetic waves in transmission lines. The antenna should rectify the wave resistance of free space to guiding systems. A convenient transmission line should be considered to determine whether a coaxial or waveguide is more appropriate for particular system. The antenna system properties are also crucial from the point of view of spatial-angular scanning. In each resolution element the system should receive a signal with a specific, required polarization. The last basic requirement of the antenna system is homogeneous frequency response over the measured band.

The radiometric system usually consists of a high-frequency low noise amplifier, a quadratic device and a low frequency filter. The amplifier amplifies the signal from an antenna to a quadratic transformer in the specified frequency band that correlates to the object under observation.

The object under observation, the source of radiation, has an internal resistance which corresponds to the energy received by the antenna system. The character of received signal can be described by a Gaussian random process with a variance value that corresponds to the intensity of the measured signal. In accordance with the Nyquist theorem, the noise signal is similar to the signal of a complex resistance  $\hat{Z}(j2\pi f)$ . Considering the equation (2.1.1) with impedance strictly resistive, the voltage noise signal variance is expressed in:

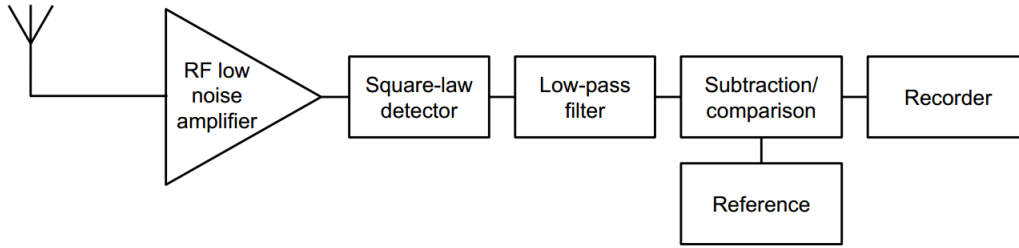


Figure 2.5: General radiometer system principal diagram.

$$\sigma^2 = 4kTR\Delta f, \quad (2.2.1)$$

where  $R$  stands for the internal resistance.

Assuming perfect matching conditions – equality of the source resistance and the input resistance, the well known Nyquist formula is expressed as the maximum power  $P_{max}$

$$P_{max} = kT\Delta f. \quad (2.2.2)$$

The formula (2.2.2) can be modified to the equation that will include input and output quantities as

$$P = k\Delta fG(T_A + T_N), \quad (2.2.3)$$

where  $G$  stands for the gain of the system,  $T_A$  for input antenna noise temperature and  $T_N$  stands for the noise added by the receiver itself. The  $T_N$  is independent of  $T_A$  and cannot be separated later. Considering the added noise, the general sensitivity formula is expressed as

$$\Delta T = k_1 \frac{T_A + T_N}{\sqrt{k_2 \Delta f_{HF} / k_3 \Delta f_{IM}}}, \quad (2.2.4)$$

where the  $k_1$  is the constant related to the switching signal of the radiometer (different for various switching signal shape),  $k_2$  stands for the frequency coefficient band constant – conversion to the equivalent frequency band and  $k_3$  is the time constant describing the period over which is the signal integrated.  $f_{HF}$  is the input frequency band and  $f_{IM}$  is the band of interfrequency.

### 2.2.2 The Total Power Radiometer

Since the basic principles of the remote sensing instrumentation and methodology were explained, particular radiometric receivers can be introduced. The first, and simplest, radiometer is the Total Power Radiometer (TPR). The TPR consists of only an input

frequency filter for frequency band selection, a detector (linear or square-law) and an integrator [9–12]. Presently the square-law detector is preferred. The signal is finally smoothed by an integrator – to reduce potential fluctuations. In Fig. (2.6) the principal diagram of the TPR is depicted.

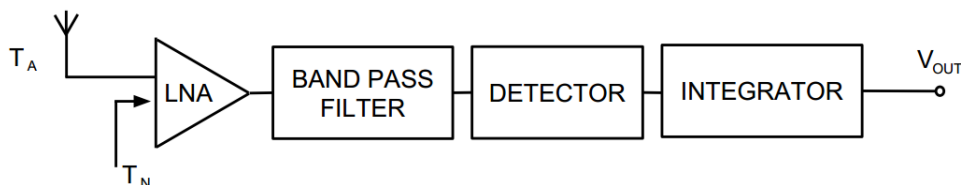


Figure 2.6: Total power radiometer principle diagram.

This type of radiometer is useful in applications where periodic and frequent calibrations can be done. The sensitivity of the TPR is generally expressed in (2.2.4).

### 2.2.3 The Dicke Radiometer

The Dicke radiometer does not directly measure antenna temperature, but it measures the difference between the antenna and some reference with a known temperature [9, 10, 12, 13]. The input of the radiometer is switched in turns between the antenna and the known reference. The switching frequency is usually in the order of 1 kHz to units of Hertz or slower depending on the application. The output of the square-law detector is multiplied by +1 or -1 with the switching frequency after the integration of the multiplied signal. The principal diagram of the Dicke radiometer is shown in Fig. 2.7.

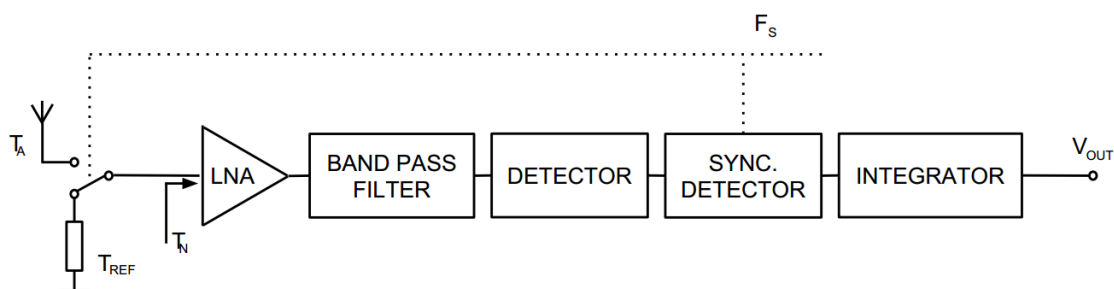


Figure 2.7: The Dicke radiometer principle diagram.

In the Dicke radiometer,  $T_N$  is reduced, but the gain is lower [10]. The radiometer in the Dicke design is more stable and immune to instabilities but because of integration switching time is shortened to half of the original period, this leads to decreased sensitivity. The sensitivity of the Dicke radiometer is expressed in (2.2.4).

### 2.2.4 The Noise-Injection Radiometer

The noise injection radiometer is based on the Dicke design with a servoloop added. Additional noise is introduced to the signal channel, yet the signal has same characteristics as the input signal. The intensity of the injected noise signal is in sum with input noise equal to the value of the reference temperature. Such measurements are referred to as null-balancing techniques. The intensity of injected noise is controlled by the servoloop. Thus, the noise injection radiometer is immune to gain and noise fluctuations [10, 12, 14]. The principal diagram of the noise injection radiometer can be seen in Fig. 2.8.

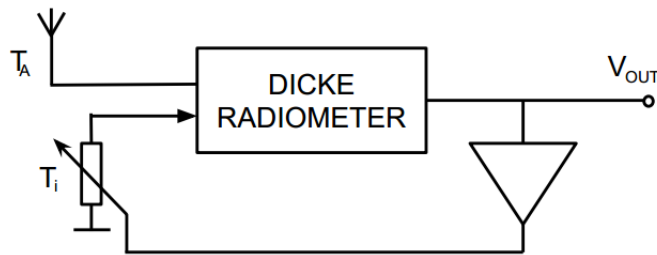


Figure 2.8: The noise-injection radiometer principle diagram.

The sensitivity of the noise-injection radiometer is generally expressed in (2.2.4).

### 2.2.5 Correlation Radiometer

The correlation radiometer is essentially a multichannel system and the two brightness temperatures are measured, as well as the correlation between them [15]. This can be used in a polarimetric radiometer [10, 14, 16] where vertical and horizontal brightness temperature are measured with their correlation to find Stokes parameters. In addition, an interferometric radiometer can be based on a correlation radiometer. The radiometer consists of two channels which are processed in the same way as in the Dicke design, but there is an additional feature: the complex correlator into which a signal is fed before detection and the real and imaginary parts of cross-correlation between the two signals is obtained. The principal diagram is shown in Fig. 2.9.

### 2.2.6 Other Radiometer Types

Basic radiometer systems and concepts have been described. Other types of radiometers are more or less combinations of previously mentioned types, though, an interesting concept is the Hybrid Radiometer [10] which works on the Dicke principle but with a direct A/D converter after signal detection. Integration and all subsequent processes are calculated by a processor, typically an FPGA (Field Programmable Gate Array). In Fig. 2.10 the simple principal diagram is shown.

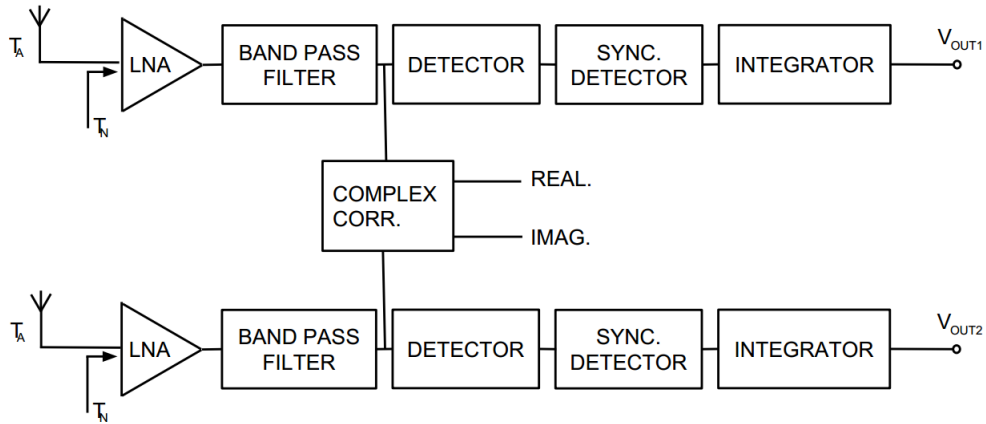


Figure 2.9: The cross-correlation radiometer principle diagram.

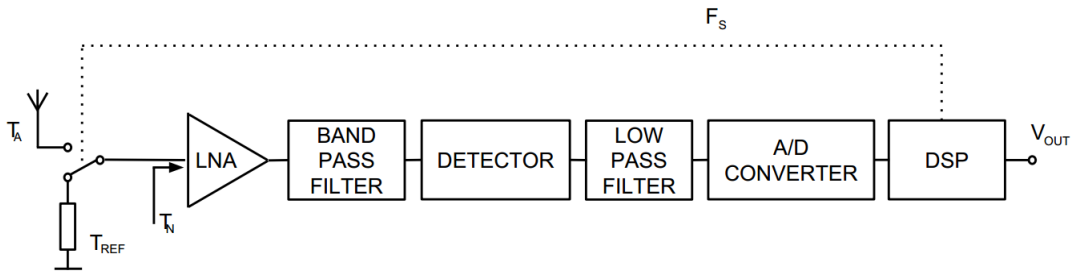


Figure 2.10: The hybrid radiometer principle diagram.

Other types of radiometers may have more than one reference, or, be a more complicated combination of the Dicke and noise-injection radiometers. Furthermore, the total power radiometer can be modified to obtain better gain stability, but all other possibilities are the result of a compromise between accuracy, sensitivity etc.

### 3 State of the Art in Radiometric Sensing

Rainfall is a key part of the hydrological cycle and much research has been conducted over a very long time. Precipitation (especially in the form of rainfall) is accompanied with heat release which drives a significant part of this cycle – the circulation of the atmosphere and water. Because of the diversity of the Earth’s surface, rain events should be examined with regards to the characteristics of the surroundings. Rainfall corresponds to various types of surfaces over which are different characteristics such as tropical rain events above forests and different rain events appears above the ocean surface. In this thesis, precipitation above solid land will be primarily examined.

Various types of communication links have been developed in the information age and

many today are wireless [17]. All these links and their reliability can be affected by atmospheric events related to rainfall or cloudiness. These atmospheric events can be observed by hydrometeorological radars or satellite cameras with satisfactory results and accuracy. With the radiometer these events can be examined from a different point of view: local parameters can be observed more accurately and precisely with a ground-based radiometer. This is the motivation for research in this branch. New, faster and more sensitive wireless links are being used and thanks to remote sensing of the atmosphere, reliability is kept at a high level.

### 3.1 Ground Based Sensing of Atmosphere

Passive atmosphere sensing is mainly performed in the visible part of the spectrum, as well as in infrared and radiofrequency bands. Visible and infrared waves radiated upwards from clouds are often reflected and emitted by top cloud layers and insufficiently correlated to the microphysical structure of clouds below the top layer. This is the reason why the visible/infrared information cannot be used satisfactorily for rain detection and prediction. Clouds are mainly related to rainfall in convective systems.

#### 3.1.1 Atmospheric Models

The composition of the atmosphere has a significant influence on radiated and received thermal fluctuation signals within the terrestrial atmosphere.

Barbaliscia measured atmosphere brightness temperature over four years [18] to obtain a statistical model of the atmosphere, brightness temperature and water content in Italy. The measurements were performed at two frequencies, 23.8 GHz and 31.4 GHz.

In Fig. 3.1 cumulative distributions of zenith brightness temperature at two frequencies are depicted. There are two regions in Figure 3.1, the first being the part of the curve measured below 1 % of the period of measurement. This happened when heavy rain clouds were sensed or rain events occurred. The other part of the curve corresponds to the remaining time where no clouds were present in the area. The lower signal (at 23.8 GHz) is more sensitive to liquid when the water vapor absorptive process is dominant. At the higher frequency, the 1 % period, clouds are more dense thus increasing brightness temperature over 150 K.

Since the atmosphere contains water vapor and liquid water which have a significant influence on thermal radiation, knowledge of the statistical model of water distribution is useful. The cumulative distribution of retrieved and calculated integrated water vapor is shown in Fig. 3.2.

Thanks to the dual-channel measurement the water vapor and integrated liquid water along the measured integration path could be calculated. Both can be expressed directly in  $\text{kg}\cdot\text{m}^{-3}$ . The calculation can be done just by a weighting function for both measured brightness temperature. For such measurement and calculation one channel of the radiometer must be sensitive to the water vapor and the second one to the liquid. For the full explanation and calculation see [18].

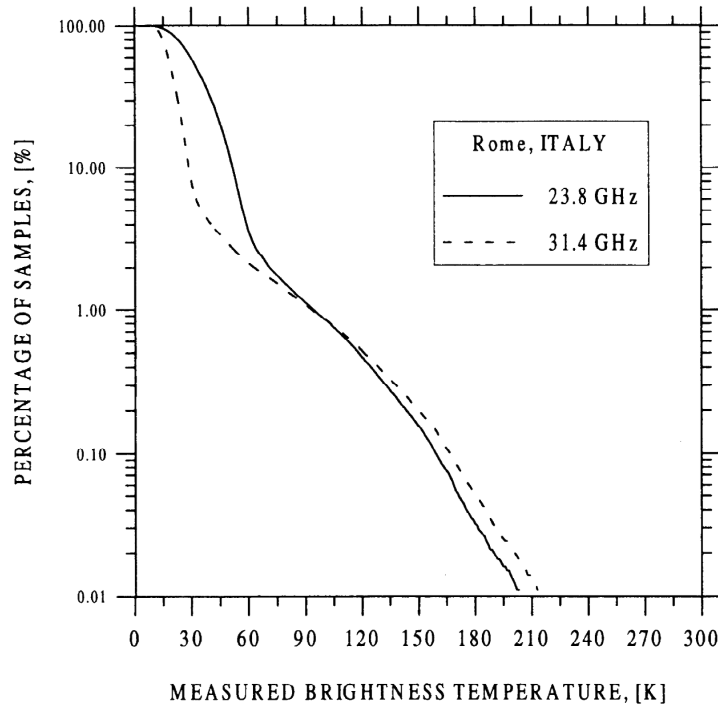


Figure 3.1: Cumulative distributions of zenith brightness temperature at 23.8 GHz and 31.4 GHz, average over 4 years [18].

### 3.1.2 Atmosphere Profiles

In the previous chapter, atmospheric characteristics were described. In this chapter the current state of atmospheric profiling and sensing of cloudiness is described. For atmospheric exploration, the radiometric profiler is usually used [19] [20] [21]. Profiling is generally done to obtain water vapor content which is related to other hydro-meteorological events that are investigated in this thesis.

Theoretical insight into atmospheric profiling was proposed by Li and Vivekanandan [22] [23]. With knowledge of some meteorological parameters, temperature and a subsequent water vapor profile can be obtained. The first approximation of the temperature profile is shown in this relation [22]:

$$T(z) = T_0 - \gamma z, \quad (3.1.1)$$

where  $T_0$  and  $\gamma$  stands for near-ground temperature and altitude temperature gradient respectively.  $T_0$  and  $\gamma$  can be directly calculated from radiometric-radiosonde observations by (3.1.2) and (3.1.3):

$$T_0 = 4\bar{T} - 6T_\sigma, \quad (3.1.2)$$

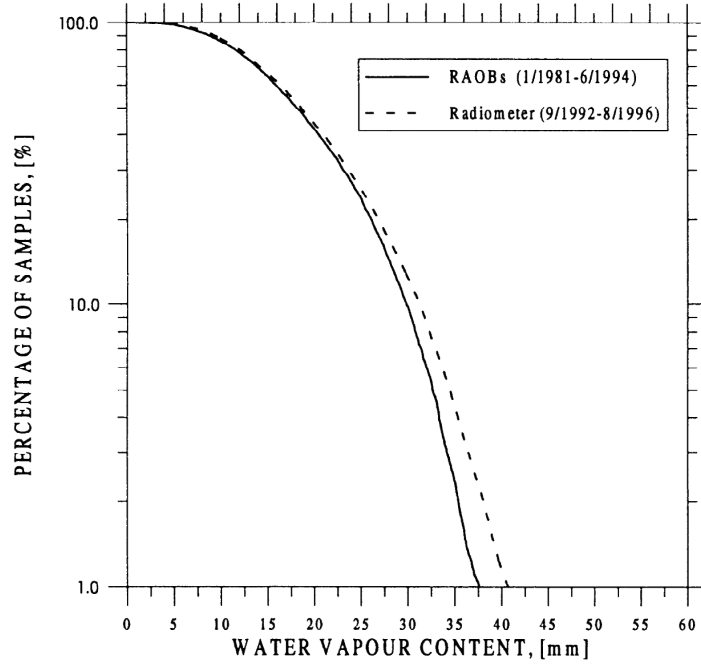


Figure 3.2: Cumulative distributions of retrieved and calculated integrated water vapor [18].

$$\gamma = \frac{6}{H} [\bar{T} - 2T_\sigma]. \quad (3.1.3)$$

In equations mentioned,  $H$  stands for thickness of the lower atmosphere and  $\bar{T}$  and  $T_\sigma$  are the mean and first moment of the temperature profile:

$$\bar{T} = \frac{1}{H} \int_0^H T(z) dz, \quad (3.1.4)$$

$$T_\sigma = \frac{1}{H^2} \int_0^H zT(z) dz. \quad (3.1.5)$$

For the vapor density profile characterization the precipitable water vapor  $PWV$  and integrated vapor column are used. The water vapor density profiles are generally approximated by the exponential function (3.1.6):

$$\rho_w = \frac{V}{PWV} \exp\left(-\frac{z}{H}\right), \quad (3.1.6)$$

where  $V$  stands for the water vapor content:

$$V = \int_0^H \rho_w dz, \quad (3.1.7)$$

and  $PWV$  means vapor scale height is

$$PWV = \frac{\int_0^H z \rho_W dz}{\int_0^H \rho_W dz}. \quad (3.1.8)$$

Water vapor profiles expressed by (3.1.6) can be used for radiative transfer models of ground-based radiometers. The parameters  $V$  and  $PWV$  can be obtained directly from radiometric measurements.

In [24, 25] atmospheric profiles, in accordance with previous theoretical insight, were investigated by a microwave radiometer. A radiometric profiler working on water vapor frequency channels was used for temperature and humidity soundings measurements. By fitting the shape of the water spectral absorption line, information related to the vertical distribution of water vapor can be obtained. Atmospheric profiles measured in 2001 by R. Ware are in Fig. 3.3. For comparative purposes, radiosondes were released to correlate results. Data measured by radiosonde and by radiometer are depicted with a strong, visible correlation. Next, measuring campaigns were measured by Cimini [20], Chan [26], Marzano [27] [28] and by Baxter [19] but mainly for locations other than central Europe with other atmospheric characteristics.

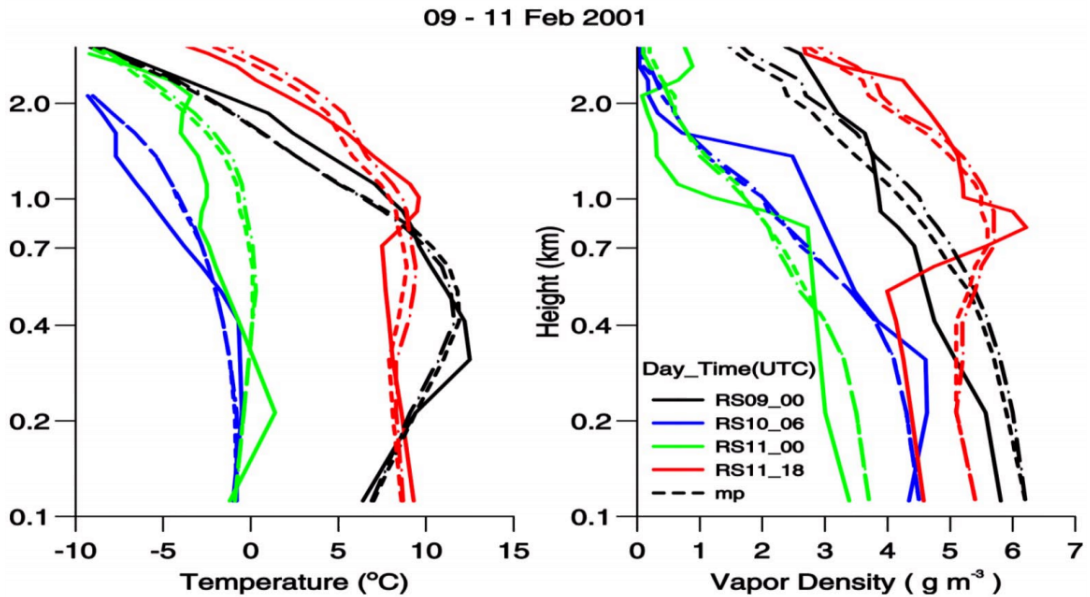


Figure 3.3: Temperature and vapor soundings measured by a radiosonde (solid line) and radiometer (dashed). Measured at Lindenberg, Germany [24].

### 3.1.3 Precipitation Sensing

Having an atmosphere model and profiles, precipitation sensing and prediction can be investigated. In 1999 J. Guldner performed water vapor sensing via a ground-based radiometer

over a 1-year period. Guldner proposed findings from measuring precipitable water vapor (PWV) and cloud liquid water (CLW) [29]. The data were measured in central Europe.

A pure state of the art precipitation detection and prediction model by a microwave ground-based radiometer was performed by H. Y. Won [30]. To estimate rainfall occurrence and intensity, a ground based microwave radiometer was used. Ordinary upper-air observation provided by a radioprobe 2 times a day cannot satisfactory substitute local on-line monitoring recording short-time precipitations. By statistical evaluation of measured brightness temperature, Guldner measured PWV and CLW increase of in a 30 minute time interval of before the rain started. Guldner measured the brightness temperature at two channels, 23.8 GHz and 31.4 GHz respectively. The band close to the water vapor spectral line is more sensitive to PWV, and the second band is more sensitive to CLW. Simultaneous determination of PWV and CLW was performed by the linear equations (3.1.9) and (3.1.10) in [29].

$$PWV = m_0 + m_1\tau_{f1} + m_2\tau_{f2} \quad (3.1.9)$$

$$CLW = n_0 + n_1\tau_{f1} + n_2\tau_{f2} \quad (3.1.10)$$

In equations mentioned  $\tau_f$  stands for the frequency-dependent total atmospheric optical depth as the sum of the optical depths of water vapor, liquid water and dry air. The  $n$  and  $m$  are in (3.1.9) and (3.1.10) numeric constants. The  $\tau_f$  is expressed by

$$\tau_f = \ln \left[ \frac{\overline{T_{BA}} - T_{BC}}{\overline{T_{BA}} - T_{BA}} \right]. \quad (3.1.11)$$

In (3.1.11)  $T_{BA}$  means measured atmosphere brightness temperature at frequency  $f$  and  $\overline{T_{BA}}$  is the mean radiation temperature of the atmosphere,  $T_{BC}$  stands for the cosmic background brightness temperature of 2.73 K. The  $\overline{T_{BA}}$  quantity can be expressed by (3.1.12):

$$\overline{T_{BA}} = \frac{1}{1 - \exp[-\tau_f]} \int_0^{\tau_f} T(z) \exp[-\tau_f(z)] d\tau_f(z). \quad (3.1.12)$$

The obtained results of PWV and CLW are depicted in Fig. 3.4 and 3.5 respectively. Deviations from the 2-h mean are used.

In the Gueldner's work Won continues with his precipitation prediction by a ground-based radiometer [30]. Won has used microwave radiometer that measures 8 water vapor channels in the K-band and 14 oxygen channels in the V-band. Data are converted by the Planck law. In the mission surface meteorological parameters (temperature, relative humidity and pressure) were measured. Also an infrared thermometer is used for water vapor and liquid water profiles measurements in the new method. Since the brightness temperature is the primary measured parameter and PWV and CLW are secondary parameters with worse accuracy only the brightness temperature is considered in the algorithm.

Predictability of precipitation events can be proved by using 15-minute moving data accumulation. If in the 15-minute interval a statistically significant rainfall is detected, it

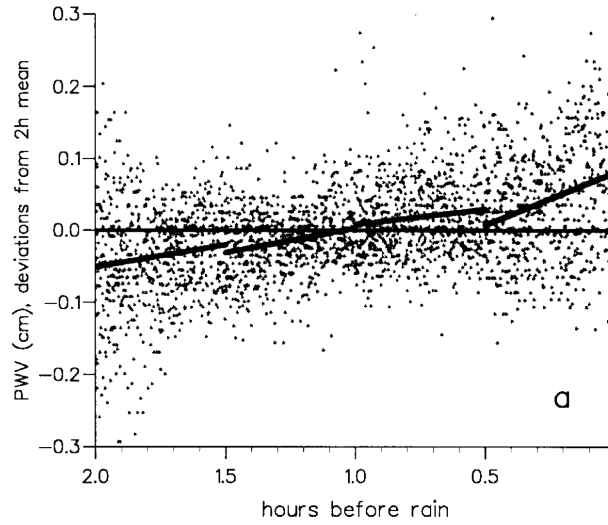


Figure 3.4: Deviation of PWV from corresponding 2-h mean before precipitation in summer. The solid line is linear regression for 30 minutes interval [29].

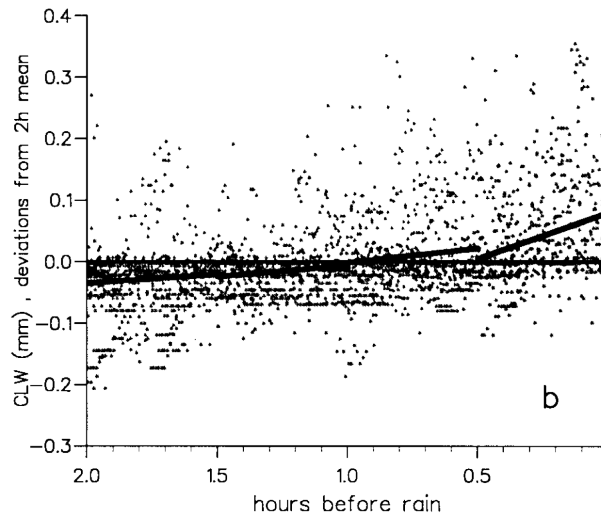


Figure 3.5: Deviation of CLW from corresponding 2-h mean before precipitation in summer. The solid line is linear regression for 30 minutes interval [29].

is considered as the rain event. Two datasets are used of the analysis – rain record data set (RR) and no-rain record (NR) dataset. When an event occur and another one occur within 2 hour period after the first one, it is regarded as the same event. The 2-h interval is generally used to keep preceding time long enough. If the longer interval is used, fewer number of events will be recorded. Brief diagram of the rain event definition is in Fig. 3.6. Seasonal and weekly dependences of the measured data are eliminated by taking RR and

NR from data time-shifted by 7 days.

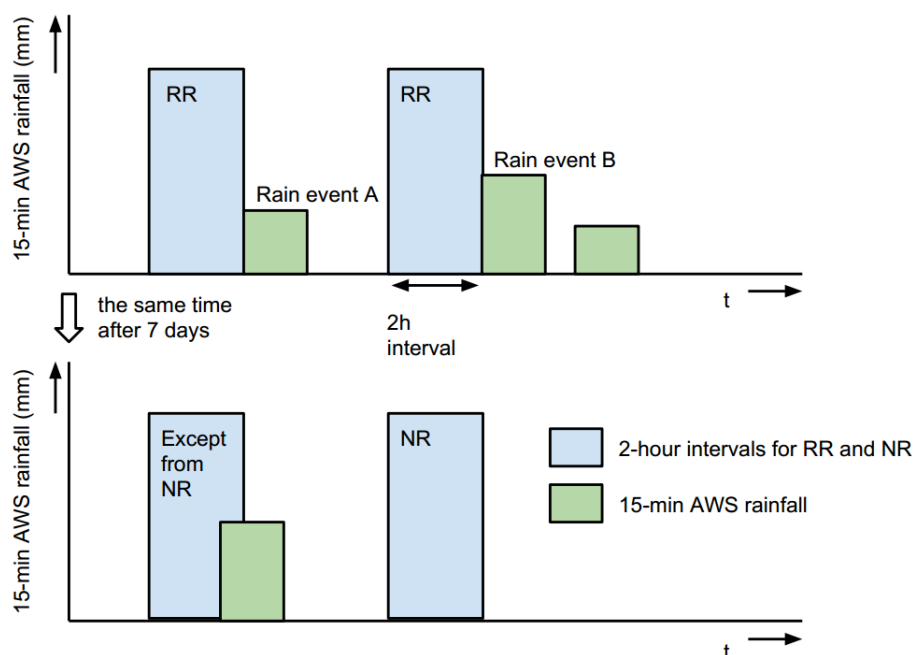


Figure 3.6: A diagram for the definition of rain events and no-rain period. Triangles means 15 minute interval from the automatic weather system.

Typical results of Won's method are depicted in Fig. 3.7 and in Fig. 3.8 respectively. In figures averaged differences of brightness temperature in period of 2 h before the rain starts can be seen. The difference of RR and NR graphs is obvious.

From the pictures above can be seen that the brightness temperature is widely distributed. In other frequency channels has the distribution of measured brightness temperature even bigger variation. So the water vapor RR and NR datasets are used as a factor for rain events prediction as well as the other bands. As a functional proof of this method the correlation between the brightness temperature and rainfall amount can be calculated. In Fig. 3.9 a gradual increase of lagged correlation coefficient is depicted. The main growth is 30 minutes before the rain, as can be seen in Fig. 3.7.

### 3.1.4 Conclusion

There is a lot of research groups that are recording brightness temperature at various frequencies and several approaches are used in order to detect and forecast rain. The most similar solution of the rain forecasting proposed Won's research group but unfortunately it is in the early stage with minimal validation. Other research groups are mostly using multi-frequency sensing by a radiometer at the water absorption frequency to obtain the liquid and water vapor content in the sensed area.

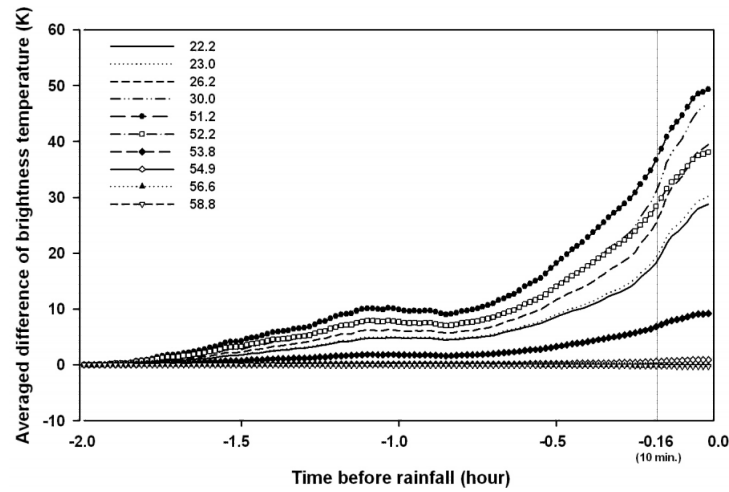


Figure 3.7: Time averaged brightness temperature differences in 2-hour period before the rain event. RR datasets measured at water vapor frequency channels are used [30].

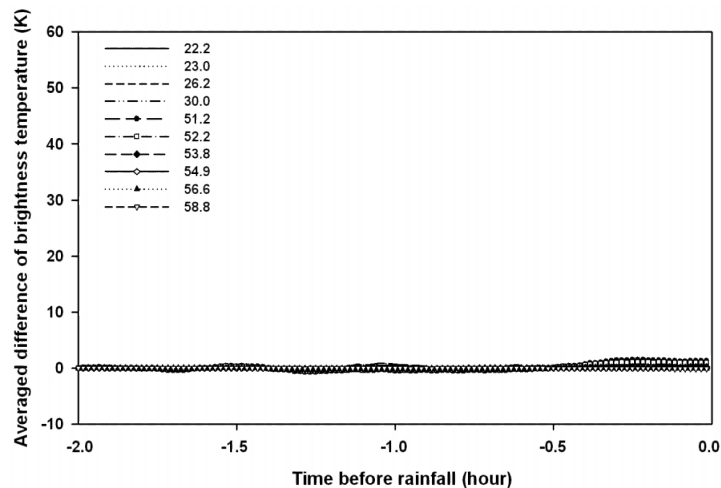


Figure 3.8: Time averaged brightness temperature differences in 2-hour period before the rain event. NR datasets measured at water vapor frequency channels are used [30].

### 3.2 Methods of Remote Sensing in Case of Fires

As well as the atmosphere being studied to detect and predict undesirable atmospheric effects, fires can be sensed by measuring thermal radiation too. Every year thousands of square kilometers are destroyed by forest fires causing huge damage to the environment and people. A variety of fires can be distinguished: fires in buildings, open space fires, fires of dangerous chemicals etc. Detecting fire by radiometry has great potential. Current fire detectors, from a remote sensing point of view, are based on infrared satellite sensors,

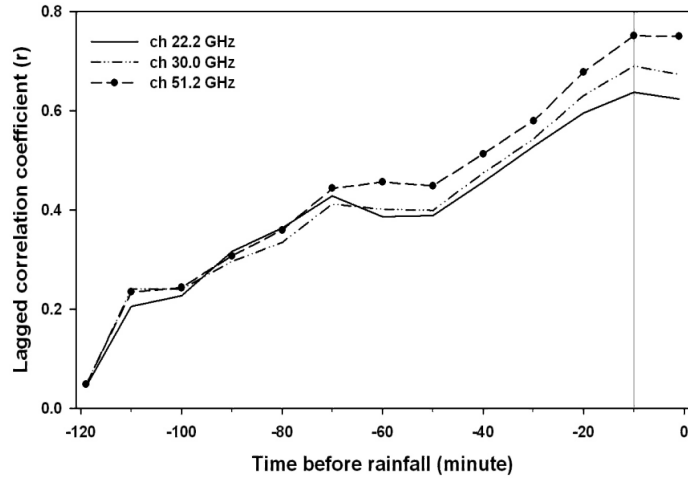


Figure 3.9: The lagged correlation coefficient between the measured brightness temperature differences and precipitation amount at three frequency channels [30].

though problems exist as infrared sensors may not detect fire hidden under vegetation or other forms of coverage. Since microwaves can penetrate the vegetation layer, which is opaque for visible or IR radiation, radiometers can be successfully used.

### 3.2.1 Fires Detection

Radiometers for the purpose of fire detection are well designed by the group of F. Alimenti. Alimenti has designed several radiometers for various purposes [31–34] and the ability to detect a fire was proved. The ability of fire detection was performed by measuring of the open wood fire. For this purpose the microwave radiometer was developed. The working frequency was 12.65 GHz with the bandwidth of 100 MHz. A low-cost radiometer was used to measure thermal radiation in accordance with the European standard EN54. The standard is used to certify optical and temperature fire detectors. The standard also describes the fire sizes and types in order to simulate the wild fires etc. Materials of the fuel is mentioned as well. In Fig. 3.10 the course of experiment is depicted.

The brightness temperature increase was from 0.2 dB to 1.5 dB for various solid fuels used in the experiment. No dependency of the used frequency in the range of chosen band was observed. Thus, there is no strong requirement on the frequency band. Also the brightness temperature differences are more important than the absolute value of temperature so the calibration of the radiometer is not essential in this application.

Possibility of using radiometric spectroscopy was considered but the increase of radiated power is not significant enough. A liquid fuel, the most frequent source of fire, causes the increase only of 0.2 dB [32]. The resolution requirements in comparison with a solid fuels would lead to high price of the instrument. Thus the low-cost radiometers cannot be used for the spectroscopy exploring.

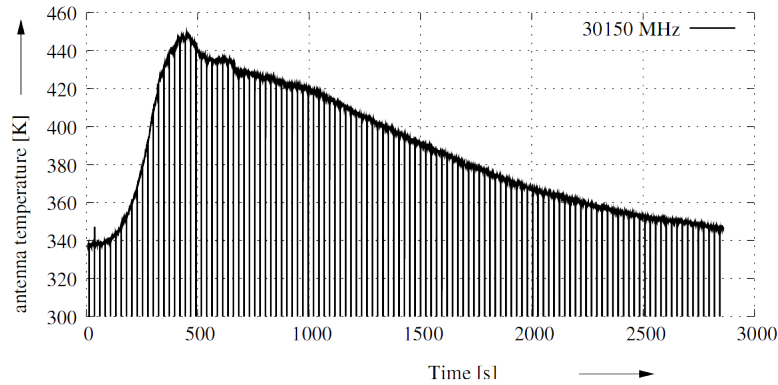


Figure 3.10: Measured brightness temperature of a wood fire. Experimental procedure performed to prove ability of fire detection in accordance with EN54 standard. The signal dropouts are caused by the radiometer calibration [32].

The outdoor measurement to detect a fire by the radiometer can be performed. An example of the measurement in Fig. 3.11. The increase of the brightness temperature is measurable by a low cost radiometers. The brightness temperature can increase by 8 K in the case of small fire ( $0.2 \text{ m}^2$ ), sensing of extensive, massive fire can produce the brightness temperature contrast in order of tens Kelvins [32]. The signal increase marked by the "A" letter is caused by a human presence at the beginning of the fire.

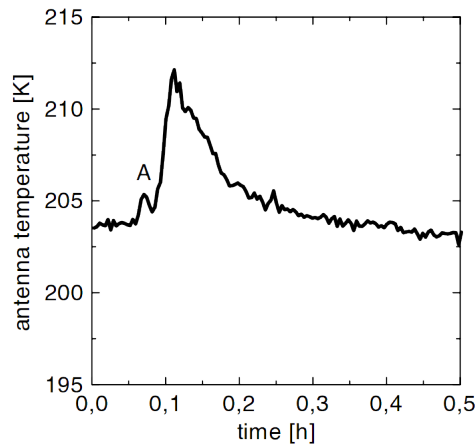


Figure 3.11: Measured brightness temperature of a wood fire in a open space [32].

Next possible issue with the radiometric sensing of fires can be caused by the fire coverage [35,36]. Currently, results of measuring of fire covered by plasterboard and concrete are available. In the Fig. 3.12 a situation with open fire and its coverage is depicted. The contrast of the measured brightness temperature in case of fire and without a fire is about 27 K [32]. A plasterboard placed in front of the fire causes reduction of the measured

brightness temperature contrast by 10 K. Also the time delay of possible detection increases. Nevertheless, the fire can be recognized in comparison with the concrete coverage where the contrast of brightness temperature is negligible.

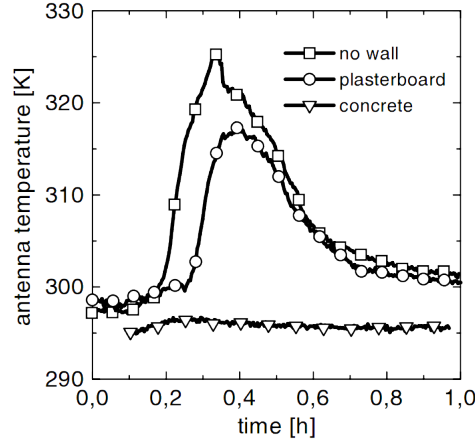


Figure 3.12: Measured brightness temperature of open-space fire that is covered by plasterboard and concrete and without any coverage [32].

### 3.2.2 Localization of Fires

In this chapter current methods of fire localization by radiometer will be described. As it was mentioned, infrared cameras can locate the fire position. Naturally, with the limitations related to transparency of the coverage. By the radiometric sensing of fire also a picture of the situation can be taken. Subsequently the current 2D sensing of the radiation will be described.

At first the scan geometry should be described. The antenna beam shape must be taken into account. Considering the ground-based radiometer the situation is depicted in Fig. 3.13.

The power pattern  $F(\Theta, \varphi)$  is expressed in the equation

$$T_A = \frac{\iint_{4\pi} T_B(\Theta, \varphi) F(\Theta, \varphi) d\Omega}{\iint_{4\pi} F(\Theta, \varphi) d\Omega}, \quad (3.2.1)$$

where  $\Theta$  stands for the elevation angle,  $\varphi$  is the azimuth angle and  $d\Omega = \sin \Theta d\Theta d\varphi$  is the elemental solid angle.

Two approaches are used in the remote scanning, the conical scanning and the linear scanning. Example of antenna footprints prepared for image scanning in the conical scanning pattern is in Fig. 3.14.

In Fig. 3.15 the linear scanning footprints pattern is depicted. The conical pattern is frequently used because during the scan it is necessary to adjust the antenna direction

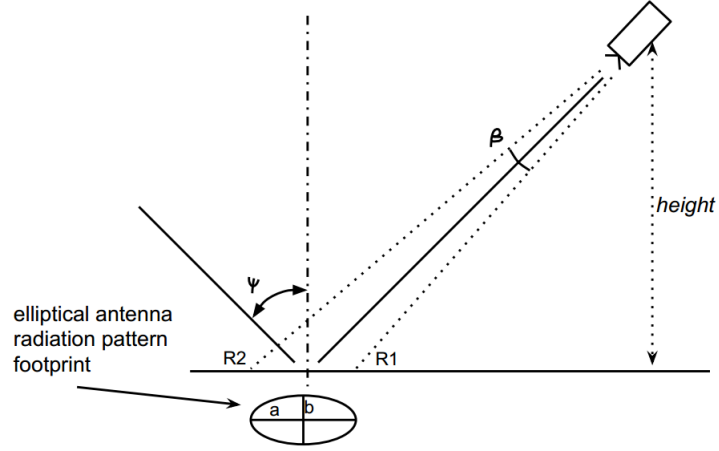


Figure 3.13: The measured scene by a radiometer placed in the height of  $h$ .  $\psi$  is the incident angle,  $\beta$  is the antenna half-power beam width,  $R1$  and  $R2$  is the closest and furthest point of the sensed footprint. The footprint is elliptical with  $a$  and  $b$  major and minor radius, respectively.

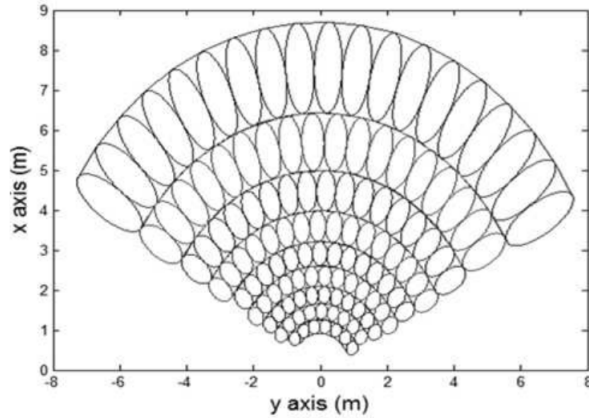


Figure 3.14: Conical scanning pattern. Half-power beam footprints are plotted as an image matrix for a microwave sensing [37].

only by one angle. But the image has slightly irregular shape in comparison with linear scanning.

Since the scanning methods are proposed the brightness temperature can be measured in an open space. A typical situation with the homogeneous soil without any fire will be described. The observed brightness temperature can be expressed by

$$T_B = T_s \epsilon_s + (1 - \epsilon_s)(T_{BA} + T_C e^{-\tau_\infty}), \quad (3.2.2)$$

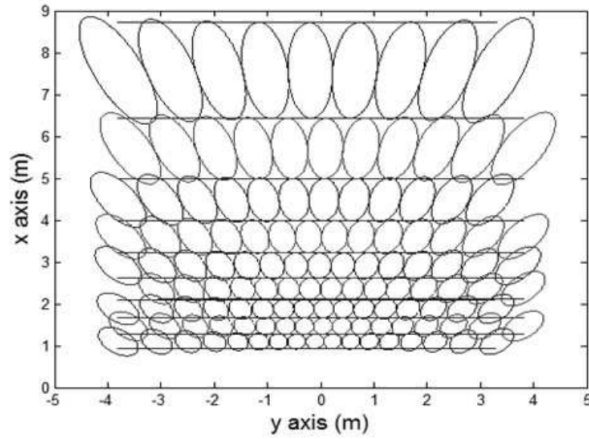


Figure 3.15: Linear scanning pattern. Half-power beam footprints are plotted as an image matrix for a microwave sensing. Disadvantage is necessity of two angles adjusting during one line sensing [37].

where  $\epsilon_s$  and  $T_s$  are the emissivity and the physical temperature of the soil respectively.  $T_{BA}$  stands for brightness temperature of atmosphere, the  $T_C$  is the cosmic background radiation and  $\tau_\infty$  is the atmospheric opacity. The radiometer is ground-based so the up-warding radiation can be neglected. A typical measured pattern of the scenario with homogeneous soil is shown in Fig. 3.16.

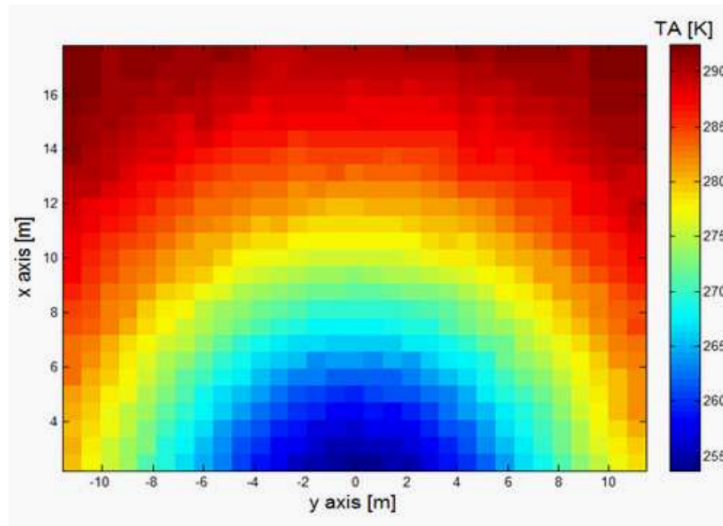


Figure 3.16: Image of the brightness temperature without fire measured by a microwave radiometer [37].

Brightness temperature measured in situation with soil with fire can be described by

$$T_{BSF} = [T_F \epsilon_F + (1 - \epsilon_F)(T_{BA} + T_C e^{-\tau_\infty})]q + T_B(1 - q), \quad (3.2.3)$$

where  $\epsilon_F$  and  $T_F$  are the emissivity and the average temperature of the fire respectively and  $T_B$  is the brightness temperature obtained by 3.2.2. The parameter  $q$  is the filling factor defined as the power received from a fire source relative to that which would be received from a source with the same temperature but covering the whole antenna footprint.

By relation (3.2.4) the brightness temperature of soil with fire covered by a canopy can be calculated

$$T_{BSFV} = T_{BSFV} + T_{BSV} + T_{BV} + T_{BVrS} + T_{BVrF} + T_{BAR}, \quad (3.2.4)$$

where the quantity  $T_{BSFV} = \epsilon_F T_F t_V q$  stands for emission from fire attenuated by the vegetation canopy with transmissivity  $t_V$ ;  $T_{BSV} = \epsilon_S T_S t_V (1 - q)$  is emission of the bare soil attenuated by the vegetation,  $(1 - q)$  is the factor describing footprint coverage by the fire;  $T_{BV} = \epsilon_V T_V$  is direct emission of the vegetation with physical temperature  $T_V$  and emissivity ( $\epsilon_V$ );  $T_{BVrS} = (1 - \epsilon_S) T_{BV} t_V (1 - q)$  is downward emission of the vegetation reflected by the soil and attenuated by the vegetation layer;  $T_{BVrF} = (1 - \epsilon_F) T_{BV} t_V q$  is downward emission of the vegetation reflected by the fire and attenuated by the vegetation;  $T_{BAR} = \rho_V (T_D + T_C e^{-\tau_\infty})$  is downward brightness temperature emitted by sky and reflected by the vegetation with  $\rho_V$  vegetation reflectivity.

By measuring of  $T_{BSF}$  in one of described scanning pattern the image of scenery with fire can be obtained, as is shown Fig. 3.17.

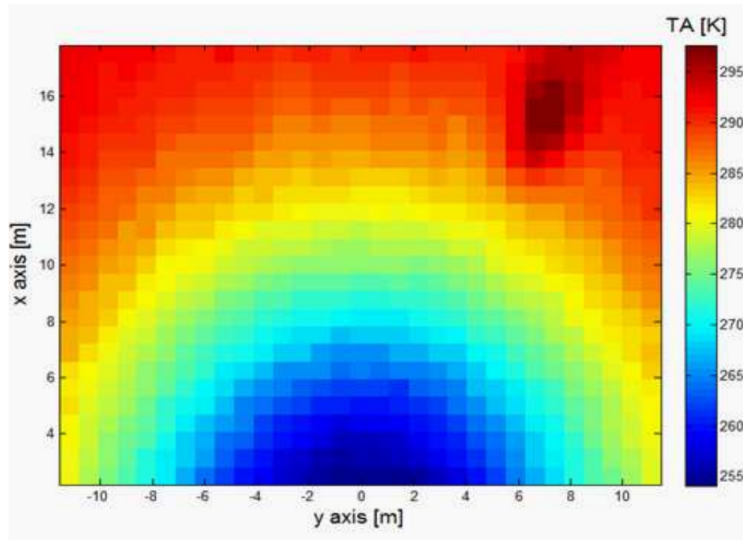


Figure 3.17: Image of the scenery with fire where the brightness temperature is measured by a microwave radiometer [37].

The measuring of brightness temperature allows imaging of sceneries from the new point of view. Some problems regarding the time of scanning or the resolution of image are still present but this area is very promising for investigation.

### **3.2.3 Conclusion**

The fire sensing by a microwave radiometer is still at the beginning at this time and not many research groups are involved in this topic. There is an initial interest from the F. Alimenti's group in the topic of fire remote sensing but it is in very early stage and mostly focused on the physical radiometric system. Radiometers and their design and system properties for fire sensing are under interest but not the methodology. Not many measurements were done on site in order to discover fire properties from the microwave point of view.

## 4 Thesis objectives

The doctoral thesis proposes new methodologies of microwave radiometric sensing. Since a lot of atmospheric and environmental effects decrease reliability of newly planned wireless links or sensors (either microwave or optical) and with recent advances in radiometer technology (e.g. miniaturized MEMS based radiometers which allow to construct small, cheap and portable radiometric devices), new algorithms for undesirable effects detection and prediction have to be proposed. Two main objectives will be solved.

- I The thesis will be primary focused mostly on derivation of methodologies for prediction and detection of dynamic atmospheric changes relating to rains. In order to obtain statistically significant amount of measured data, a measuring campaign will be accomplished. Specific atmospheric effects, e.g. cloudiness and precipitation, will be analyzed based on samples of brightness temperatures. A methodology to predict and detect rain events, and clouds from brightness temperature dependencies will be proposed and verified.
- II Each summer thousands of square kilometers of forests are burned out with huge impact on both environment and economy. Precise detection and localization of fires is a contemporary well demanded service in order to secure human lives and assets. In order to improve the detection and localization of fires, microwave radiometers can be used for the ground scanning. In comparison of radiometer with IR camera the microwave instrumentation brings the advantage to sense even through obstacles or smoke. In the second aim of the thesis, the detectability of a particular fire types by aerial microwave radiometer will be investigated with respect to specific parameters like the fire size, temperature and especially radiometer sensitivity. There are a few papers published about the fire sensing topic but mainly focused on hardware development and not on methodologies of measurement approaches and data processing. Several measurements will be performed in order to study the fire from the radiometric point of view and a new methodology will be described.

## 5 Atmosphere Sensing Methodology

### 5.1 Introduction and Analysis of Atmosphere Sensing

Microwave waves propagation through the atmosphere is a natural effect with very complex theoretical description. For the start the basic theory of radiative transfer should be mentioned. The basic part is the propagation through a matter. Considering the passive medium (no external artificial radiation sources), a radiation is weakened by the interaction with the medium. Assuming the radiation intensity  $B_\lambda$  turns to  $B_\lambda + dB_\lambda$  by passing through a medium with thickness of  $ds$  and this can be described by

$$dB_{\lambda 1} = -k_\lambda \rho_d B_\lambda ds, \quad (5.1.1)$$

where  $\rho_d$  stands for the material density and  $k_\lambda$  is the mass extinction cross section of radiation at the wavelength  $\lambda$  [38, p. 27]. So the extinction of the radiation is caused by both, absorption and scattering in the medium. But the medium has its own radiation and this can be boosted by the thermal emission of the medium and also by the scattered radiation from other natural sources. A source function should be taken into account defined by the term

$$dB_{\lambda 2} = j_\lambda \rho_d ds, \quad (5.1.2)$$

where the  $j_\lambda$  is the coefficient of the source function. The final radiation intensity difference can be then expressed according to [38, p. 27] by

$$dB_\lambda = -k_\lambda \rho_d B_\lambda ds + j_\lambda \rho_d ds, \quad (5.1.3)$$

and the source function will be described by

$$J_\lambda \equiv j_\lambda / k_\lambda. \quad (5.1.4)$$

So the final radiative equation can be afterwards expressed by

$$\frac{dB_\lambda}{k_\lambda \rho_d ds} = -B_\lambda + J_\lambda. \quad (5.1.5)$$

The final term does not depend on a coordinate system. Such equation can be the base for atmosphere radiation transfer equations and models [38].

Below frequencies of approx. 22 GHz, absorption is the main process for microwave radiative transfer. Although scattering as well occurs, it is of secondary significance. Around frequency of 60 GHz, scattering is more important than absorption (except strong oxygen absorption line). Between 20 and 60 GHz, both scattering and absorption processes have to be considered.

## 5.2 Measurement Site

In order to validate brightness temperature changes and to obtain better statistical insight, an experimental site was set up in the university campus of the Faculty of Electrical Engineering, Czech Technical University in Prague (CTU), Czech Republic. The experimental measuring system consists of a ground based radiometric station and a set of weather sensors located at two meteorological stations.

The microwave radiometer based on the Dicke switch design [10] was utilized for long-term monitoring of brightness temperature. The lower working frequency range of 10.68 to 11.49 GHz (satellite band) was chosen to measure the thermal deviation for two main reasons - we wanted to avoid the strong absorption line of water vapor in the atmosphere at 22.2 GHz, which would cause partial biasing of measurement results, and secondly because the technology for satellite receivers was available. Using frequency band lower than 37 GHz leads to measurements of the brightness temperature that responds more to rain or cloud liquid emissions. Contrary to band with frequencies higher than 37 GHz, where brightness temperature mainly responds to cloud ice scattering [3].

The vertically pointed radiometer was deployed on the roof of the CTU building, 36 m above the ground level, therefore it was isolated with respect to the brightness temperature contribution in a given antenna (receiving) radiation pattern of received noise signal from adjacent buildings.

As a receiving antenna the parabolic reflector antenna with the diameter of 64 cm was used. Radiation pattern of the antenna is depicted in Fig. 5.1.

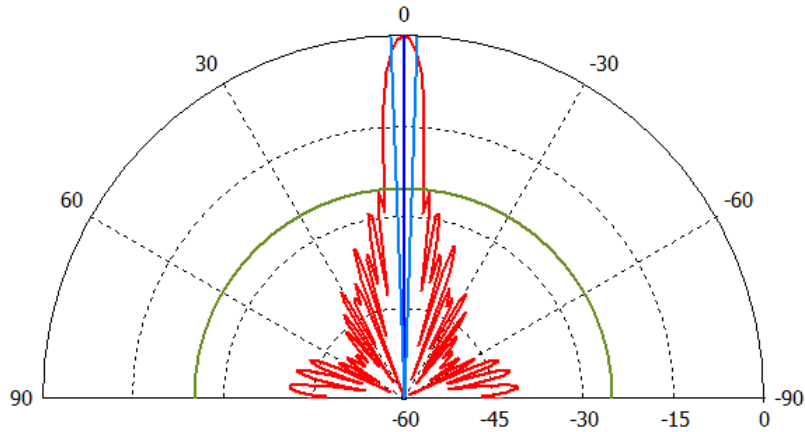


Figure 5.1: Radiation pattern of the used antenna.

The radiometer exterior and internal deployments are shown in Fig. 5.2 and Fig. 5.6 – the parabolic antenna of the radiometer points vertically through a planar metal mirror tilted under angle of  $45^\circ$ .

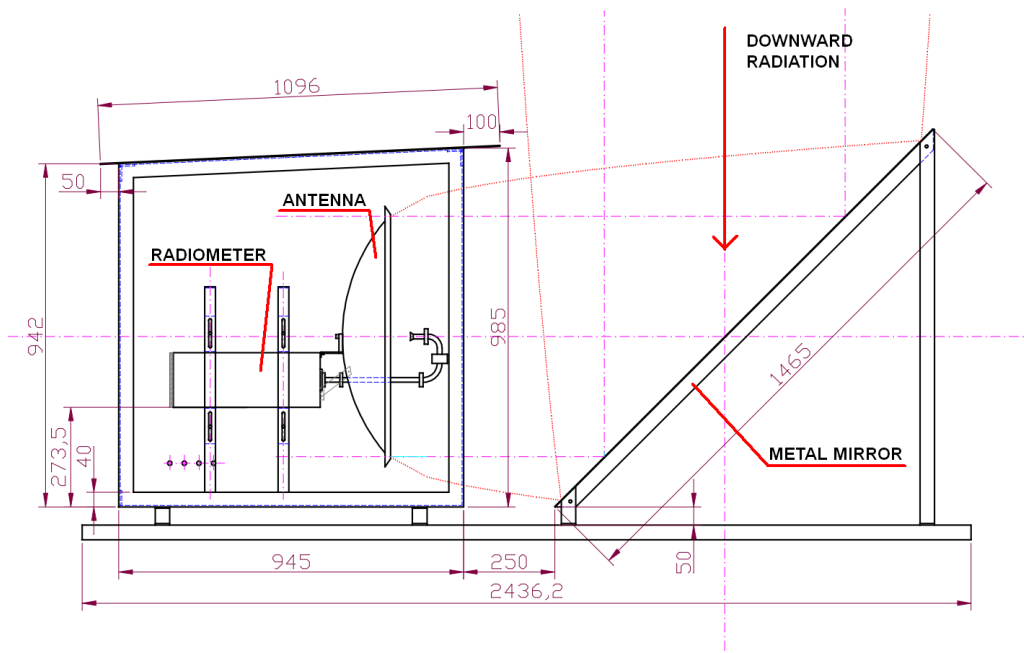


Figure 5.2: Radiometer deployment: Schematic view and dimensions.

This arrangement was chosen in order to avoid antenna aperture deformation by any obstacles (like snow, rain water) on the upper cover that could affect precision of measurement. The metal surface of the mirror was also smeared with a hydrophobic film of silicon oil in order to trickle water drops away. The chosen arrangement allows to measure brightness temperature of the ice and liquid content of clouds in the vertical direction. The main radiometric system parameters are listed in table 5.1.

The test of influence of the mirror on the brightness temperature was performed. Two test cases were evaluated – the antenna pointed directly to the zenith and to the mirror. Fig. 5.3 shows an example – the first 14 samples of brightness temperature were measured with the antenna pointed through the mirror, following samples from 15th to 35th measured with the antenna pointed directly to the zenith and the last samples from 36th to 50th where measured when the antenna was pointed through the mirror again.

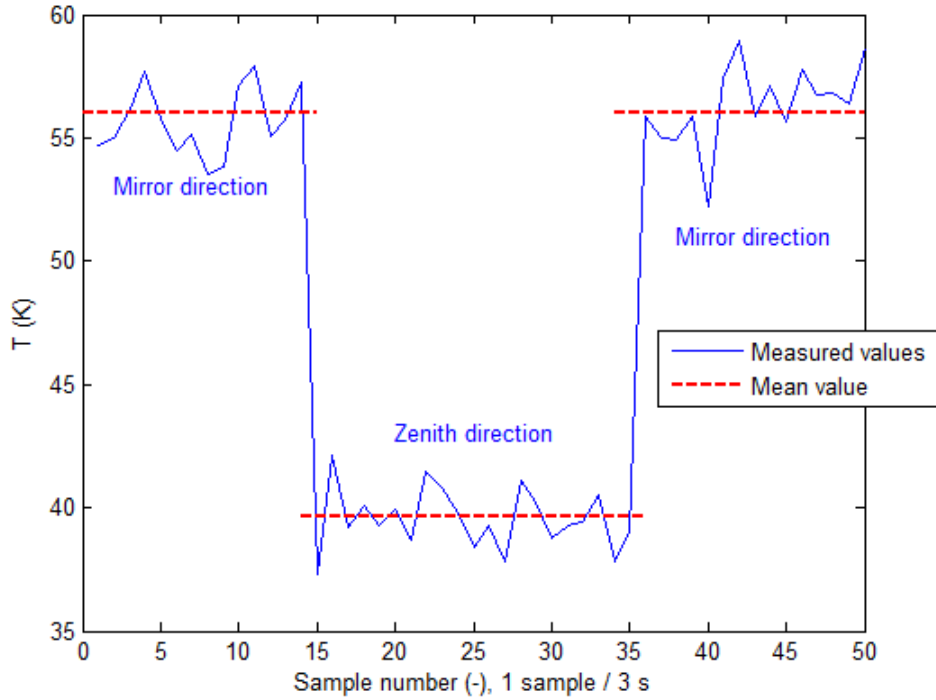


Figure 5.3: Experimental measurement of antenna pointed to mirror, then to zenith and then back to mirror.

Average value of brightness temperature measured in horizontal position through the mirror was 56.1 K, while the brightness temperature measured in the zenith direction was 39.6 K. Variance of the signal for both cases was similar – when pointing to the zenith was 2.29 K<sup>2</sup>, in mirror direction 2.36 K<sup>2</sup>. The difference of the brightness temperature value is caused by antenna side-lobes which receive signal from the surroundings. Setups were tested during various weather conditions (sunny and cloudy day) and it was found that the difference of signal measured in both direction is stable and changes in the order of hours which doesn't affect the dynamic atmospheric effects sensing where the variance method is used. However, the reflectivity of the metal mirror can be calculated. Measured brightness temperature consists of three main contributions:

$$T_B = T_{BA}\rho^2 + T_M(1 - \rho^2) + T_{BSL}, \quad (5.2.1)$$

where brightness temperature  $T_{BA}\rho^2$  which is reflected by the mirror, emission of the metal mirror itself  $T_M(1 - \rho^2)$  and the side lobes contribution  $T_{BSL}$ . Estimation of the brightness temperature received by the side lobes is approximately 280 K but since the side lobes suppression is better than 20 dB, only temperature of 2.8 K can be received.

Then the reflectivity can be determined:

$$\rho = \sqrt{\frac{T_B - T_{BSL} - T_M}{T_{BA} - T_M}} = 0.98 \quad (5.2.2)$$

In order to verify the radiometer bandwidth the experimental measurement setup with radiometer and signal generator was arranged – as is depicted in Fig. 5.4.

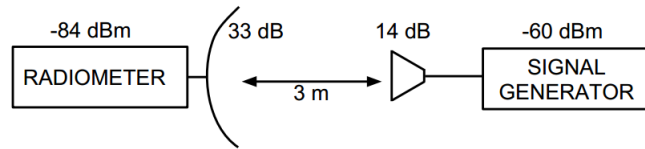


Figure 5.4: Deployment of the radiometer and signal generator in order to measure the radiometer bandwidth.

The power level on the signal generator was set to -60 dBm and the frequency sweep in the band from 10.4 GHz to 12 GHz with the frequency step of 10 MHz. Brightness temperature measured by the radiometer was recorded. From Fig. 5.5 was determined the bandwidth of radiometer 810 MHz.

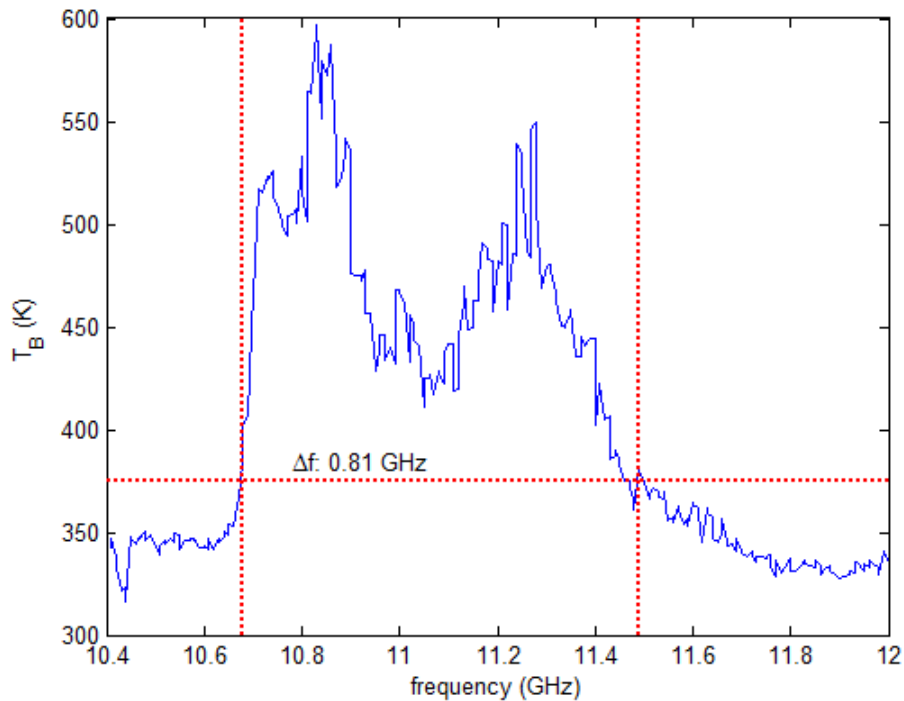


Figure 5.5: Measured brightness temperature during frequency sweep.

With use of the equation (2.2.2) the received power is then approximately -83 dBm. When considering the receiving parabolic antenna with gain of 33 dB, transmitting antenna with gain of 14 dB and 3 m distance of the antennas, the expected value of received power will be -75 dBm which closely corresponds to the received power.

In order to find the radiometer sensitivity the calibration experiment was performed. Radiometer was pointed to the absorbers which were heated from the temperature of 8 °C to the room temperature of 23 °C. During the measurement the signal was recorded. From the width of the noise waveform (tangential sensitivity) was found. Then, the statistical radiometer sensitivity was determined to be 0.7 K.

Table 5.1: Radiometric system parameters.

Parameter	Value
Radiometer bandwidth	0.81 GHz
Integration time	0.5 ms
Radiometer sensitivity	0.7 K
Antenna beamwidth (-3 dB)	4.4 deg
Sidelobe suppression	>20 dB
Measuring data averaging interval	3 s
GPS location	50.10339, 14.392749



Figure 5.6: Picture of the measurement site.

In the Dicke design, the radiometer switches in turn between the antenna output and the reference (temperature stabilized) load.

CTU radiometer has circulator-based waveguide switch. As an example of other switch designed can be demonstrated on the results of the short-term scientific mission of author in 2010 at University of Perugia. During the mission a new MEMS switch for radiometric application was designed – see [39].

The MEMS switch is depicted in Fig. 5.7. The MEMS switch is introduced as possible arrangement which has been realized for another radiometer of research team at University of Perugia. The Details of the MEMS switch are more in detail discussed in [39]. The whole MEMS switch is embedded as the BiCMOS BEOL (Back-end-of-line) MEMS switch [40], [39]. The movable part of bridge is suspended above the RF line and by moving the bridge down, the RF signal is shorted through a capacitive coupling to the ground. The capacitive feature is implemented as a MIM (Metal-Isolation-Metal) capacitor between the RF line and the bridge, between 2nd and 3rd layer of the IHP BiCMOS technology [40]. The bridge is connected to the ground conductors by springs which allow actuating the bridge with lower voltage.

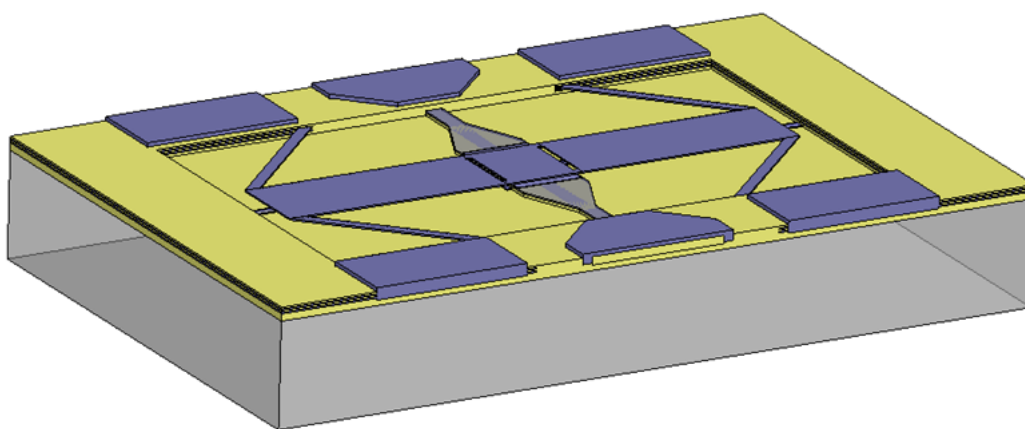


Figure 5.7: State-of-art MEMS switch used for load switching.

After the signal has passed through internal amplifiers and a detector, part of the signal is detected at the switching frequency by a synchronous detector. The output signal of the synchronous detector is proportional to the difference of the brightness temperature of an observed object and the reference load. The used radiometer principle introduces a higher level of stability and sensitivity at the expense of reduced thermal sensitivity. The switching of the gain with calibration was also used to avoid saturation. Temperatures of particular subsystems in the radiometer are measured and used for the continuous correction of measured data. The radiometer has a floating reference whose temperature changes are substantially slower than the changes in measured brightness temperature. The temperature stability of the reference load is given by a robust and thermally insulated construction where the temperature is also measured. The time constant of the reference load is more than ten times higher than the time constant of the measured object. Therefore, there is no need ever to calibrate the equipment after the first laboratory calibration. The use of another type of radiometer such as a total power radiometer or a noise injection radiometer was also considered at the very beginning of the measurement campaign; however the Dicke design was selected as the best compromise, providing good sensitivity and acceptable stability without any follow-up calibration [9]. Some undesirable

signals can affect the measurement, such as heating of the radiometer housing or mirror heating, but these effects were suppressed by temperature corrections of the radiometer and by a proper detection method.

Data from two (primary and backup) meteorological stations WS981, made by the Anemo Corporation, Czech Republic [41], have been used for further analysis. Each station collects the temperature and humidity, as well as atmospheric pressure (barometer TMAG 518N4F with range 800 - 1200 hPa), precipitations (heated tipping-bucket rain gauge with a collecting area of 500 cm<sup>2</sup>, and the rain amount per one tip of 0.1 mm), and the speed and direction of the wind (anemometer AN 955C). The primary meteorological station is located at same place as the radiometer, i.e. 36 m above ground level. Measurement data are collected in 1 minute intervals, therefore to harmonize the sampling of meteorological and radiometer data, the 3 second intervals of radiometer data were averaged over 1 minute. Only measurements of temperature and precipitation were used for direct processing.

### 5.3 Atmospheric Models

In order to understand the atmosphere from the radiometric point of view the physical properties will be described first. Density of the atmosphere decreases with the altitude. Considering the steady conditions the pressure and density can be described by

$$dp(z) = -g\rho_d(z)dz, \quad (5.3.1)$$

where  $g$  is the gravity constant and atmospheric pressure  $p$  is measured vertically in the upward direction from the surface [8, p. 211].

For the ideal gas the relation of the pressure and density is described by

$$\rho_d(z) = MM_0 \frac{p(z)}{kT(z)}, \quad (5.3.2)$$

where  $M$  stands for the molecular weight of the atmosphere ( $M = 28.97$ ),  $M_0$  means the atomic mass unit ( $M_0 = 1.66 \cdot 10^{-27}$  kg),  $k$  is the Boltzmann's constant and  $T$  is the temperature. By combination of both (5.3.1) and (5.3.2) the complex relationship can be expressed by

$$\frac{dp}{p} = -g \frac{MM_0}{kT(z)} dz = -\frac{dz}{H(z)}. \quad (5.3.3)$$

Microwave radiative transfer in the terrestrial atmosphere is determined by chemical composition and water vapor content. Also altitude distribution of meteorological parameters (temperature, humidity, pressure) has significant influence on the microwave atmospheric transfer. In the atmosphere model that will be considered the altitude profiles of temperature  $T(H)$  will be described by a linear function and pressure and humidity models by exponential functions.

The temperature model can be expressed [3, p. 468] by

$$\left. \begin{aligned} T(H) &= T_0 - \gamma H & H < 11km \\ T(H) &= T_{11} & H > 11km \end{aligned} \right\}, \quad (5.3.4)$$

where  $\gamma$  stands for temperature lapse rate  $\gamma = 6.5$  °C/km,  $H$  is the altitude,  $T_0$  is the temperature close to the Earth surface and  $T_{11}$  stands for the atmospheric temperature in the altitude of 11 km.

The pressure  $p$  and humidity  $\rho_W$  model, respectively, can be expressed by

$$p = p_0 \exp(-\delta H) \quad (5.3.5)$$

and

$$\rho_W = \rho_0 \exp\left(\frac{-H}{PWV}\right), \quad (5.3.6)$$

where  $p_0$  and  $\rho_0$  represent atmospheric pressure and absolute humidity at the sea level and  $\delta$  stands for the pressure lapse rate [8, p. 264].

Considering the stratified atmosphere model the brightness temperature of thermal radiation can be expressed in the convectational form [3, p. 468] as

$$T_B(f) = \int_0^\infty \alpha(f, H) T(H) \exp\left[-\int_0^H \alpha(z) dz\right] dH. \quad (5.3.7)$$

In (5.3.7) the  $\alpha(f, H)$  stands for spectral absorptivity of all gaseous components of the atmosphere. These components characteristics depends on frequency and altitude. In this formula no contribution from surface or other over-boundary medium is considered. Usually the mean temperature  $\overline{T_{BA}(f)}$  is introduced. The  $\overline{T_{BA}(f)}$  is quantity corresponding to isothermal atmosphere temperature. Thus the equation (5.3.7) can be expressed by radiobrightness equivalent  $T_B$

$$T_B(f) = \overline{T_{BA}(f)} \int_0^\infty \alpha(H) \exp\left[-\int_0^H \alpha(z) dz\right] dH = \overline{T_{BA}(f)} [1 - \exp(-\alpha_g(f))], \quad (5.3.8)$$

where  $\alpha_g(f)$  is the total absorption of all gaseous components of atmosphere at the given frequency and in the direction of beam propagation. Absorption in the free atmosphere is mainly represented by absorption of oxygen molecules and water vapor.

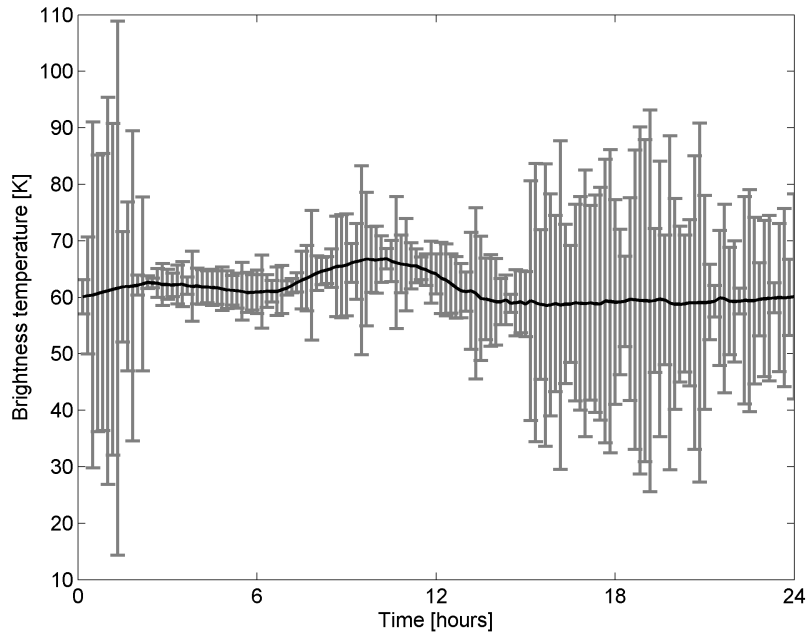


Figure 5.8: Diurnal brightness temperature distribution.

Joint statistics between radiometric data and meteorological data were searched for. In figure 5.8 the diurnal brightness temperature distribution is depicted. For the case of short-term measured statistics (from hour up to daily records) of noise temperature and atmospheric temperature a higher correlation was found (correlation coefficients higher than 0.8). These short-term correlations reached such high values only when relatively stable curves of temperature were measured and simultaneously the noise temperature event was distinct. It was proven that these events are caused by shading of particular clouds. It is easy to understand, when a cloud overshadows the Earth surface, the temperature falls. With the temperature decrease all other atmospheric quantities change similarly. Unfortunately, these mentioned events were rarely distinguished. For majority of time, more complicated atmospheric features were observed.

Contrary to short term statistics, no long-term correlation of measured noise temperature and meteorological data was observed. The noise temperature has no statistically significant long-term relationship either with the atmospheric temperature, relative humidity or pressure. Correlations coefficients from the monthly observation varied in the wide range (from negative linear -0.8 up to positive 0.8), so prediction of precipitations from correlation coefficients between noise temperature and other meteorological parameters was impossible.

Fig. 5.9 depicts the relation between the noise temperature and the received power.

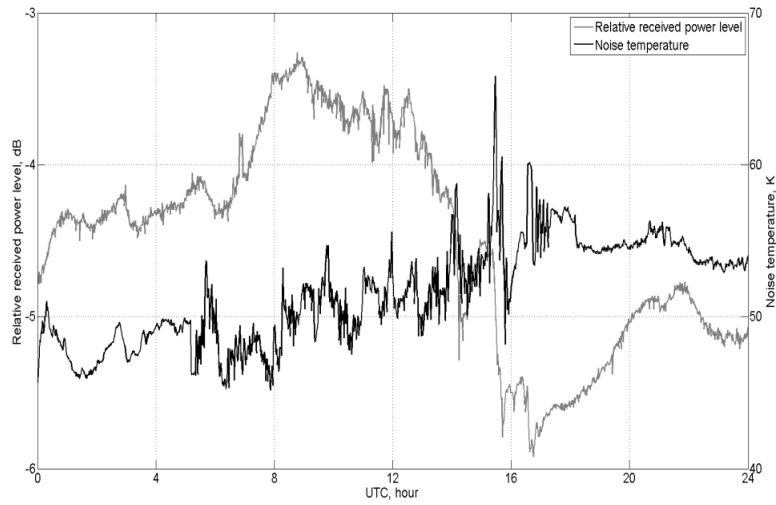


Figure 5.9: Noise temperature swell at the beginning of the rain measured on 29th of March 2010.

If the noise temperature curve is smooth, there can be find sharp fluctuations caused by the rainfall, in which a prediction of oncoming rain is possible and can be properly recognized in 66% of cases. On the other hand, non sharp fluctuations of noise temperature can be used to predict, rain in 43% of cases. Rapid fall of received optical power due to reduced visibility caused by particles scattering is apparent. With the ingoing rainfall the vehement and short rises of the radiometer measured noise temperature were observed. These rises were distinguished mostly at the beginning of the rainfall. The typical brightness temperature swell is depicted in Fig. 5.10.

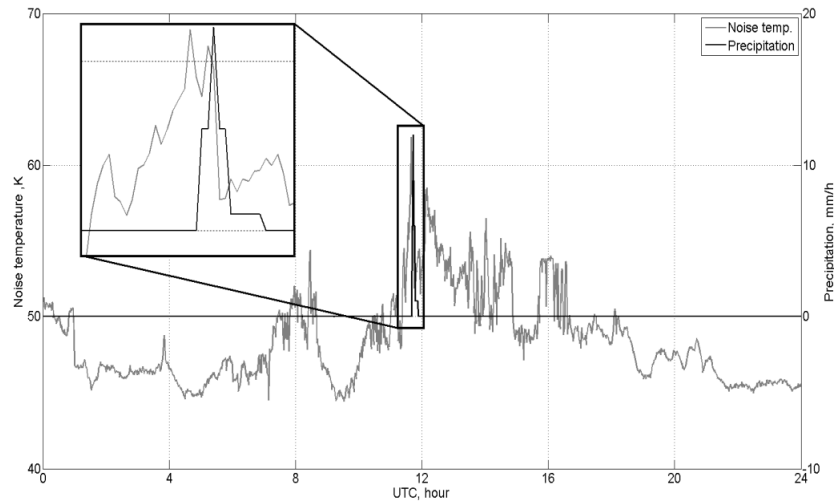


Figure 5.10: Brightness temperature swell at the beginning of the rain measured on 28th of March 2010.

Apart from statistics of meteorological parameters and brightness temperature the combined characteristics of microwave radiometer and free-space optical link were measured.

Since it was determined that the rapid increase of noise temperature indicates a higher probability of a precipitation, the correlation between the noise temperature and received power of the FSO link was evaluated in next step.

In the measuring period every precipitation started with a noise temperature swell. Noise temperature increased to 150% of the original value in 59% of cases and to 125% of the original value in 82% of cases. All increases correlated to FSO fades were perceptible in average 5.3 minutes before the precipitations start. At this time the devaporation starts and the volume of water drops in the observed area strongly increases. After the burst of rain-fall the changes in the noise temperature vanished and the rain could not be detected by the radiometer even if the rain continued. Detectable transients of measured noise temperature disappeared after the beginning of rain as well. Based on measured statistics our next research is focused to derivation of FSO fade forecasting model capable to on-line precede drops of optical backbone networks.

## 5.4 Atmospheric Events

During the measuring campaign hundreds of various meteorological events were measured. In this chapter the record of brightness temperature of three various days is depicted. Typical rain events and brightness temperature swells can be seen. In Figure 5.11 is the one-day time series of measured brightness temperature on 10th May 2010 with relation to atmosphere temperature, humidity, precipitation and pressure. The average day temperature was 12 °C. In this Figure the brightness temperature swell can be seen just before the rain starts at 5am, 6pm and 11pm.

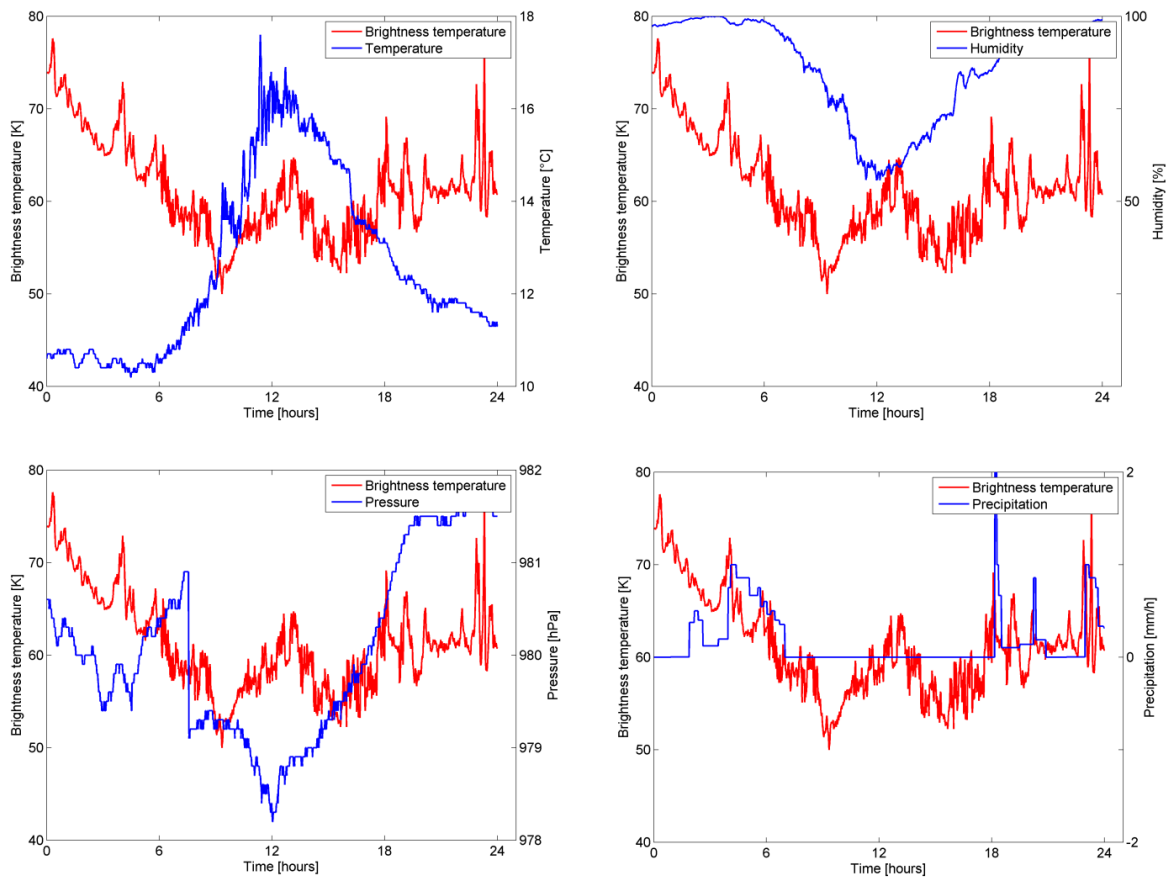


Figure 5.11: Example of measured brightness temperature and meteorological parameters.

In the next Figure 5.12 the measurement from 9th October 2010 is depicted. The average temperature during the day was 16 °C. In this Figure the initial brightness temperature swells can be observed as well.

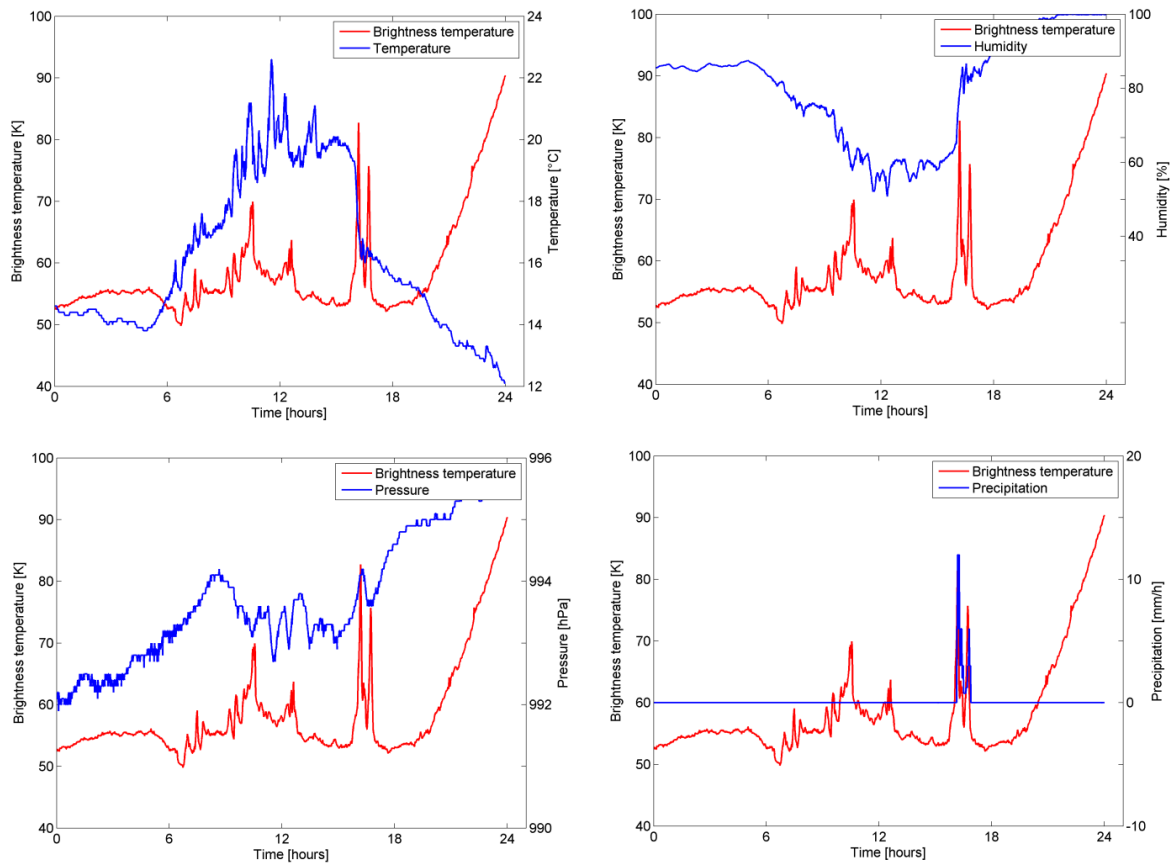


Figure 5.12: Example of measured brightness temperature and meteorological parameters.

In Figure 5.13 the measurement from 17th March 2011 is depicted. The average day temperature was 10 °C. It can be seen in Fig. 5.13 that no significant correlation of brightness temperature and air temperature or any other meteorological parameter can be found. But the brightness temperature swell before the rain can be seen.

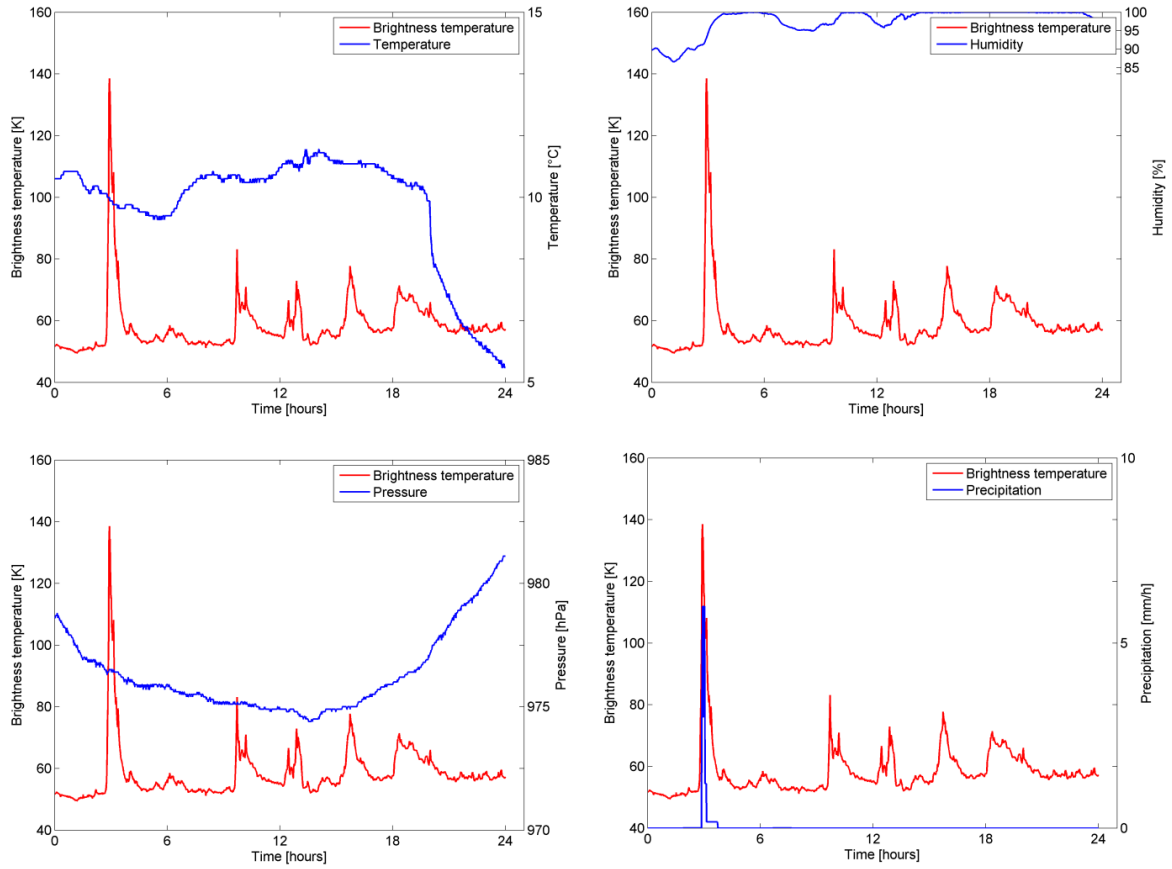


Figure 5.13: Example of measured brightness temperature and meteorological parameters.

## 5.5 Method for Precipitation Prediction

In this section, the relation between measured brightness temperature and weather conditions will be discussed. Nevertheless, the terminology of the detection methods first has to be defined. Hereafter, "Hit" indicates that the precipitation was observed after it had been predicted; "Miss" then means that the precipitation was observed even though it had not been predicted. "False alarm" stands for a situation when precipitation had been predicted but did not occur (see Table 5.2).

Measured data were analyzed over the period of 14 months, from March 2010 to April 2011. During this period 314 clearly defined atmospheric states were observed. These states can be detected or predicted by a microwave radiometer with the use of the proper statistical tools. To achieve the best results the method with variance enumeration was proposed.

The main aim of the paper is to introduce the detection of dynamic atmospheric events that are connected with certain atmospheric states. Initially, the utilization of a microwave radiometer as a precipitation detector and especially for precipitation prediction was in-

Table 5.2: Terminology contingency table.

Event Forecast		
Yes		No
Event Observation		Event Observation
Yes	No	Yes
<b>Hit</b>	<b>False Alarm</b>	<b>Miss</b>

investigated. Different types of clouds as well as various precipitation events were observed and recorded during the measuring period. It was derived similarly as it was described by Won in [30] - that during a particular time interval before the start of a rain event a rapid increase of the brightness temperature can be observed. Contrary to [30], where only small number of events was analyzed, 69 rain events were recorded over the entire period during the 10 GHz radiometer measuring campaign at the CTU.

A simple approach using a steady threshold to predict rain events [42] was dismissed at the beginning of analysis because it had led to a higher number of "False alarms". In Fig. 5.14 a typical situation is depicted on the set of precipitation and brightness temperature data. In this simple (generally used) steady threshold method of cloud or rain event detection, a particular threshold is first carefully determined. When the brightness temperature exceeds the threshold limit, an event is predicted (Hit indication). The main problem arises with the threshold determination. When a low threshold is chosen to achieve extremely sensitive forecasting (i.e. for radiometer measurements in time intervals shorter than 1 minute), a number of "False alarm" signals are usually generated. By establishing a higher threshold we can on the one hand rapidly reduce the number of false alarms, but on the other hand, as it was confirmed by our analyses, this causes more "Misses" and, what is more, it inconveniently shortens the forecasting period before events. In other words, in many cases it results in the degradation of forecasting information. An example of false alarm signals observed on 24th May 2010 before 12.00 (note: all measurement records are related to UTC) can be distinguished in Fig. 5.14. In this case, the threshold was set to a value of 80 K of brightness temperature.

Since the success rate of the method analyzed above had not proved satisfactory, a more reliable detecting method based on observations that the rapid increase of brightness temperature precedes rain events was proposed. The new method inheres in brightness temperature variances calculated over a particular time window within the measuring period. By parametric study, a 5 minute window of variance calculation was found to be the most effective. The signal variance was calculated by

$$\sigma^2 = \sum_{i=x}^{x+l} (T_{A,i} - E(T_A))^2, \quad (5.5.1)$$

where  $E(T_A)$  is the average (in statistics expected) value of the brightness temperature in the specified window,  $l$  is the length of the window in number of samples. The average brightness temperature can be calculated by

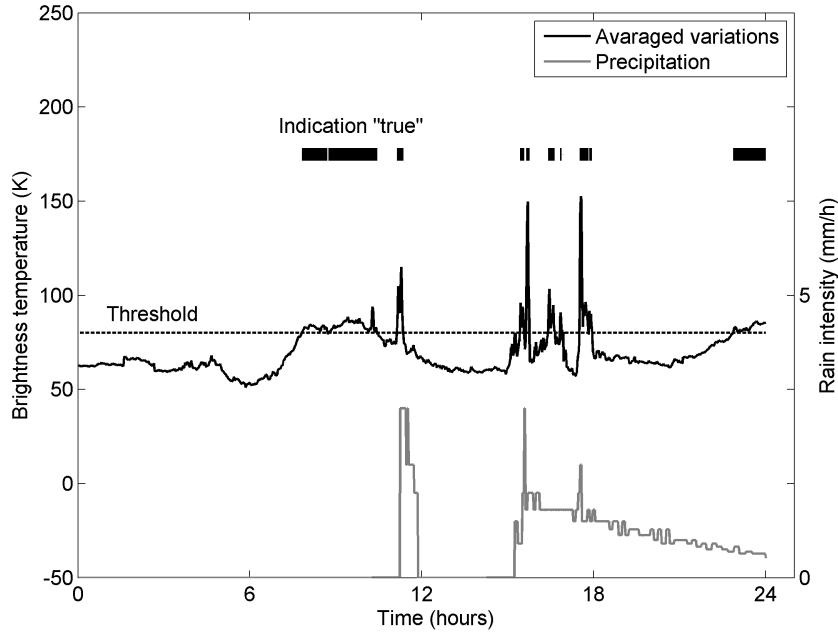


Figure 5.14: Example of simple threshold method utilization for the prediction of rain events; data from 24th of May 2010.

$$E(T_A) = \frac{1}{l} \sum_{i=x}^{x+l} T_{A,i}. \quad (5.5.2)$$

In this case the number  $l$  corresponds to the number of samples which has been taken during the specified time window - 5 minutes.

A shorter window results in higher variances even for non-significant events e.g. an artificial ripple in the brightness temperature, while with a longer window the forecasting information degrades or is lost. To smooth the variance curve, an additional moving average over the 15 minute time window can be applied (note this is not as significant as the first moving average to obtain variances, the 15 minute interval was optimized based on measured data). After these operations the detection threshold can be determined. The advantage of using the variances in this method is in the obvious suppression of slow brightness temperature changes. In this way, variance is also free from the absolute value of measured brightness temperature. The same situation as in Fig. 5.14 is newly demonstrated in Fig. 5.15, where the threshold was applied to the curve obtained by moving-averaged variances. It can clearly be seen that false alarm signals were suppressed, and only real rain events could be detected in advance without a significant number of false signals.

The probability of the successful utilization (hit rate) of the proposed method applied to the whole data set (314 events were considered) is summarized in Tab. 5.3. The whole

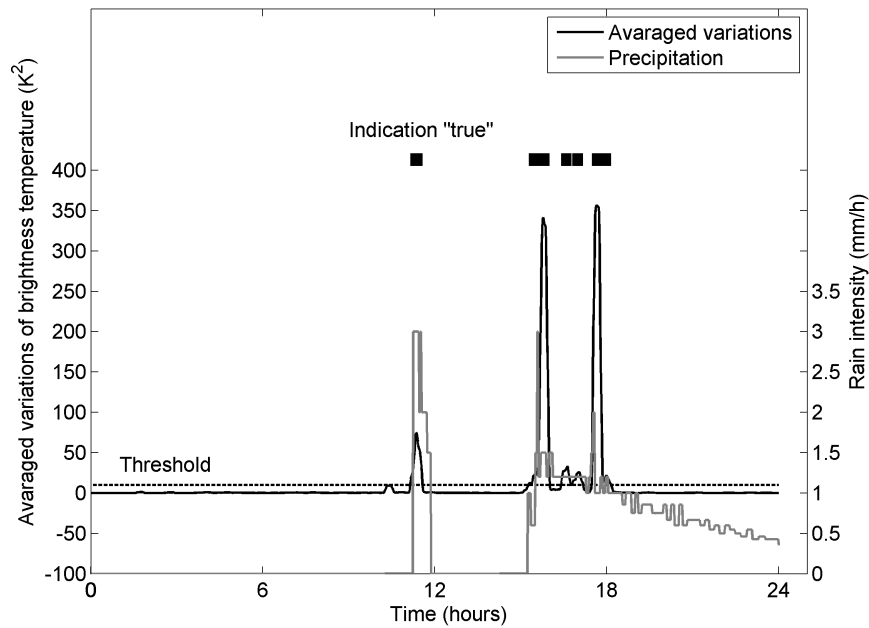


Figure 5.15: Example of undesirable signals suppression and rain prediction by using the method proposed in this contribution; data from 24th May 2010.

range of temperature variations thresholds was scanned and the optimum of 10 K was determined as the value corresponding to the highest and the most stable hit rate over the evaluated period.

To determine the average forecasting time before rain detection at ground level (note this can be for short intervals more precisely expressed as a detection time), a cross-correlation function was used. Every pattern of events was correlated to the function processed for forecasting (variation, averaging) and the correlation was calculated for different time shifts. The maximum of the cross-correlation product and corresponding forecasting time was derived (see Fig. 5.16). The average time of the event forecast before the start of precipitation is 1.8 minutes. Since the variance is calculated over a moving time window of measured data, the result of averaging is delayed to brightness temperature changes. Note that the real peaks of brightness temperature can be observed quite some time before the start of rain (approximately 5 – 10 minutes). The forecasting time of 1.8 minutes represents a compromise value and corresponds to an acceptable number of Hits and False alarms. There is also a certain degree of freedom, and therefore it is possible to choose between a relatively improved forecasting time, but at the cost of a higher number of False alarms or Missed events. The forecasting time is shortened because of the averaging.

Table 5.3: Hit rate of precipitation forecasting by the proposed method.

Threshold	Event Forecast		
	Yes		No
	Event Observation		Event Observation
	Yes	No	Yes
8 K	75,4 %	11,7 %	12,9 %
9 K	75,1 %	11,4 %	13,6 %
10 K	74,4 %	7,7 %	17,9 %
11 K	70,1 %	7,5 %	22,4 %
12 K	59,5 %	7,3 %	33,2 %

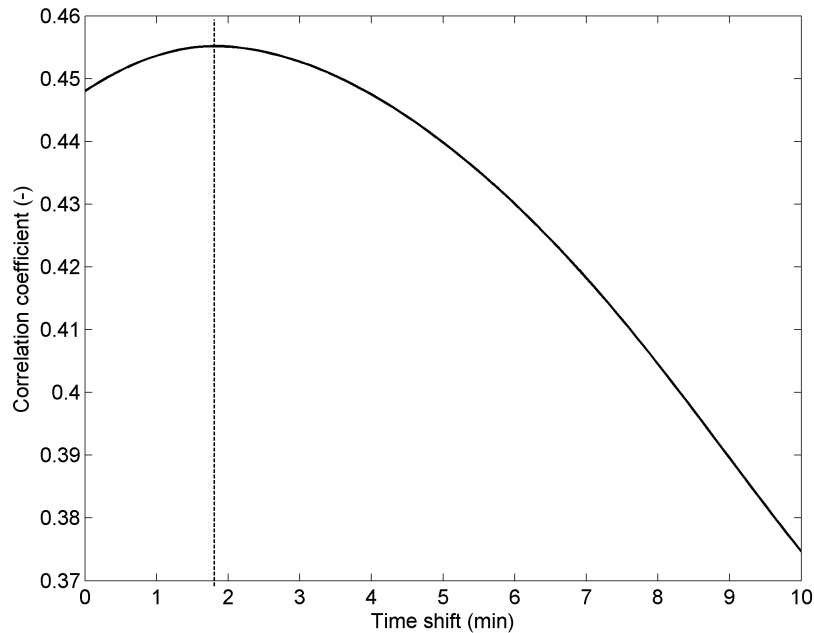


Figure 5.16: Averaged cross-correlation products of all rain events.

## 5.6 Method for Cloud Detection

Next the cloudiness detection method will be described. After eliminating the influence of rain, brightness temperature measured by the microwave radiometer and meteorological data was further analyzed. Despite a high randomness rate in the meteorological data, some particularly interesting relationships were observed. At first, the brightness temperature varied from 47 K up to 65 K, even during periods of clear skies. The amplitude of the measured brightness temperature was dependent on sunshine, i.e. in the daytime. Almost all the higher brightness temperatures with more rapid brightness temperature changes

were related to specific types of cloudiness [43] (for cloudiness types see [44]). These issues were also partially described by Long in [45]. Before any discussion of measured data, it was necessary to clarify how the range of measured brightness temperature conforms to certain types of cloudiness. During the measuring campaign several types of clouds (described below) were observed. The types of clouds were determined periodically by the meteorological station service and their base was measured by a ceilometer. Corresponding brightness temperatures were assigned to cloud types. Cumulus clouds are specific with their clearly defined base formed in low altitudes up to 2.5 km. These clouds have a particularly vertical extent. Cumulus is created by small water drops and can be a source of short-term rainfall. The specific brightness temperature measured in the case of Cumulus clouds varied from 48 K to 55 K. Cumulus clouds can grow into Cumulonimbus - a dense storm cloud with a wide base. This type of cloud is formed at low altitudes from hundreds of meters up to 20 km and can be a significant source of rainfall. The measured brightness temperature of Cumulonimbus clouds was slightly higher than the previous clouds, from 50 K up to 70 K. It was hard to distinguish which brightness temperature is related to Cumulus and Cumulonimbus, but for possible joint microwave links, it is essential that both types of clouds can be a source of rainfall. There is another cloud type with a very low altitude, wide base and small vertical extent the Stratus cloud. The measured brightness temperature of this cloud varied from 50 K up to 80 K. Other types of clouds formed in high altitudes - Altostratus, Altocumulus and Cirrus were omitted from the analyses as they do not cause significant changes in measured temperature because the water content of these clouds is much lower than that of the clouds mentioned above.

For cloudiness detection, a similar technique was used as for precipitation prediction. This method exploits the instability of brightness temperature when a cloud moves through the observed volume. Again, the variance of the brightness temperature was calculated within a 5minute time window over the entire period.

A typical behavior pattern for brightness temperature is depicted in Fig. 5.17, where the clouds presence in the monitored volume of atmosphere from 7.00 to 18.00 caused higher variations of the brightness temperature.

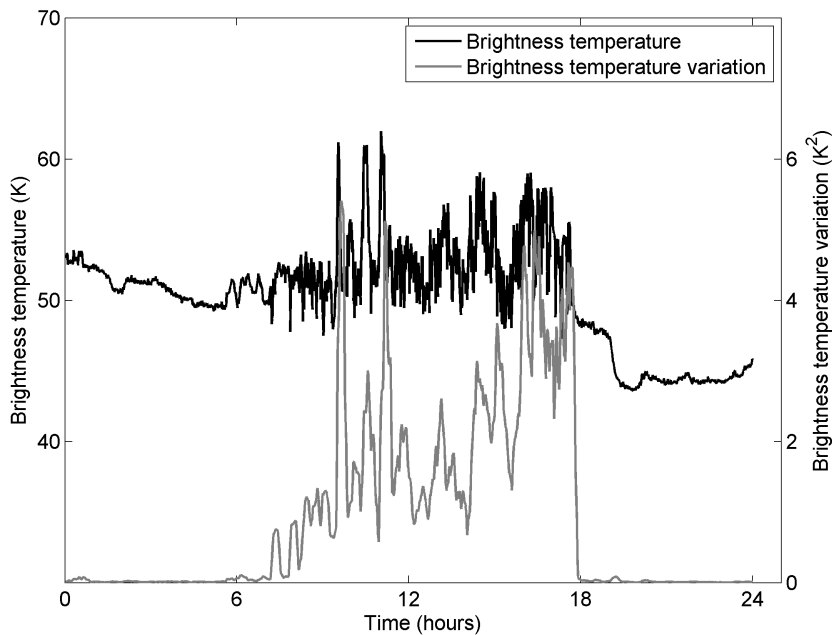


Figure 5.17: Typical variations of the brightness temperature during clouds presence in the monitored volume of atmosphere on 5th April 2010.

Variations of brightness temperature are depicted as a function of ambient temperature in Fig. 5.18 (156 events were captured). The incidence of low temperature can be observed. From the measurements it was found that when the ambient temperature is above 0 °C, the variation of brightness temperature due to the cloud presence is higher - in the range from 0.2 to 4 K. It should be emphasized that when the ambient temperature is below 0 °C, the variation ranges from 0 to 0.5 K. The temperature at ground level (measured by the weather station) is highly correlated to the temperature in the monitored volume of atmosphere above (obtained from the radiometer). Since the radiometer is thermally stabilized, possible slow and minor temperature deviations cannot significantly affect the measurements. To ensure correct interpretation of the results, the influence of temperature (below/above 0) is considered and the results are described for both temperature ranges.

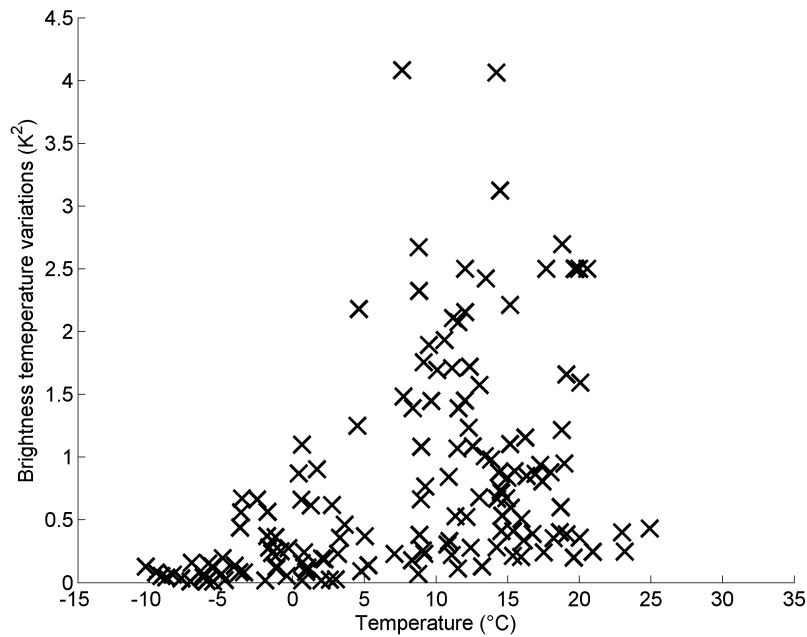


Figure 5.18: Brightness temperature variations when clouds passed through the vertical volume monitored by the radiometer.

In Fig. 5.19, variation of brightness temperature is shown in a cloudless situation in the monitored volume of atmosphere – 158 events were captured during the cloudless period. The contrast with the cloudy case (Fig. 5.18) is obvious. The variation does not exceed the value of 0.25 K during the cloudless period. Variations, based on measurements when clouds were in the observed volume, can be clearly separated from the state when no clouds were present in the observed volume, and hence a method to detect cloudiness based on the calculation of variations can be proposed.

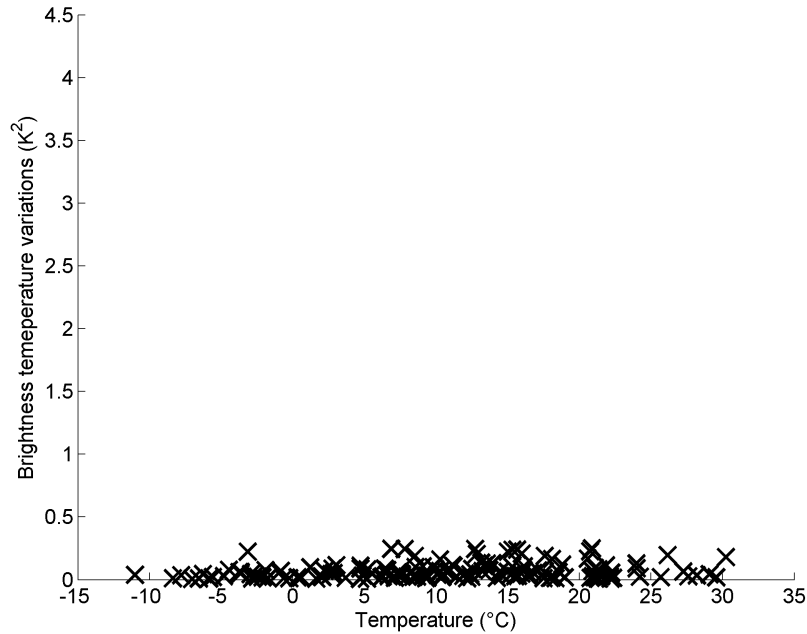


Figure 5.19: Brightness temperature variations when no clouds were present in the monitored volume of atmosphere.

The threshold of brightness temperature variations for the determination of cloud presence was parametrically determined as 0.23 K. Using this value as a decision-making parameter, the following results listed in Tab. 5.4 for temperatures higher than 0 °C were obtained from an analysis of 14 months of measurement data (314 captured events). The hit rate of estimates is substantially higher than the hit rate of estimates calculated for ambient temperatures below 0 °C, when the method cannot be properly applied. In such cases the hit rate was only 31.43 %.

Table 5.4: Hit rate of cloudiness forecasting when the temperature was higher than 0 °C.

		Event forecast	
		Yes	No
Event Observation	Yes	80.5 %	4.8 %
	No	14.7 %	–

## 5.7 Conclusion

In the chapter 5 the atmospheric model for precipitation sensing was proposed. Hundreds of atmospheric dynamical effects were captured and the relation of brightness temperature and meteorological parameters were described. The initial brightness temperature swell

that occurs just before a rain was investigated as the key parameter for all events. Based on this brightness temperature swell a new methodology of rain prediction and cloud detection was proposed and published. The methodology exploits the signal variance as a statistical parameter which steeply grows in advance of a rain event. The parametric study for two parameters was done - the time window over which the variance has to be specified and the threshold as the decision making parameter have been derived from the measured datasets. The precipitation prediction methodology was validated by consequent long-term brightness temperature monitoring. Similar approach was analyzed for cloud detection and was exploited further in section 5.6.

It has to be emphasized, even though several other approaches to predict a precipitation were published, the new proposed methodology brings a general view on the issues and proposes novel but generally applicable method which is easy to integrate to a measuring system.

## 6 Fire Sensing Methodology

Principles of remote sensing of the atmosphere and ground are well described. The fire-endangered environment is typically scanned by several means (radiometer, camera, IR camera) using different frequency bands. Basic fire observation in the visible light spectrum (450-750 nm) is the most inherent for human beings but this has many limitations as only the visible part of fire can be seen, and in most cases, only direct flames can be seen and detected. Such observations can be useless when obstacles that shadows an area of interest, or, when a fire is in its smoldering phase and has no apparent fire signs. The last argument can be eliminated by using thermal scanning (1400nm) but problems with obstacles still remains. Since the microwave radiation can pass some of natural obstacles (vegetation) it is a reasonable choice to use microwave band as a next means for scanning.

A lot of research teams use either self-developed or commercial radiometers for atmosphere profiling [28,46]. General ground scanning is the basic task of passive remote sensing so it is also described well. The weak point in passive remote sensing is detection and localization of wild fires. Considering the number of wild forest fires over the whole world this part of radiometry application is, with few exceptions, unkempt. To the author knowledge only Italian research teams systematically try to solve fire sensing tasks [36], [32].

### 6.1 Theoretical Introduction and Analysis of Fire Sensing

Since fire remote sensing is, by necessity, a down-looking application several effects must be taken into account. The ground surface is not an ideal environment in terms of microwaves propagation. There are many obstacles and inhomogeneities. Fires that should be detected can be easily overlooked in a tangle of vegetation, sand, wet and dry soil, etc. In addition, the emissivity of the sensed surface must be taken into account. Even the sky's reflection has a minor influence on the measurement and cannot be neglected. The derivation is well documented in [35].

A general scenario of spot sensing is depicted in Fig. 6.1. In this case no fire is present in the sensed spot.

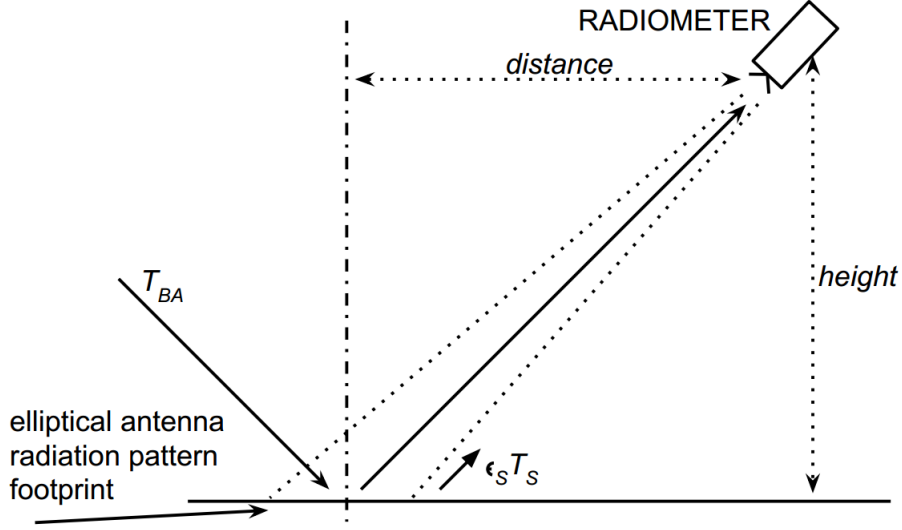


Figure 6.1: General remote sensing deployment focused on a ground target

The antenna is placed in a particular height. In this case the sensed temperature consists of two parts - the soil radiation and the reflected sky radiation. The part of brightness temperature that comes from soil is weighted by the soil emissivity. Likewise, the downward radiation is weighted by the ground reflectivity:

$$T_A = T_S \epsilon_S + (1 - \epsilon_S)(T_{BA} + T_C e^{-\tau_{v,\infty}}), \quad (6.1.1)$$

where  $T_S$  stands for the soil thermodynamical temperature,  $\epsilon_S$  is the emissivity of the soil and the right part of the formula represents downward atmospheric radiation  $T_{BA}$  and cosmic radiation background ( $T_{BC}$ ) weighted by the soil reflectivity  $(1 - \epsilon_S)$ .

### 6.1.1 Soil Emissivity

For early simulations the emissivity described in [47] was used. The emissivity of soil with low vegetation and X-band frequency is in the range from 0.92 to 0.95, it depends on the soil water content and surface roughness.

First experimental measurement was done within the thesis in order to obtain the soil emissivity. For this purpose the thermodynamical temperature of soil was measured as well as the brightness temperature of sensed spot and sky brightness temperature. The soil emissivity can be derived from (3.2.2) as

$$\epsilon_S = \frac{T_A - (T_{BA} + T_C e^{-\tau_{v,\infty}})}{T_S - (T_{BA} + T_C e^{-\tau_{v,\infty}})}. \quad (6.1.2)$$

During the experiment the radiometer antenna was pointed to the sky under the same elevation angle that was then used for fire sensing but in the upward direction. This measured brightness temperature is the  $T_{BA}$  parameter. Then the antenna was turned to the

fire spot (without the fire yet) and the brightness was recorded again. The calculated emissivity during the period of several minutes is depicted in Fig. 6.2 . The measurement should take only a short time in order to avoid weather changes, clouds movements and fast environmental changes that can affect the measurement.

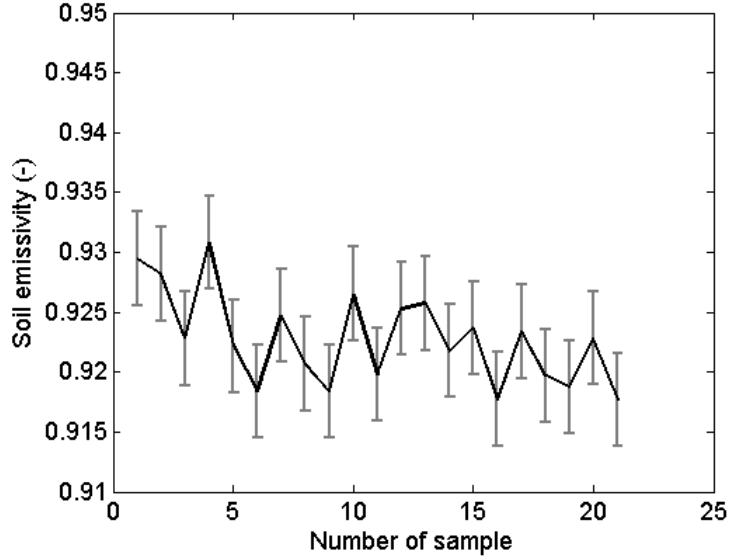


Figure 6.2: Soil emissivity measurement with marked standard deviation.

The experiment was done during cloudy day when the whole sky was covered by consistent altostratus cloud. The brightness temperature measured when pointing to the sky was in the range of 53 K to 55 K, soil thermodynamical temperature was in the range of 20 to 21 °C (293 – 294 K). Brightness temperature recorded by the radiometer was in the range of 273 to 277 K.

### 6.1.2 Filling Factor

For the radiometric measurement in relation with sensing of a bounded spot the filling factor quantity is generally used. It is a representative parameter of spatial resolution of the radiometric system. Usually the filling factor is considered as a fraction of the area covered by the fire which is seen by a radiometer. By using the filling factor the problem with sensing of same fire spot from various distances and under various angles is solved.

Generally the filling factor definition is understood as the power received from a bounded source in relation of the source at the same brightness temperature but filling the whole antenna radiation pattern [48–50].

Formally the filling factor can be calculated by

$$q = \frac{G_0}{4\pi} \iint_{\Omega_F} F_n(\Theta, \varphi) d\Omega, \quad (6.1.3)$$

where  $G_0$  stands for the antenna gain in the direction of maximum radiation,  $F_n$  is the normalized power radiation pattern and  $\Omega_F$  means the spatial angle in which the fire spot is detectable by the antenna.

This equation can be successfully used for environment with more sources of radiation: fire, soil self-radiation, sky reflection etc.

For most cases the simple expression of filling factor can be used

$$q = \frac{A_F}{A_{ant}}, \quad (6.1.4)$$

where  $A_F$  stands for the area of fire and the  $A_{ant}$  is the antenna radiation pattern footprint restricted by the half-power beam-width.

### 6.1.3 Fire Emissivity

In order to supplement general knowledge about the fire sensing, the fire emissivity has to be found. When using approach by [50] the radiometric contrast of a fire spot and bare soil can be defined as

$$\rho_T = (1 - \rho_V)(1 - \rho_A)[\epsilon_F T_F - \epsilon_S T_S - (\epsilon_F - \epsilon_S)\epsilon_V T_V]q, \quad (6.1.5)$$

where  $(1 - \rho_V)$  is the transmissivity of vegetation that can cover the fire spot,  $(1 - \rho_A)$  is the transmissivity of atmosphere,  $\epsilon_F$ ,  $\epsilon_S$ ,  $\epsilon_V$  stands for the fire emissivity, soil and vegetation respectively.  $T_F$ ,  $T_S$  and  $T_V$  are the thermodynamical temperatures of corresponding objects.

Considering that no vegetation was over the fire spot and transmissivity of atmosphere of 1 the relation (6.1.5) can be simplified as

$$\rho_T = (\epsilon_F T_F - \epsilon_S T_S)q \quad (6.1.6)$$

and the fire emissivity can be expressed as

$$\epsilon_F = \frac{\rho_T}{q} + \epsilon_S T_S. \quad (6.1.7)$$

Since the soil emissivity can be measured as well as the soil and fire temperature the fire emissivity is an accessible number. In chapters 6.2.3 – 6.2.6 this relation is used for emissivity calculation. Also all scenarios were numerically simulated in MATLAB where the thermodynamical temperature of all objects, known emissivities and environmental parameters were taken into account. The simulation result is mentioned in following chapters as well.

## 6.2 Fire Detectability

In this chapter the detectability of a fire by a microwave radiometer is investigated. Simulations of several scenarios and together with outdoor measurement were performed in order

to confirm detectability of the fire of specific temperature distributions and dimensions. Various scenarios for fire sensing were numerically modeled and simulated. Real parameters of antenna radiation pattern and radiometer sensitivity were taken into account. The concept of fire detectability verification was tested on real measurement data and then applied in a large scale on analyses of scaled airborne sensing of an environment. The results clearly indicate the possibilities and limits of detection with currently available radiometers.

The brightness temperature was calculated in simulations' stage by

$$T_A = \frac{1}{\Omega_A} \iint_{4\pi} F_N(\Theta, \varphi) T_B(\Theta, \varphi) d\Omega, \quad (6.2.1)$$

where  $T_A$  is the antenna detected noise temperature,  $F_N$  represents the normalized antenna radiation pattern and  $T_B$  stands for the brightness temperature at given azimuth  $\Theta$  and elevation  $\varphi$  angles.

In the following chapters several types of fires were measured in order to obtain the emissivity of various burning matter.

Measurement scenario of fire emissivity was simulated first using the equation (6.1.7) and (6.2.1). The whole scenario was discretized and each element was set to the demanded temperature. Contribution of each element was weighted by the radiation pattern of the antenna that was used for the scanning. Since the absolute temperature of the fire spot was known the only variable in this case is the emissivity which was found by the parametric analysis. That is the simulated value mentioned in following chapters.

### 6.2.1 Airborne Sensing

When the wild fires are monitored it is usually done by remote sensing, mainly in the IR range and, experimentally, in a microwave band. In both cases airborne sensing is frequently used. At the start of our analysis a feasibility study of fire detectability by airborne sensing was done and the entire scenario was numerically simulated then downscaled to dimensions that are possible to measure in a natural environment by the available measuring system, it was measured and the model was verified. The down scaled scenario is described in the following sections.

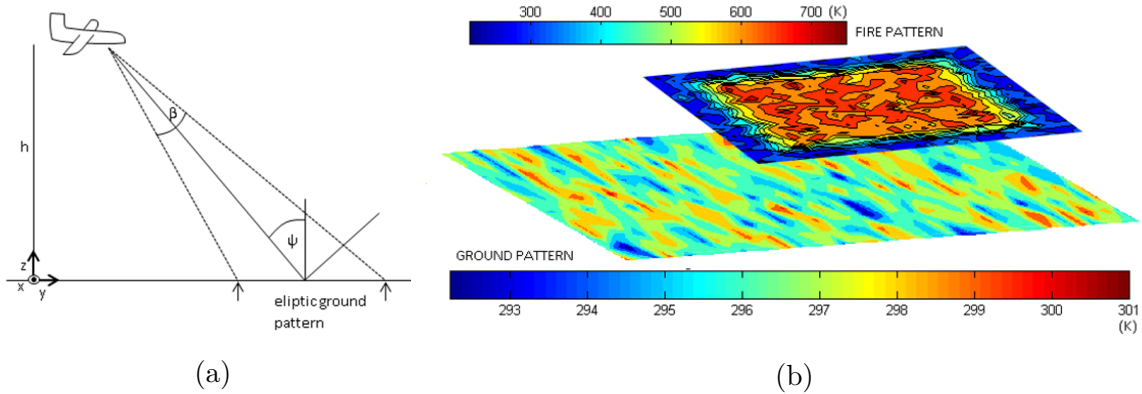


Figure 6.3: Scenarios schemes: a) General schematic view; b) fire and ground temperature pattern (fire pattern is depicted in reduced scale).

Various scenarios have been analyzed. Typical scanning scene is depicted in Fig. 6.3a. Let us assume the ground is being sensed by an airborne radiometer at 300 m above ground level, with an incident angle ( $\psi$ ) up to  $45^\circ$  in the forward direction of the track. In that case, the ground area scanned by antenna beam has an elliptical pattern. For analyses we assumed the ground plane area  $500 \text{ m} \times 2400 \text{ m}$  (width  $\times$  length) with a resolution of 0.5 m/pixel.

A model of a broadside radiating antenna – the 10-element antenna array (typical for microwave remote sensing [8] with  $\lambda/2$  of the antenna elements distance and  $13.4^\circ$  beam width at -3dB) was considered for simulations (see normalized radiation pattern in Fig. 6.4).

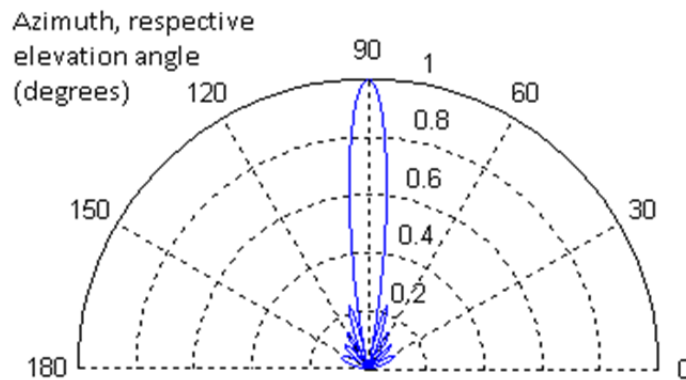


Figure 6.4: Normalized array pattern of 10-element array.

The analyzed fire was located from small scales up to  $2/3$  of the ground plane length. These dimensions were set to cover the ground plane width by the main lobe and the first side lobe of the antenna, especially for better insight on the parasitic influence of side lobes. The ground was considered as homogeneous without any obstacles in the calculated

paths, but with various temperatures in the range of 287 K to 293 K which correspond to a typical natural range of such environment.

Numerical analysis of the above mentioned scenario was performed to define the basic task of airborne sensing. Results from the analysis are shown in Fig. 6.5 .

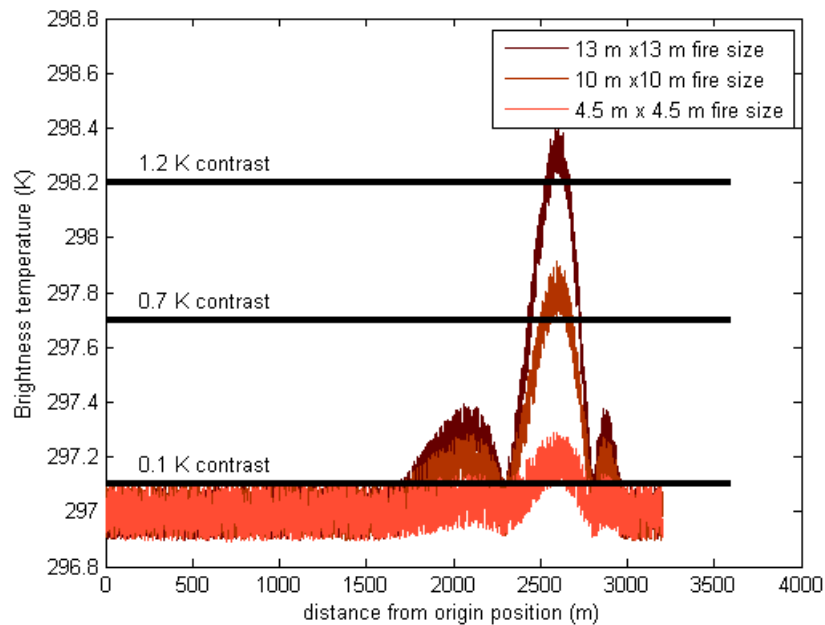


Figure 6.5: Three fires with different size at the temperature in the range of 220 - 290 °C.

The brightness temperature in the simulation was calculated by equation (6.2.1). Several fire types were analyzed. Results in this thesis are demonstrated on an example of the fire TF1 standardized in EN54, Part 9 [51] (burning cellulose wood, size 50 × 50 cm). The first investigated case represents a fire at the moment before direct flame combustion with a cellulosic fire having a temperature in the range of 220 to 290 °C [52]. The next case tested represents the direct-flaming mode where the temperature varies in the range of 300 to 350 °C. Both fire stages were investigated for various fire sizes spread over the scanning area. Distribution of the temperature in the "hot" fire was within the above given range. Both models of fire are considered in the scenario: i) the cellulosic fire immediately after a self-ignition; and ii) the direct, open flame fire. As the fire size varied, the peak-to-peak values of the antenna noise temperature were registered.

Fire in the first smoldering stage having the temperature in the range 220 to 290 °C was assumed [52]. In this analysis 3 radiometers were considered: i) state-of-the-art radiometer [33], ii) commercially available radiometer [53], and iii) radiometer from our laboratory [54]. Main results of the analysis reveal the fire dimensions that are still detectable with the mentioned instruments.

The results from analysis – the limits in microwave radiometer detection of fire – are shown in Table 6.1. Three values of radiometer sensitivity were used to verify detectability

of the fire. The first one is for case of the state of the art radiometer with sensitivity 0.1 K [33], the second one for the commercially available radiometer [9] having sensitivity of 0.7 K and the third one representing the Dicke-type radiometer available in our laboratory with sensitivity of 1.2 K [54]. Each row stands for the minimum detectable fire size corresponding to the particular radiometer sensitivity.

Table 6.1: Detectable fires sizes with respect to radiometer sensitivity.

Dimensions of fire (m × m)	Temperature of fire (°C)	Brightness temperature contrast (K)	Event forecast		
			State-of-art radiometer	Commercial radiometer	Radiometer at CTU lab
4.5 × 4.5	220-290	0.11	YES	NO	NO
10 × 10	220-290	0.72	YES	YES	YES
13 × 13	220-290	1.23	YES	YES	YES
4 × 4	300-350	0.13	YES	NO	NO
9.5 × 9.5	300-350	0.71	YES	YES	YES
11 × 11	300-350	1.35	YES	YES	YES

The example of sensed brightness temperature contrast that is detectable by above mentioned radiometers is shown in Fig. 6.5.

The influence of the fire area brightness temperature distribution was considered as well as various ground plane temperature distribution. Derived results can help hardware designers of radiometric instruments to design a receiver for the purpose of fire sensing with properly set sensitivity with respect to other radiometer potentially adjustable parameters (integration time).

Simulation of the above described scenario was done at first, and then it was verified by the measurement.

### 6.2.2 Human Figure Sensing

The first measurement was performed in order to try to record a human figure in the natural background. The primary intention and request for figure sensing is to perform the detection of a person in case of fire. Since the measurement under real conditions is almost impossible or very dangerous another method was used. The method exploits the difference of emissivity of the natural environment – the soil, grass, vegetation and emissivity of the human body [55, 56].

Deployment of the measurement site is depicted in Figure 6.6. The distance of radiometer and the sensed figure was 10 m. The elevation angle was 58 degrees.

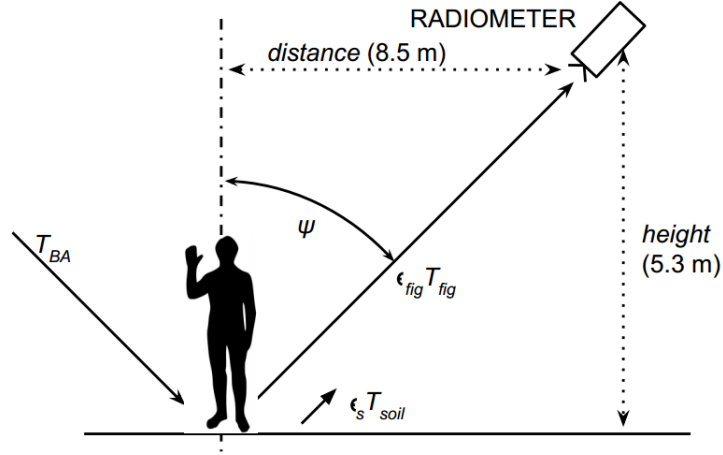


Figure 6.6: Measuring setup and deployment for figure sensing (standing human body).

Human body has significantly different microwave properties than the soil and because of this difference it can be detected and recognized [57], [55], [56]. In this case just the "warmer" spot is sensed and not the human body shape or any geometric characteristics. For this purpose only the brightness temperature from a single elevation was recorded. Measurement was done in the natural environment with dry soil under steady weather conditions. Outside temperature was 31 °C, other measured parameters are listed in Table 6.2.

Table 6.2: Parameters from figure brightness temperature contrast measurement.

Parameter	Value
$T_B$ (soil)	274.9 K
$T_B$ (figure)	273.8 K
$T_S$	294 K
$T$ (figure)	308 K
$\rho_T$	1.1 K
$\epsilon_H$	0.85
$\epsilon_S$	0.92
$q$	21 %

Where  $T_B$  (figure) is the brightness temperature measured by the radiometer when the human figure was present on the spot,  $T_B$  (soil) is the brightness temperature of the spot without the figure,  $T_S$  stands for the thermodynamical temperature of the soil,  $T$  (figure) is the body temperature (in simulations the average temperature was set to 35 °C),  $\epsilon_H$  means the emissivity of human body,  $\epsilon_S$  emissivity of the soil and  $q$  stands for the filling factor of the current setup.

Two measurements were done to sense a figure, both are depicted in Figure (6.7a) and (6.7b). In both cases the measurement process took 15 minutes.

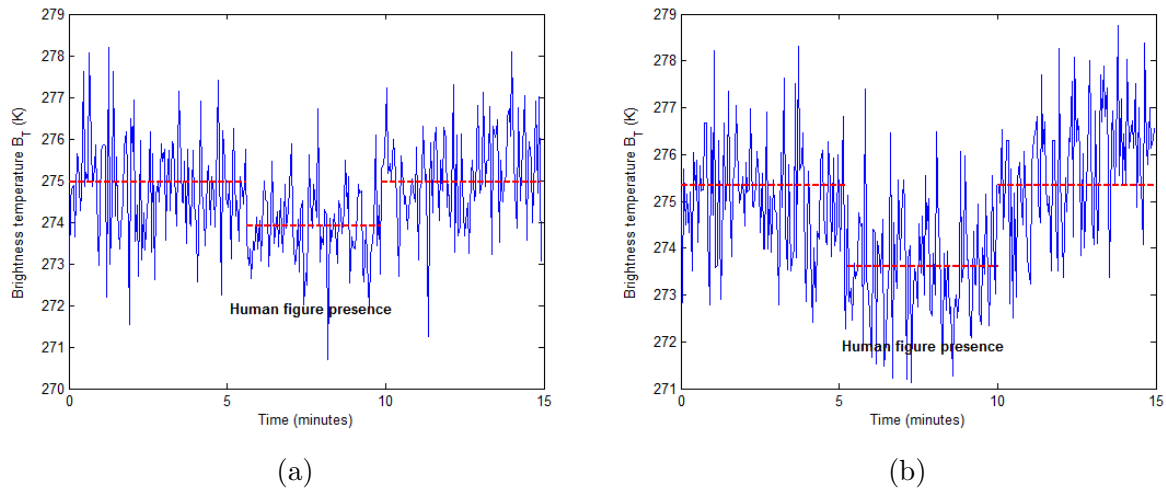


Figure 6.7: Brightness temperature recording when the figure was present on the measured spot: a) The first and b) the second measurement.

There was no figure at the sensed spot in the first 5 minutes. Over the course of the next 5 minutes there was a human figure standing in front of the antenna to have an the approximate body center in the direction of maximum antenna gain. For the last 5 minutes there was now body present at the sensed spot. Before and after each measurement the sky temperature was sensed under the same elevation angle as the figure was sensed. This allowed us to calculate the emissivity of the spot at a later time in accordance with the method described in chapter 6.1.1. In both figures a brightness temperature drop between the 5th and 10th minute is apparent. The average temperature during figure-free time was 275.1 K and during the period with present figure it was 273.4 K. The average brightness temperature contrast is 1.7 K.

The whole task was also analyzed numerically to calculate the emissivity of the spot occupied by the figure. The possibility of such a simulation will be proved in chapter 6.2.7.

For the emissivity calculation the complete scenario without the figure was simulated with all known parameters (thermodynamic temperature of the soil, brightness temperature of the sky, measured brightness temperature of the soil). Then the figure was introduced to the environment. Since the total brightness temperature was measured and the thermodynamic temperature was known, the emissivity can be found to be a parametric study where the temperature of the figure changed until the same temperature in simulation that was measured was achieved.

### 6.2.3 Gasoline Fire

The first fire studied was the gasoline fire. 100 cc of gasoline was absorbed into a cotton fabric. Size of the fabric was  $50 \times 50$  cm. By the fabric it is preserved the fire size, shape and homogeneous gasoline distribution in the sensed area. Time of the whole measurement was approximately 11 minutes. In Figure 6.8 the course of the burning is depicted in series

of 4 pictures.



Figure 6.8: Burning of the gasoline fire in 4-picture time series. Fire size  $50 \times 50$  cm.

In Figure 6.9 the measured brightness temperature in a time series is depicted. The ignition occurred in the 7th minute and the whole combustion took approximately 2 minutes.

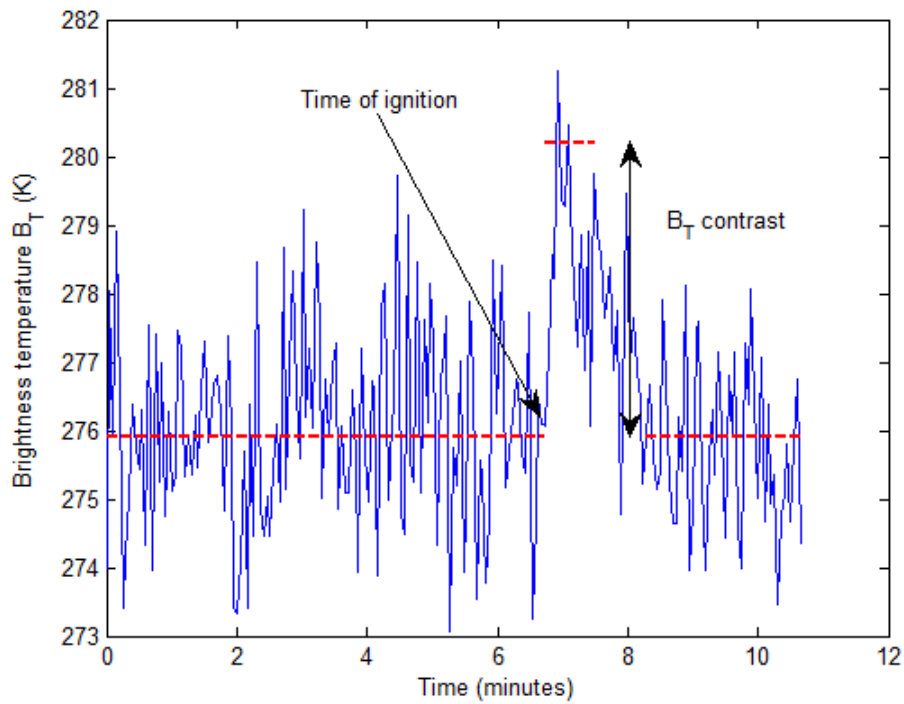


Figure 6.9: Gasoline fire microwave signature. Fire size  $50 \times 50$  cm.

The fire place emissivity, the filling factor and other parameters can be calculated from the known parameters. A list of measured and calculated values is seen in Table 6.3.

Table 6.3: Gasoline fire measured parameters.

Parameter	Value
$T_B$ (soil)	276.1 K
$T_B$ (fire)	280.2 K
$T_S$	294 K
$T_F$	$\sim 1220$ K
$\rho_T$	4.1 K
$\epsilon_F$ (simulation)	0.247
$\epsilon_S$	0.92
$\epsilon_F$ (measurement)	0.248
$q$	13.9 %

Where  $T_B$  (fire) is the averaged maximum brightness temperature measured during the burning process,  $\epsilon_F$  (simulation) stands for the fire emissivity that was numerically simulated and  $\epsilon_F$  (measurement) means the fire emissivity that was calculated from measurement by (6.1.7).

#### 6.2.4 Flood Trash Fire

For the measurement the flood trash fire was chosen. 1kg of the flood trash that consists of dry grass, wood, dust and wooden bark was used. The size of the fire was  $50 \times 50$  cm. The material was evenly spread over the spot. The whole measurement was approximately 13 minutes long, but the burning itself took approximately 5 minutes. In Figure 6.10 the course of the burning is depicted in a series of 4 pictures.



Figure 6.10: Burning of the flood trash fire in 4-picture time series. Fire size  $50 \times 50$  cm.

In Figure 6.11 the measured brightness temperature in a time series is depicted. The ignition occurred in the 5th minute. Since the flood trash was still wet, only the smoldering stage of the fire occurred.

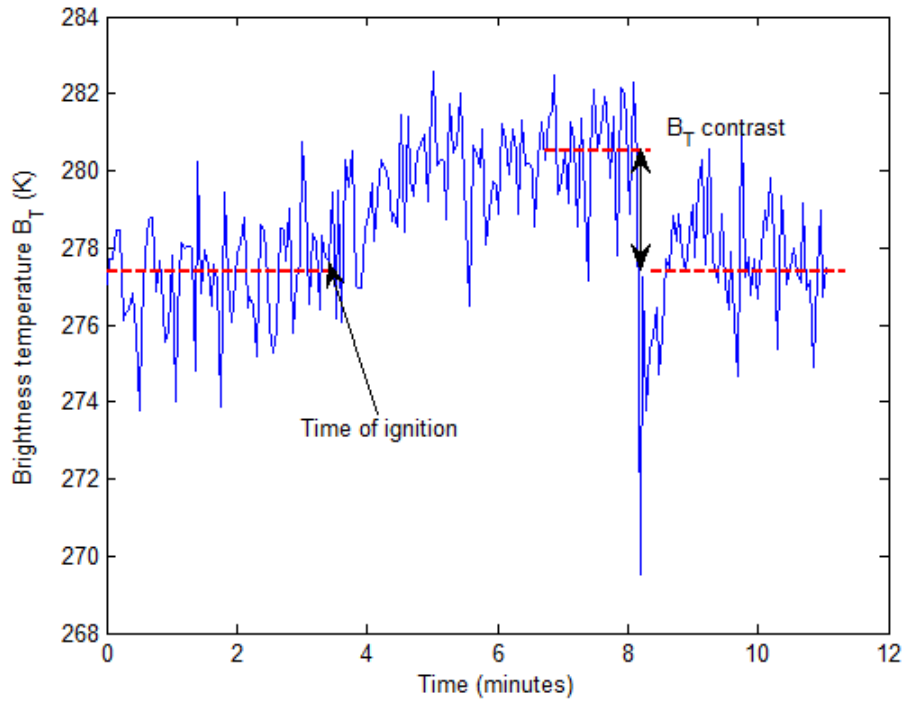


Figure 6.11: Flood trash fire microwave signature. Size  $50 \times 50$  cm.

The signal drop that occurred after 10th minute was caused when removing the rest of smoldering material with a metal tools.

From the known parameters the fire place emissivity, the filling factor and other parameters can be calculated. A list of measured and calculated values is in Table 6.4.

Table 6.4: Flood trash fire measured parameters.

Parameter	Value
$T_B$ (soil)	277 K
$T_B$ (fire)	280.4 K
$T_S$	294 K
$T_F$	$\sim 1150$ K
$\rho_T$	3.4 K
$\epsilon_F$ (simulation)	0.256
$\epsilon_S$	0.93
$\epsilon_F$ (measurement)	0.257
$q$	13.9 %

### 6.2.5 Wood Fire

In Figure 6.12 the measured brightness temperature of a wood cellulosic fire in a time series is depicted.



Figure 6.12: Burning of the wood cellulosic fire in 4-picture time series. Fire size  $50 \times 50$  cm.

The ignition occurred in 4th minute – the first signal drop is apparent and it is caused by a worker who started the fire. Next, the fire was twice checked – the drop in 8th minute and 10th minute, caused again by a worker. These artificial influences were removed from dataset.

From the know parameters fire place emissivity, the filling factor and other parameters can be calculated. List of measured and calculated values is in Table 6.5.

Table 6.5: Wood fire measured parameters.

Parameter	Value
$T_B$ (soil)	277.1 K
$T_B$ (fire)	280.1 K
$T_S$	294 K
$T_F$	$\sim 1200$ K
$\rho_T$	4 K
$\epsilon_F$ (simulation)	0.252
$\epsilon_S$	0.93
$\epsilon_F$ (measurement)	0.257
$q$	13.9 %

In Figure 6.13 the microwave signature of the wood fire is depicted.

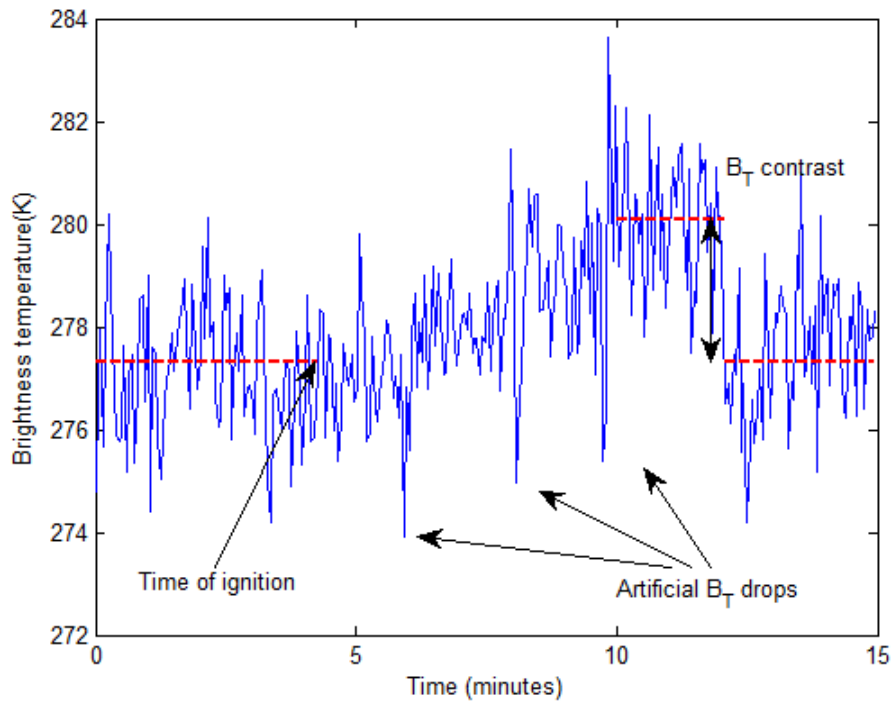


Figure 6.13: Wood fire microwave signature. Fire size  $50 \times 50$  cm.

### 6.2.6 Straw Fire

In order to measure a well burning material with rapid ignition the straw fires were recorded. Those fires were measured with bigger fire spot in order to measure with various filling factor.

The course of the fire in 4-picture time series is depicted in Figure 6.14. For the first fire it was used 400 g of very dry straw spread over the spot of size of  $50 \times 50$  cm.



Figure 6.14: Burning of the straw fire in 4-picture time series. Fire size  $50 \times 50$  cm.

Since the straw burns very rapidly a clear brightness temperature signature was recorded. Maximum brightness temperature was 290.1 K (averaging several top values). Ignition started at 5th minute and the whole burning took approximately 3 minutes.

All measured values and parameters of the first straw fire are listed in Table 6.6. In Figure 6.15 the brightness temperature signature of the straw fire is depicted.

Table 6.6: Straw fire measured parameters. Fire size  $50 \times 50$  cm.

Parameter	Value
$T_B$ (soil)	277.2 K
$T_B$ (fire)	290.1 K
$T_S$	294 K
$T_F$	$\sim 1420$ K
$\rho_T$	12.9 K
$\epsilon_F$ (simulation)	0.254
$\epsilon_S$	0.93
$\epsilon_F$ (measurement)	0.250
$q$	13.9 %

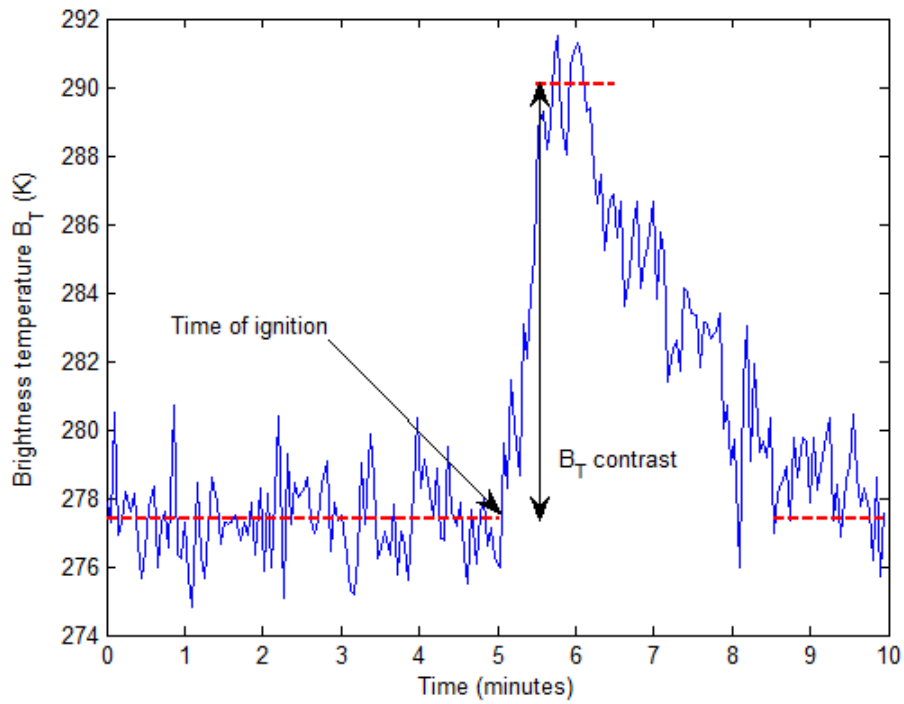


Figure 6.15: Straw fire microwave signature. Fire size  $50 \times 50$  cm.

Next straw fire was smaller, only 300 g of straw was used and the fire spot had size of  $25 \times 25$  cm. Picture of the fire burning are shown in Fig. 6.16.



Figure 6.16: Burning of the straw fire 1 in 4-picture time series. Fire size  $25 \times 25$  cm.

During the fire a minor change of weather occurred (cloud space) but in the brightness temperature signature it can be seen as unsteady signal level. A radiometric contrast was recorded anyway and all parameters of fire were measured.

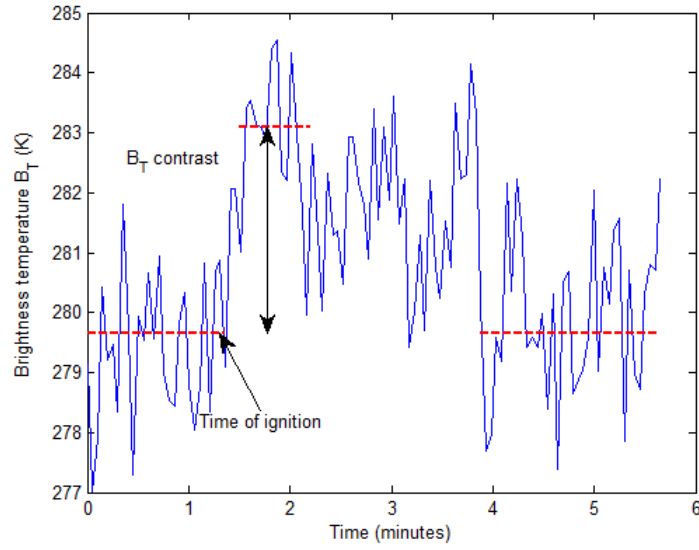


Figure 6.17: Straw fire microwave signature. Fire size  $25 \times 25$  cm.

In Table 6.7 radiometric contrast, calculated and simulated emissivity are listed.

Table 6.7: Straw fire measured parameters. Fire size  $25 \times 25$  cm.

Parameter	Value
$T_B$ (soil)	277.4 K
$T_B$ (fire)	283.1 K
$T_S$	294 K
$T_F$	$\sim 1420$ K
$\rho_T$	5.7 K
$\epsilon_F$ (simulation)	0.298
$\epsilon_S$	0.93
$\epsilon_F$ (measurement)	0.292
$q$	3.8 %

The second small ( $25 \times 25$  cm) straw fire depicted in Fig. 6.18 was recorded in steady weather condition so the signal level is easy-to-read in order to recognize the ignition time approximately at 3rd minute and the burning process took about 2 minutes and 30 seconds.



Figure 6.18: Burning of the straw fire in 4-picture time series. Fire size  $25 \times 25$  cm (the second one).

Maximum value of measured brightness temperature was nearly 284 K which gives more than 7 K of brightness temperature contrast. Recorded signal is depicted in Fig. 6.19

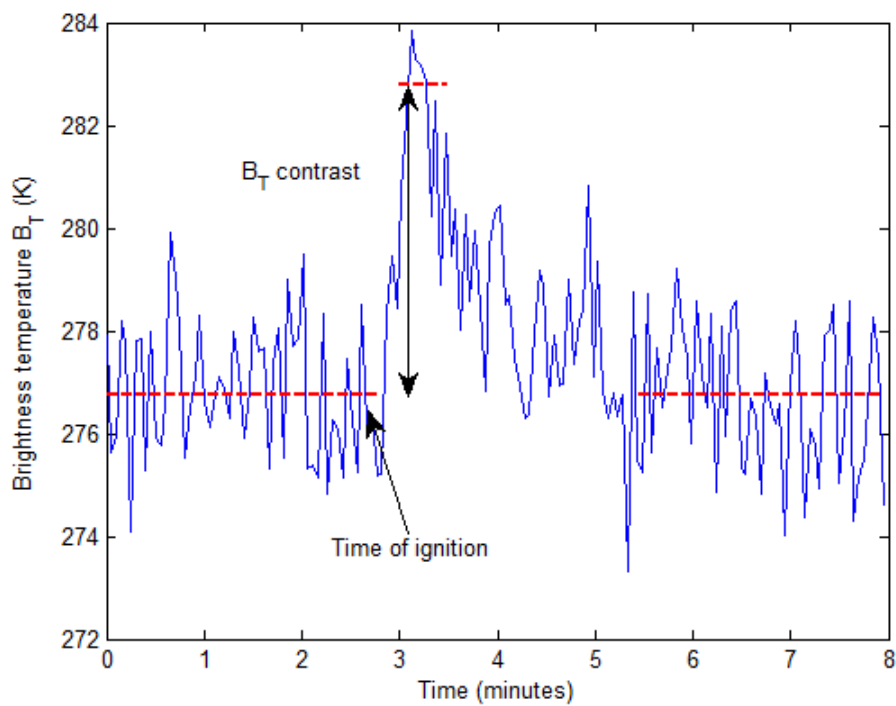


Figure 6.19: Straw fire microwave signature. Fire size  $25 \times 25$  cm.

The most important values and parameters of the measurement are listed in Table 6.8.

Table 6.8: Straw fire measured parameters. Fire size  $25 \times 25$  cm.

Parameter	Value
$T_B$ (soil)	277.2 K
$T_B$ (fire)	282.8 K
$T_S$	294 K
$T_F$	$\sim 1420$ K
$\rho_T$	5.6 K
$\epsilon_F$ (simulation)	0.296
$\epsilon_S$	0.93
$\epsilon_F$ measurement	0.289
$q$	3.8 %

The last straw fire had size of 50 cm in the square shape. More amount of straw was used in order to spread it over the whole spot, approximately 600 g of dry straw was used. In Figure 6.20 the fire spot is depicted during the burning process.



Figure 6.20: Burning of the straw fire in 4-picture time series. Fire size  $60 \times 60$  cm.

Since the last straw fire was the biggest one, also the highest radiometric brightness temperature contrast was recorded and very clear microwave signature of the fire was measured – see the signal in Fig. 6.21.

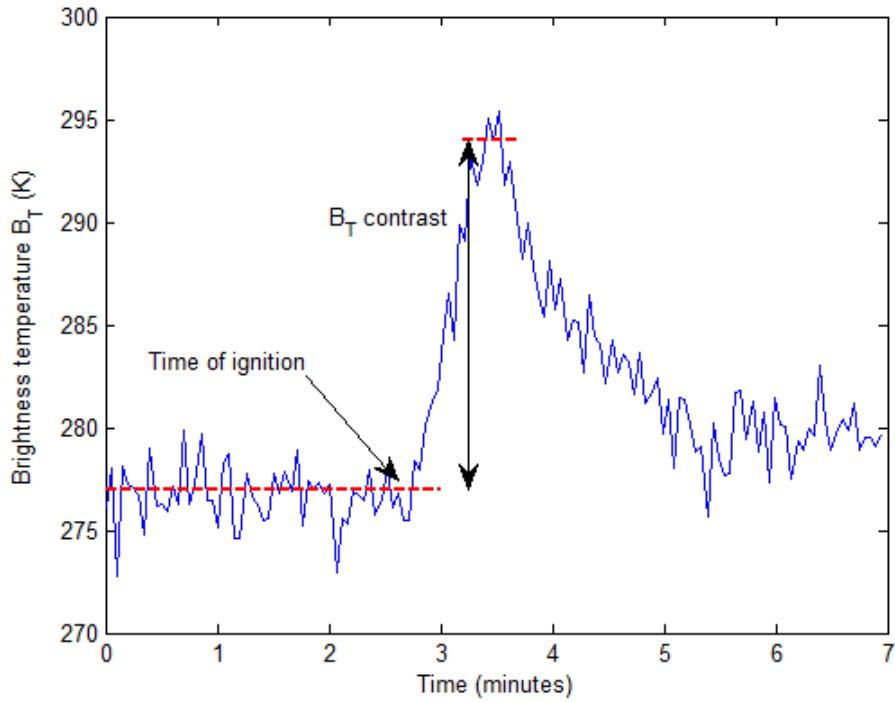


Figure 6.21: Straw fire microwave signature. Fire size  $60 \times 60$  cm.

All important parameters of the straw measurement are listed in Table 6.9.

Table 6.9: Straw fire measured parameters. Fire size  $60 \times 60$  cm.

Parameter	Value
$T_B$ (soil)	277.2 K
$T_B$ (fire)	294.9 K
$T_S$	294 K
$T_F$	$\sim 1420$ K
$\rho_T$	17.7 K
$\epsilon_F$ (simulation)	0.255
$\epsilon_S$	0.93
$\epsilon_F$ (measurement)	0.248
$q$	20.1 %

The possibility of the fire sensing by microwave radiometer has been verified via measurement campaign and several microwave fire signatures were determined. From the recorded and analyzed data the fire emissivity was calculated as a new crucial parameter. It has to be highlighted, to author knowledge this essential parameter has never been

published or derived. The soil emissivity was measured as well in order to derive the radiometric background features beneath the fire. In following chapter the influence of fire size and temperature on radiometric contrast is measured and described to fulfill the methodology.

### 6.2.7 Fire Size and Temperature Influence

For the remote sensing of fire the influence of the fire size on the detectability is necessary to investigate as well as the fire temperature influence. The methodology of fire sensing is based on the different radiometric contrast caused by various fire temperature, size, emissivity of the places that are supposed to be sensed. In the following simulations and measurement both were investigated.

The same radiometric system as is described in chapter 5.2 was used but the deployment of the radiometer and measured spot was different.

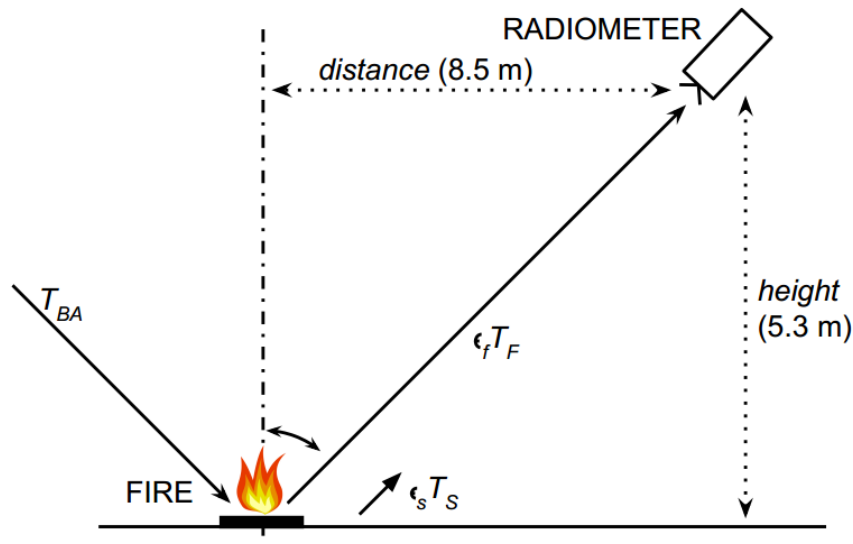


Figure 6.22: Fire measurement deployment.

For comparison purposes, an additional 2D-thermal fire sensing and scanning of surrounding temperature distribution was done by the FLIR i7 infrared camera [58].

A general scenario of simulations and measurement by the radiometer is depicted in Fig. 6.22. Such setup introduces typically used deployment for airborne sensing [8] so it is a good approximation of the up-scaled scenario. During the outdoor measurement the radiometer was placed in the height of 5.3 meters. The incident angle was  $62^\circ$ . Antenna was pointed to the center of fire area. The filling factor [35] in this case was about 15 %.

The same situation was numerically analyzed and the analogical numerical model was designed having resolution of 1 cm. The whole scenario was discretized and contribution of each cell to the total brightness temperature was taken into account. Every cell had a

specific temperature and the antenna radiation pattern was involved in the simulation as well.

Fire size varied from the square area of  $0.3 \text{ m} \times 0.3 \text{ m}$  to  $0.7 \text{ m} \times 0.7 \text{ m}$ . Fire temperature varied in the range of  $500 \text{ }^\circ\text{C}$  to approx.  $1200 \text{ }^\circ\text{C}$  (due to the lower dynamic range of IR camera the upper temperature range was approximated).

Before the start of the first outdoor fire measurement, the brightness temperature background was sensed. The measured ground area had temperature distribution in the range of  $5$  to  $15 \text{ }^\circ\text{C}$ . The soil was dry after a sunny day covered with grass. Figure 6.23 depicts sample of time series of measured and simulated data of brightness temperatures. The conditions of measurement were very steady, the brightness temperature of the background was stable more then 30 minutes.

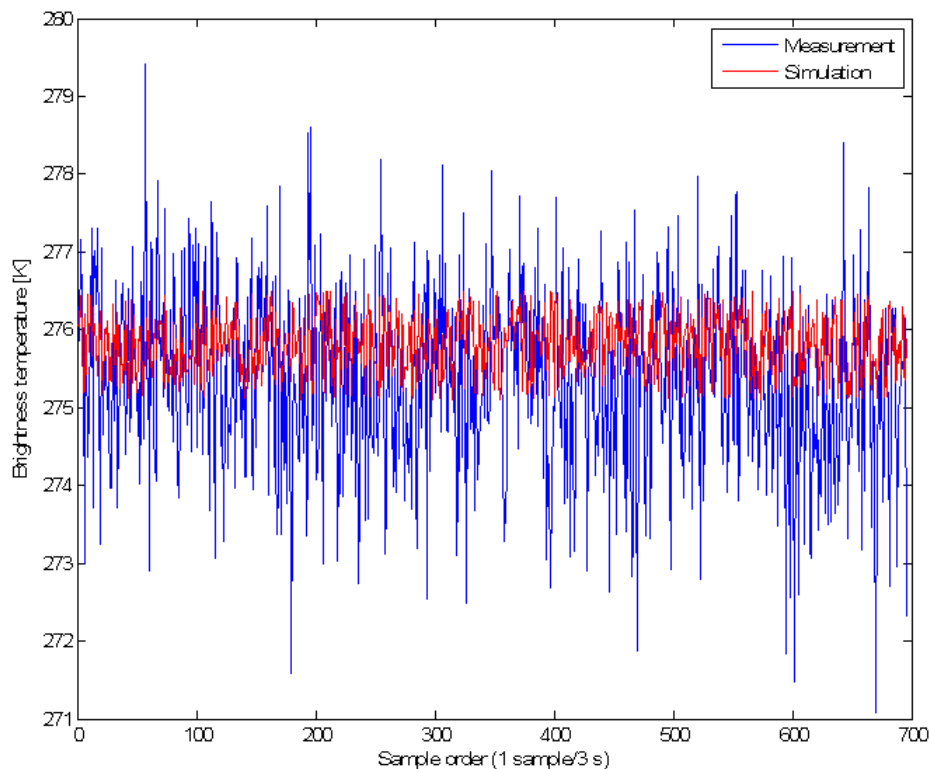


Figure 6.23: Measured background brightness temperature.

For the first scenario a constant fire size was assumed and various temperatures were considered. The fire area had approximately square shape covering the size of  $50 \times 50 \text{ cm}$ . The fire activated from glowing wooden sticks reached highs up to  $2 \text{ m}$  high having bright flames with the temperature approx. up to  $1200 \text{ }^\circ\text{C}$  [51]. Fire development in time as caught by 4 IR shot sequences in 7 minutes is depicted in Figure 6.24 .

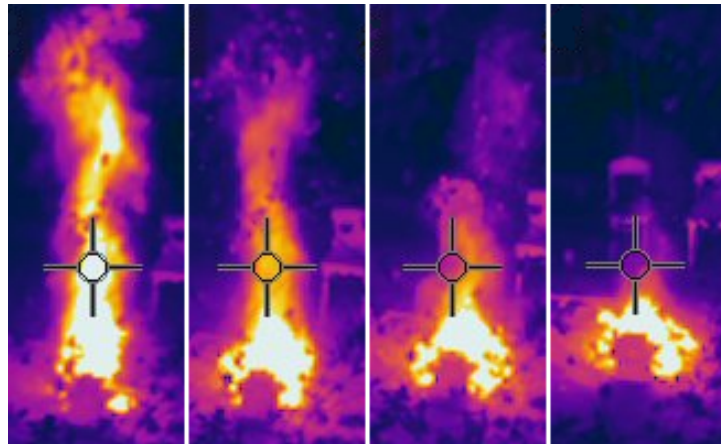


Figure 6.24: Fire development captured by the thermo-camera, temperature range is estimated up to approx. 1200 °C.

Recorded brightness temperature with dependence on fire temperature is in Figure 6.25.

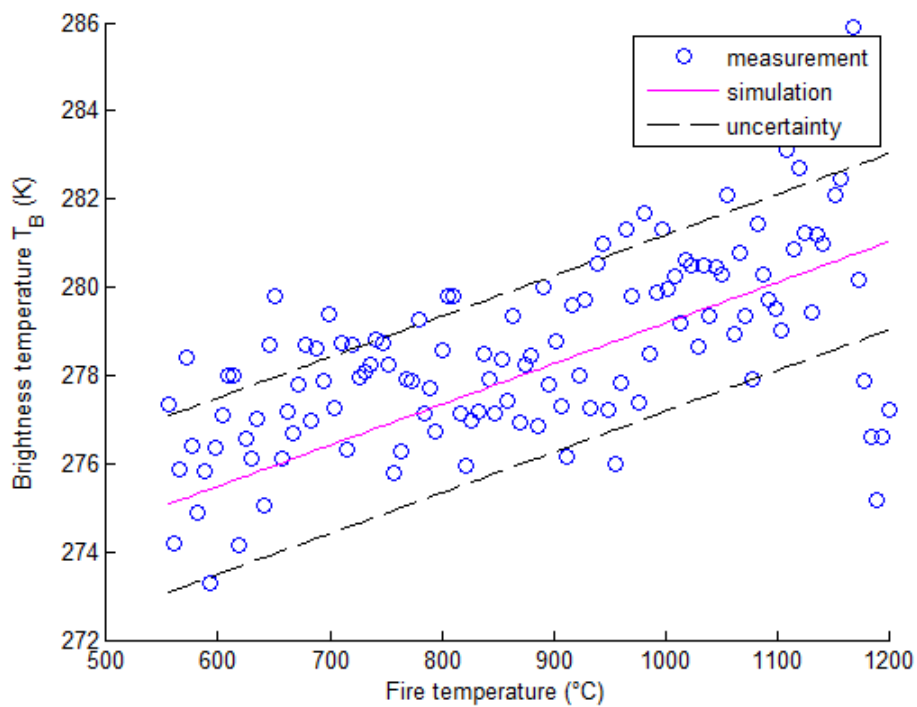


Figure 6.25: Measured brightness temperature as a dependency on fire temperature.

The fire temperature was activated by a compressed air and checked by the IR camera.

Unfortunately, the low dynamical range of the available camera couldn't provide accurate values of the temperature so in later stages the temperature was estimated.

Second measurement was performed to capture brightness temperature as a dependency on fire size. The fire had a square shape varying from the size from  $0.3 \text{ m} \times 0.3 \text{ m}$  to  $0.7 \text{ m} \times 0.7 \text{ m}$ . Temperature of the fire was kept constant and was in the range of  $500$  to  $600 \text{ }^\circ\text{C}$ . For this measurement only glowing charcoals were used in order to easily manipulate with the hot material. Measured values are shown in Figure 6.26.

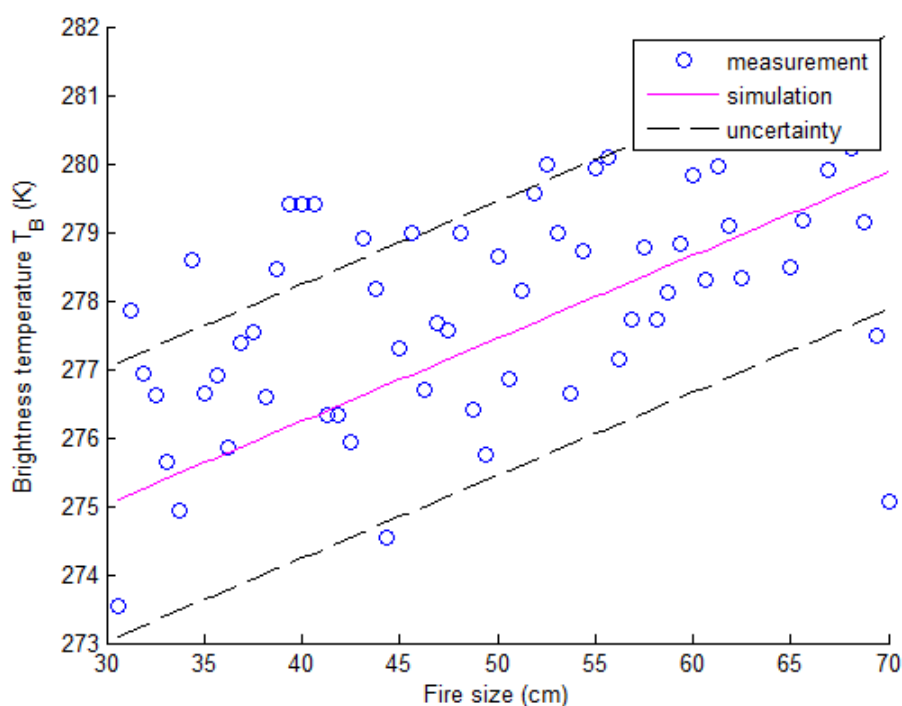


Figure 6.26: Measured brightness temperature as a function of fire size (x-axis describes length of edge of the square fire area).

In this case the resolution of numerical model was set to  $10 \text{ cm}$  per pixel (the smallest fire pixel size was assumed to be  $10 \times 10 \text{ cm}$ ). In the first approach, the model of fire had set constant temperature  $550 \text{ }^\circ\text{C}$  (for distances and deployment see section the picture of deployment above). Results of analysis in terms of the dependency of fire size on brightness temperature contrast are described in Table 6.10.

Table 6.10: Dependency of demanded radiometer sensitivity on the fire size to be detected.

Fire temperature ( $^{\circ}\text{C}$ )	Fire dimensions (cm)	Brightness temperature contrast (K)
550	$10 \times 10$	0.17
550	$20 \times 20$	0.69
550	$50 \times 50$	4.29
550	$100 \times 100$	16.76

Let us assume the ground without a fire has homogeneous temperature distribution. Once the lobe of antenna scans the fire area, the brightness temperature swell is recorded. Table 6.10 then distinguishes which fire size is detectable by specified brightness temperature contrast. For instance the brightness temperature contrast of fire having size of  $10 \times 10$  cm is approximately 0.17 K. So the minimal radiometer sensitivity for detection such fire has to be at least 0.17 K as well. Next simulated scenario was analyzed to obtain the dependence for possibly measured contrasts of brightness temperatures under various fire temperatures. In this case the fire was set constant with size of  $50 \text{ cm} \times 50 \text{ cm}$ . The corresponding results of analysis are depicted in Table 6.11.

Table 6.11: Dependency of demanded radiometer sensitivity on the fire temperature to be detected.

Fire temperature ( $^{\circ}\text{C}$ )	Fire dimensions (cm)	Brightness temperature contrast (K)
550	$50 \times 50$	4.29
600	$50 \times 50$	5.06
800	$50 \times 50$	8.21
1000	$50 \times 50$	11.35

For example for the size of mentioned fire with a temperature  $550 \text{ }^{\circ}\text{C}$  is the brightness temperature contrast approximately 4 K. By the methodology of the fire sensing sensitivity with respect to the fire size it is necessary to involve in measurement a radiometer with the sensitivity of 4 K at least.

### 6.3 Methodology of Fire Sensing

The fire sensing is a complex task and the final measured brightness temperature depends on many effects which should be taken into account. During an on site measurement environmental parameters plays a significant role and must be known as well as the technological constraints of used radiometric system.

In order to sense a possible fire in the field the environmental parameters should be known. As the first step of the methodology the soil properties are necessary to consider. From the radiometric remote sensing point of view it is essential to know the soil emissivity or emissivity of any other natural background. How to measure it is described in chapter

6.1.1. The emissivity can vary from 0.8 to 0.95 and it is different for various vegetation types, sand, soil any other material and also depends on humidity etc.

Once the soil emissivity is known the limiting fire parameters must be found. In chapter 6.2.7 a possible scenarios are listed. Fire sizes and its temperature influence on the detectability by a microwave radiometer are described with proposal of the minimal sensitivity which must be met. In Fig. 6.27 the dependency of fire temperature and its emissivity on the detectable radiometric contrast is depicted.

Radiometer sensitivity is the next parameter which is crucial for radiometric sensing of any objects. When this parameter can be chosen (during the instrumentation development) the choice must be based on the sensitivity study described above and in [59].

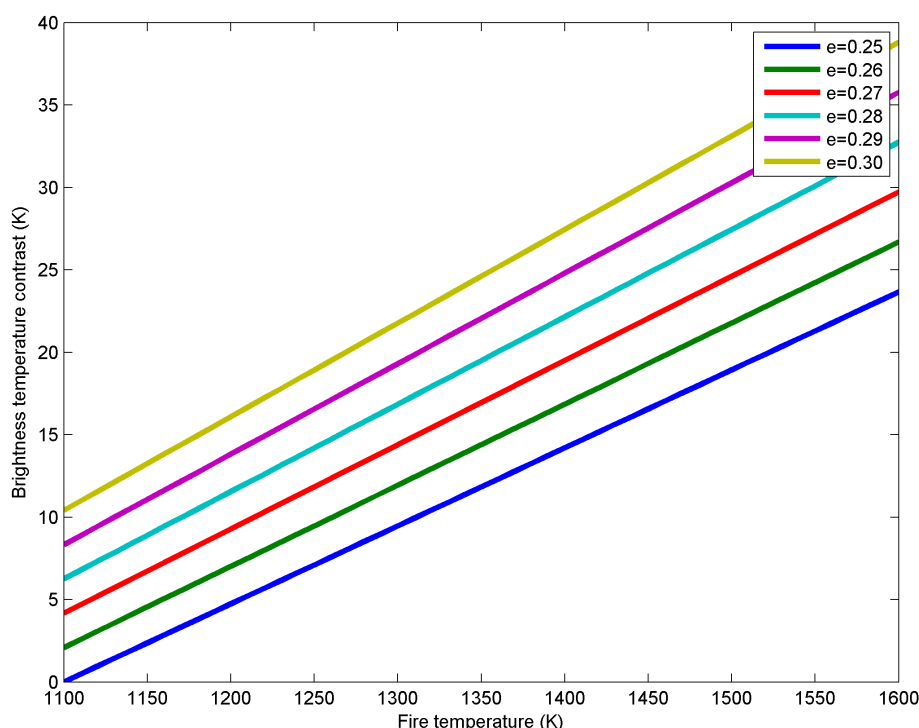


Figure 6.27: Radiometric contrast as a dependence on fire temperature and fire emissivity.

There are several ways for wild fire detection but the airborne sensing is the most convenient way in order to cover an extensive area in a short time. The last parameter is necessary to know and to set: filling factor as is described in chapter 6.1.2. The filling factor has significant influence on the possibility of fire detection. From Figure 6.28 the dependency of filling factor of fire with certain temperature is depicted.

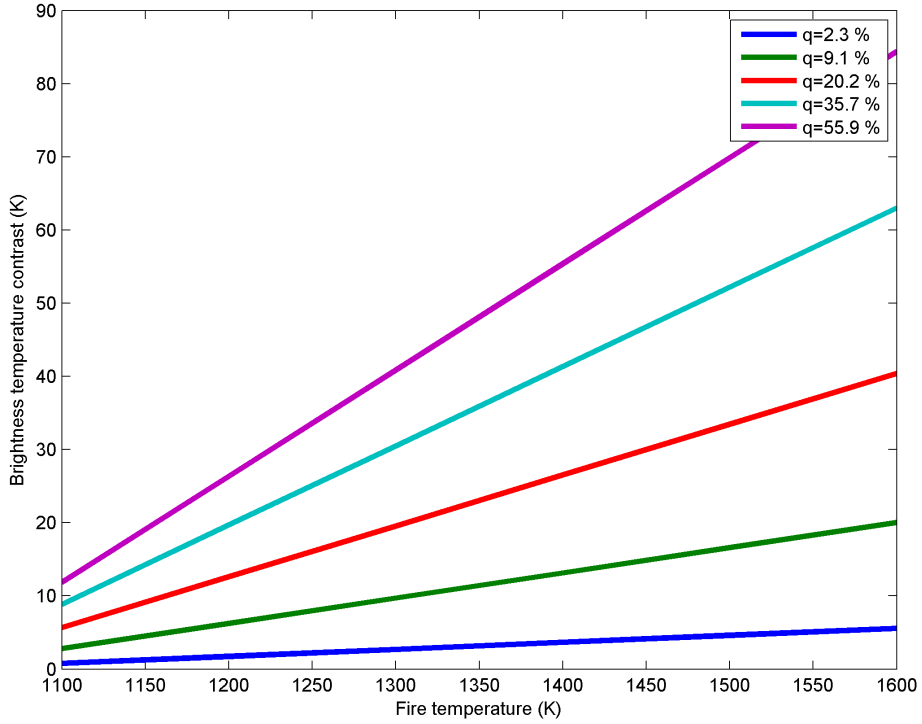


Figure 6.28: Radiometric contrast as a dependence on fire temperature and the filling factor.

When the radiometric system sensitivity is given and the fire temperature is known or expected it is possible to calculate the filling factor in order to plan e.g. altitude of the radiometer position as:

$$q = \frac{\rho_T}{(\epsilon_F T_F - \epsilon_S T_S)} \quad (6.3.1)$$

the  $\rho_T$  stands for the demanded brightness temperature or the radiometer sensitivity respectively.

## 6.4 Conclusion

New methodology of fire sensing was proposed and its parameters were validated based on both measured data and simulation derived results. Typical down-scaled scenario of airborne sensing was simulated and measured. The approaches of fire sensing were investigated. Two cases were measured, fire having different scales either of temperature or being spread on different dimensions. Then, the situation was scaled up and analyzed with the same algorithm for airborne distances and deployment. The main output represents a dependency of brightness temperature contrast on various fire sizes and temperatures. Those

parameters are necessary to be known in order to characterize the fire sensing methodology. The next essential fire parameter is the emissivity. The fire emissivity in the microwave X-band was to the author's knowledge unknown and its parameters have not been published so far. By the series of measurement of several fire types and analyses of the measured data the emissivity was found and incorporated into the methodology as the crucial microwave parameter. Subsequently, the influence of the emissivity on radiometric contrast at a specific temperature was investigated. The influence of the last fundamental parameter – filling factor was explored as well. The dependence of filling factor on brightness temperature contrast of a fire at certain temperature has been determined.

## 7 Conclusion

The thesis was focused on methodologies of remote sensing by the microwave radiometer which allow improving current possibilities of rain prediction, cloud detection and fire sensing.

The first main aim was focused on the new methodology for rain prediction and cloud now-casting using a microwave radiometer. In the datasets, hundreds of atmospheric events was recorded and analyzed in order to propose methodology for rain forecasting. Several approaches were tested and finally the method for detection of the initial brightness temperature swell was derived. For the rain prediction the variance of brightness temperature is calculated over a short time window in order to get a trigger signal on the initial brightness temperature swell before the rain. As the decision making parameter the specific threshold for triggering before rain event was found by the parametric study and set to the threshold 10 K. This value gives the best results with the hit rate of 74.4 % with false alarms in 7.7 % of cases and the miss rate is 17.9 %. The best average forecasting time is 1.8 minutes which was achieved with respect to the low number of false alarms and missed events but expands even up to 10 min before rain (with acceptable hit rate). For the cloud detection the methodology of the brightness temperature variance over a longer time window was proposed and validated by further use of the radiometer. Utilizing the low threshold of 0.23 K in order to detect the cloudiness precise results were achieved and the cloudiness was detected with success rate better the 80 %. The influence of the ambient temperature on the detectability of clouds was investigated as well. Both methods were published in [14].

The second part of the thesis deals with so far not fully mature detection of fires by the microwave radiometer (minimum papers published worldwide). The requirement was to detect the fire by brightness temperature contrast. Since the soil, vegetation, human body and fire have significant difference of microwave emissivity the new methodology was analyzed based on the specific features of this parameter. The soil emissivity was measured in order to capture behavior of the radiometric background beneath the fire. Values in the range from 0.92 to 0.93 were obtained. Several measurements under natural conditions were performed to explore the microwave signatures of various fire types (cellulose, gasoline, straw, trash) and to derive the best possible approach. Value of the fire emissivity has been selected as the new key parameter which has not been investigated yet. The fire emissivity was determined by measurements and simulations to be in the range from 0.25 to 0.30 and this value was incorporated to the methodology. Influence of the fire size and temperature on the recorded brightness temperature contrast respectively was explored. All the results are described in the general form in order to allow choosing the proper radiometer for demanded purpose so the new methodology can be applicable for different equipments and under diverse conditions. Both the state-of-the-art as well as the commercially available instruments have been taken into account in order to ascertain the best achievable results with available instrumentation. Based on the measured data, calculated and derived results the simulations the new methodology of fire sensing was validated.

## References

- [1] Planck Collaboration I. Planck Early Results: I. The Planck mission. *Astronomy and Astrophysics*, 536(A1), June 2011. 16464.
- [2] L. Terenzi, , M. Lapolla, M Laaninen, P. Battaglia, F. Cavaliere, A. De Rosa, N. Hughes, P. Jukkala, V.-H. KilpiA, G. Morgante, M. Tomasi, J. Varis, M Bersanelli, R. C. Butler, F. Ferrari, C. Franceschet, P. Leutenegger, N. Mandolesi, A. Mennella, R. Silvestri, L. Stringhetti, J. Tuovinen, L. Valenziano, and F. Villa. Cryogenic Environment and Performance for Testing the Planck Radiometers. *Journal of Instrumentation*, 4(12), December 2009. DOI 10.1088/1748-0221/4/12/T12015.
- [3] E. A. Sharkov. *Passive Microwave Remote Sensing of the Earth*. Books in geophysical science. Praxis Publishing Ltd., Chichester, UK, 1 edition, December 2009. ISBN 3540439463A.
- [4] Ch. Elachi and Jakob van Zyl. *Introduction to the Physics and Techniques of Remote Sensing*. John Wiley & Sons Inc., Hoboken, New Jersey, USA, May 2006. ISBN 978-0-471-47569-9.
- [5] G. L. Stephens. *Remote Sensing of the Lower Atmosphere: An Introduction*. Oxford University Press, New York, USA, January 1994. ISBN 0195081889.
- [6] N. A. Armand and V. M. Polyakov. *Radio Propagation and Remote Sensing of the Environment*. CRC Press, Boca Raton, Florida, USA, 1. edition, November 2004. ISBN 0415317355.
- [7] P. M. Robitaille. On the Validity of Kirchhoff’s Law of Thermal Emission. *Plasma Science, IEEE Transactions on*, 31(6):1263–1267, December 2003. DOI 10.1109/TPS.2003.820958.
- [8] F. T. Ulaby, R. K. Moore, and A. K. Fung. *Microwave Remote Sensing, Active and Passive*, volume 1 of *Microwave Remote Sensing Fundamentals and Radiometry*. Artech House Inc., Norwood, Massachusetts, USA, March 1981. ISBN 0-89006-190-4.
- [9] G. Evans and C. W. McLeish. *RF Radiometer Handbook*. Artech House Inc., Dedham - Massachusetts, USA, December 1977. ISBN 0-89006-55-X.
- [10] N. Skou and D. Le Vine. *Microwave Radiometer Systems: Design and Analysis*. Artech House Inc., Norwood, Massachusetts, USA, 2 edition, 2006. ISBN 1-58053-974-2.
- [11] M. S. Hersman and G. A. Poe. Sensitivity of the Total Power Radiometer with Periodic Absolute Calibration. *IEEE Transactions on Microwave Theory and Techniques*, 29(1):32–40, January 1981. ISSN 0018-9480.

- [12] J. M. Tarongi, A. Camps, and J. A. Pulido. K-band Radiometer Designed for Academic Purposes: Intercomparison of Performances as Total Power, Dicke or Noise Injection Radiometers. In *IEEE International Geoscience and Remote Sensing Symposium, 2007. IGARSS 2007.*, pages 2927–2930, Barcelona, Spain, July 2007. DOI 10.1109/IGARSS.2007.4423457.
- [13] R. L. Wolf. *Silicon Germanium (SiGe) Bipolar Dicke Radiometer Front End Receiver Chip*. Master theses, University of Massachusetts Amherst, Amherst, Massachusetts, United States, February 2008. [Online; accessed 1-May-2013], Available at <http://scholarworks.umass.edu/theses/76/>.
- [14] A. Colliander, S. Tauriainen, T. I. Auer, J. Kainulainen, J. Uusitalo, M. Toikka, and M. T. Hallikainen. MIRAS Reference Radiometer: a Fully Polarimetric Noise Injection Radiometer. *Geoscience and Remote Sensing, IEEE Transactions on*, 43(5):1135–1143, May 2005. ISSN 0196-2892.
- [15] H. Nakano and Y. Kato. A broadband microwave radiometer using correlation technique. In *Conference on Precision Electromagnetic Measurements Digest, 1998*, pages 596–597, Washington, DC, USA, July 1998. DOI 10.1109/CPEM.1998.700073.
- [16] K. Fujimoto. On the Correlation Radiometer Technique. *IEEE Transactions on Microwave Theory and Techniques*, 12(2):203–212, March 1964. ISSN 0018-9480.
- [17] S. Zvanovec, P. Piksa, M. Mazanek, and Pechac P. A Study of Gas and Rain Propagation Effects at 48 GHz for HAP scenarios. *Journal on Wireless Communications and Networking*, 2008(734216):1–7, April 2008. DOI 10.1155/2008/734216.
- [18] F. Barbaliscia, E. Fionda, and P. G. Masullo. Ground-Based Radiometric Measurements of Atmospheric Brightness Temperature and Water Contents in Italy. *Radio Science*, 33(3):697–706, 1998. DOI 10.1029/97RS02619.
- [19] R. A. Baxter, R. Ware, F. Solheim, D. Patton, J. Oreamuno, G. Fredericks, and P. Wiker. Continuous Thermodynamic Profiling for Air Quality Applications. In *Airnow*, pages 1–4, Raleigh, North Carolina, USA, March 2010. US Environmental Protection Agency, Radiometrics Corporation.
- [20] D. Cimini, Ed R. Westwater, and Gasiewski A. J. Temperature and Humidity Profiling in the Arctic Using Ground-Based Millimeter-Wave Radiometry and 1DVAR. *Transactions on Geoscience and Remote Sensing*, 48(3):1381–1388, March 2010. ISSN 0196-2892.
- [21] J. Gueldner and D. Spankuch. Remote Sensing of the Thermodynamic State of the Atmospheric Boundary Layer by Ground-Based Microwave Radiometry. *Journal of Atmospheric and Oceanic Technology*, 18(6):925–933, June 2001. ISSN 1520-0426.

- [22] L. Li, J. Vivekanandan, C. H. Chan, and Tsang Leung. Microwave Radiometric Technique to Retrieve Vapor, Liquid and Ice. I. Development of a Neural Network-Based Inversion Method. *IEEE Transactions on Geoscience and Remote Sensing*, 35(2):224–236, May 1997. DOI 10.1109/36.563260.
- [23] J. Vivekanandan, L. Li, Tsang Leung, and Chan Chi. Microwave radiometric technique to retrieve vapor, liquid and ice. II. Joint studies of radiometer and radar in winter clouds. *IEEE Transactions on Geoscience and Remote Sensing*, 35(2):237–247, March 1997. DOI 10.1109/36.563261.
- [24] R. Ware, F. Solheim, R. Carpenter, J. Gueldner, J. Liljergen, T. Nehrform, and Vandenberghe F. Radiometric Profiling of Tropospheric Temperature, Humidity and Cloud Liquid. *Radio Science*, 38:1–11, November 2001.
- [25] R. Ware, F. Solheim, and G. Fredericks. Thermodynamic Profiler Temperature Sounding Accuracy. In *Airnow*, pages 1–4, Raleigh, North Carolina, USA, March 2010. US Environmental Protection Agency, Radiometrics Corporation.
- [26] P. W. Chan and C. M. Li. Comparison of Total Cloud Amount Determined by a Ceilometer and a Microwave Radiometer. In *8th International Symposium on Tropospheric Profiling: Integration of Needs, Technologies and Applications*, Delft, The Netherlands, 19-23 October 2009. Royal Netherlands Meteorological Institute; Ministry of Infrastructure and the Environment, Radiometrics Corporation.
- [27] F. S. Marzano and M. Montopoli. Millimeter-wave antenna noise temperature due to rain clouds: Theoretical model and statistical prediction. In *3rd European Conference on Antennas and Propagation, 2009. EuCAP 2009*, pages 2906–2910, Berlin, Germany, March 2009. VDE Verlag GmbH. E-ISBN 978-3-00-024573-2.
- [28] F. S. Marzano, E. Fionda, P. Ciotti, and A. Martellucci. Ground-based Multifrequency Microwave Radiometry for Rainfall Remote Sensing. *IEEE Transactions on Geoscience and Remote Sensing*, 40(4):742–759, April 2002. DOI 10.1109/TGRS.2002.1006317.
- [29] J. Gueldner and D. Spankuch. Results of Year-Round Remotely Sensed Integrated Water Vapor by Ground-Based Microwave Radiometry. *Journal of Applied Meteorology*, 38:981–988, July 1999. ISSN 1520-0450.
- [30] H. Y. Won, Yeon-Hee Kim, and Hee-Sang Lee. An Application of Brightness Temperature Received from a Ground-based Microwave Radiometer to Estimation of Precipitation Occurrences and Rainfall Intensity. *Asia-Pacific Journal of Atmospheric Sciences*, 45(1):55–69, 2009.
- [31] Y. A. Hussin. MODIS - Moderate Resolution Imaging Spectro-Radiometry For Forest Detection. In *NEP-ITC RS/GIS for Monitoring and Assessment of Iraqi Marshland*,

pages 1–27, Enschede, The Netherlands, 6-10 February 2005. United Nations Environment Programme.

- [32] F. Alimenti, T. Kempka, G. Tasselli, S. Bonafoni, P. Basili, L. Roselli, K. Solbach, and H. I. Willms. Fire detection by low-cost microwave radiometric sensors. In *Microwave Radiometry and Remote Sensing of the Environment, 2008. MICRORAD 2008*, pages 1–4, Firenze, Italy, 11-14 March 2008. ISBN 978-1-4244-1986-9.
- [33] F. Alimenti, D. Zito, A. Boni, M. Borgarino, A. Fonte, A. Carboni, S. Leone, M. Piferi, L. Roselli, B. Neri, and R. Menozzi. System-on-chip microwave radiometer for thermal remote sensing and its application to the forest fire detection. In *15th IEEE International Conference on Electronics, Circuits and Systems, 2008. ICECS 2008.*, pages 1265–1268, St. Julien’s, Malta, 31 August - 3 September 2008. ISBN 978-1-4244-2181-7.
- [34] G. Tasselli, F. Alimenti, A. Fonte, D. Zito, L. Roselli, D. De Rossi, A. Lanata, B. Neri, and A. Tognetti. Wearable microwave radiometers for remote fire detection: System-on-Chip (SoC) design and proof of the concept. In *Engineering in Medicine and Biology Society, 2008. EMBS 2008. 30th Annual International Conference of the IEEE*, pages 981–984, Vancouver, BC, Canada, August 2008. DOI 10.1109/IEMBS.2008.4649319.
- [35] G. Tasselli, F. Alimenti, S. Bonafoni, P. Basili, and L. Roselli. Fire Detection by Microwave Radiometric Sensors: Modeling a Scenario in the Presence of Obstacles. *IEEE Transactions on Geoscience and Remote Sensing*, 48(1):314–324, January 2010. DOI 10.1109/TGRS.2009.2024305.
- [36] F. Alimenti, G. Tasselli, S. Bonafoni, D. Zito, and L. Roselli. Inter-Wall Fire Detection by Low-Cost Microwave Radiometric Sensors. In *Microwave Conference, 2008. EuMC 2008. 38th European*, pages 63–66, Amsterdam, The Netherlands, 27-31 October 2008. ISBN 978-2-87487-006-4.
- [37] S. Bonafoni, F. Alimenti, G. Angelucci, and G. Tasselli. Microwave Radiometry Imaging for Forest Fire Detection: A Simulation Study. *Progress in Electromagnetics Research*, 112:77–92, 2011.
- [38] K. N. Liou. *An Introduction to Atmospheric Radiation*, volume 84 of *International Geophysics Series*. Academic Press, San Diego, California, USA, 2 edition, 2002. ISBN 0-12-451451-0.
- [39] P. Dvorak, F. Alimenti, P. Mezannotte, and L Roselli. 31.4GHz BEOL Embedded BiCMOS MEMS Switch. In *Subsystems for Emerging Wireless Technologies (RFCSET)*, Castelldefels, Spain, September 19-20 2011. COST Action IC0803.

- [40] IHP GmbH. SiGe:C BiCMOS Technologies. Technology Overview, IHP GmbH, Frankfurt, Germany, 2013. [Online; accessed 25-June-2013], Available at <http://www.ihp-microelectronics.com/en/services/mpw-prototyping/sigec-bicmos-technologies.htm>.
- [41] Anemo s.r.o. *WS981 (manual)*. Anemo s.r.o., Jana Masaryka 26, Prague, Czech Republic, August 2011. [Online; accessed 11-June-2013], Available at <http://www.anemo.cz/dokumenty/WS981navod.zip>.
- [42] R. R. Ferraro, E. A. Smith, W. Berg, and G. J. Huffman. A Screening Methodology for Passive Microwave Precipitation Retrieval Algorithms. *Journal of the Atmospheric Sciences*, 55(9):1583–1600, May 1998. ISSN 0022-4928.
- [43] G. M. Skofronick-Jackson, A. J. Gasiewski, and J. R. Wang. Influence of microphysical cloud parameterizations on microwave brightness temperatures. *IEEE Transactions on Geoscience and Remote Sensing*, 40(1):187–196, January 2002. DOI 10.1109/36.981360.
- [44] World Meteorological Organization (WMO). *Guide to Meteorological Instruments and Methods of Observation*. Number 8 in Instruments and Methods of Observation Programme (IMOP). World Meteorological Organization, Geneva, Switzerland, 7 edition, 2008. ISBN 978-92-63-10008-5.
- [45] D. G. Long, Q. P. Remund, and D. L. Daum. A cloud-removal algorithm for SSM/I data. *IEEE Transactions on Geoscience and Remote Sensing*, 37(1):54–62, January 1999. ISSN 0196-2892.
- [46] F. S. Marzano, D. Cimini, P. Ciotti, and R. Ware. Modeling and Measurement of Rainfall by Ground-Based Multispectral Microwave Radiometry. *IEEE Transactions on Geoscience and Remote Sensing*, 43(5):1000–1011, May 2005. DOI 10.1109/TGRS.2004.839595.
- [47] S. Paloscia. Contribution of Microwave Radiometry in Agrometeorological Studies. In *EARSEL Advances in Remote Sensing*, volume 2 of 2, pages 15–21, June 1993. ISBN 2908885069.
- [48] P. F. Goldsmith, C. T. Hsieh, G. R. Huguenin, J. Kapitzky, and E. L. Moore. Focal Plane Imaging Systems for Millimeter Wavelengths. *IEEE Transactions on Microwave Theory and Techniques*, 41(10):1664–1675, October 1993. ISSN 0018-9480.
- [49] P. F. Goldsmith. *Quasioptical Systems: Gaussian Beam Quasioptical Propagation and Applications*, volume 4. Wiley-IEEE Press, 1 edition, December 1997. ISBN 0780334396.
- [50] G. Luzzi, P. Ferrazzoli, S. Gagliani, and T. Mazzoni. *Microwave Radiometry and Remote Sensing of The Environment*, chapter Microwave radiometry as a tool for forest fire detection: Model analysis and preliminary experiments, pages 411–418. Utrecht: VSP, Rome, Italy, February 1994. ISBN 90-6764-189-9.

- [51] European Committee for Standardization. EN 54-9 Components of Automatic Fire Detection Systems - Methods of Test of Sensitivity to Fire. EN Standard BS 5445-9:1984, EN 54-9:1982, British Standards Institution, May 1982. ISBN 0-580-13876-3.
- [52] V. Babrauskas. Ignition of Wood: A Review of the State of the Art. In *Interflam2001*, volume 1, pages 71–88, Edinburgh Conference Centre, Scotland, September 2001. Interscience Communications Ltd. ISBN 09532312 7 5.
- [53] I. PopStefanija. Airborne L-band Radiometers for Remote Sensing of Soil Moisture. Commercial product datasheet, ProSensing Inc., Amherst, USA, 2012. [Online; accessed 3-July-2013], Available at [http://www.northerngulfstitute.org/noaa\\_uas\\_wksp\\_2012/presentations/PopStefanija\\_AirborneL-bandRadiometers.pdf](http://www.northerngulfstitute.org/noaa_uas_wksp_2012/presentations/PopStefanija_AirborneL-bandRadiometers.pdf).
- [54] P. Dvorak, M. Mazanek, and S. Zvanovec. Short-term Prediction and Detection of Dynamic Atmospheric Phenomena by Microwave Radiometer. *Radioengineering*, 21(4):1060–1066, 2010. ISSN: 1210-2512.
- [55] C. M. Alabaster. *The Microwave Properties of Tissue and Other Lossy Dielectrics*. Doctoral thesis, Cranfield University, Cranfield - Bedford, United Kingdom, March 2004.
- [56] H. Kabir, K. Ashrafuzzaman, M.S. Chowdhury, and K.S. Kwak. Studies of Scattering, Reflectivity, and Transmittivity in WBAN Channel: Feasibility of Using UWB. *Sensors — Open Access Journal*, 10(6):5503–5529, June 2010. DOI 10.3390/s100605503.
- [57] S. Osterrieder and G. Schaller. An Improved Microwave Radiometer for Measurements on the Human Body. In *12th European Microwave Conference, 1982*, pages 559–564, Helsinki, Finland, September 1982. DOI 10.1109/EUMA.1982.333120.
- [58] Inc. FLIR Systems. FLIR i-Series Infrared Camera Comparison Chart., 2013. [Online; accessed 19-June-2013], Available at [http://www.flir.com/thermography/america/us/view/?id=54156&collectionid=601&col=54163?](http://www.flir.com/thermography/america/us/view/?id=54156&collectionid=601&col=54163)
- [59] P. Dvorak and S. Zvanovec. On the Sensitivity of Fire Detection by a Microwave Radiometer. In *IEEE International Geoscience and Remote Sensing Symposium*, pages 402–405, Melbourne, Australia, July 21-26 2013. IEEE Geoscience and Remote Sensing Society. ISBN 978-1-4799-1113-4.